Dynamics and Long-Range Interactions in 1D Quantum Systems

Diplomarbeit

von

Johannes Schachenmayer

Physik Department der Technischen Universität München
(Durchgeführt am Institut für Theoretische Physik der Universität Innsbruck)

November 2008

Danksagung

Mein Dank gilt allen, die zur Entstehung dieser Diplomarbeit beigetragen haben. Insbesondere möchte ich mich zunächst bei Prof. Dr. Peter Zoller und Prof. Dr. Harald Friedrich bedanken, die mir die Durchführung dieser Diplomarbeit überhaupt erst ermöglicht haben. Ich danke der Universität Innsbruck für ihre Gastfreundschaft und die zur Verfügung gestellten Mittel für die Durchführung meiner Arbeit in dieser wundervollen Stadt.

Mein ganz besonderer Dank gilt Dr. Andrew J. Daley für die umfassende Betreuung meines Diplomprojekts. Wie kein anderer konnte er mich in diesem Jahr durch seine tiefe physikalische Einsicht, seine Ratschläge und Kreativität begeistern und motivieren (letztendlich sogar für die Teilnahme beim Münchner Staffelmarathon). Ich danke ihm, dass er sich stets Zeit für mich genommen hat, und er es mir ermöglicht hat, auch die Welt der Physik in Barcelona und Oxford, fernab von meinem Schreibtisch kennenzulernen.

Ich danke allen Mitarbeitern der Forschungsgruppe um Prof. Dr. Peter Zoller und aus anderen Bereichen der Physik in Innsbruck. Es fand sich in diesem Jahr stets jemand, mit dem ich interessante physikalische und nichtphysikalische Diskussionen führen konnte, die mir teilweise zu mehr Erkenntnis verhalfen, als ich mir je alleine hätte erarbeiten können. Insbesondere erwähnen möchte ich an dieser Stelle Dr. Igor Lesanovsky und Markus Müller, da sie einen wesentlichen Teil zu meinem Verständnis für Kapitel 5 beigetragen haben.

Mein Dank gilt auch all denen, die mein Studium an der TU München zu einem unvergesslichen Erlebnis gemacht haben. Ohne Ferdinand Albrecht, Jochen Bruckbauer, Florian Blobner und viele andere hätten diese vier Jahre wohl nur einen Bruchteil so viel Spaß gemacht und die Motivation für so manche Prüfung wäre ungemein schwerer gefallen.

Zu guter Letzt möchte ich mich vor allem bei meinen Eltern bedanken, die mich stets unterstützt und mir mein gesamtes Physikstudium erst ermöglicht haben.

Contents

Chapter 1

Introduction

The potential advantages of quantum computers over their classical counterparts in solving certain problems originate in the large dimension of the Hilbert space, which grows exponentially with the size of a many-body quantum system. Consider, for example, a quantum computer with a register of N qubits, e.g. a chain of N spin-1/2 particles. The state of this system is described by a state vector $|\Psi\rangle$ residing in a 2^N dimensional complex Hilbert space $\mathcal{H}$,

$$|\Psi\rangle = \sum_{j}^{2^N} c_j |j\rangle, \tag{1.1}$$

where $\{|j\rangle\}$ denotes an orthonormal basis set of $\mathcal{H}$ and $c_j \in \mathbb{C}$. Changing the state of the register, i.e. applying a unitary transformation $\hat{U}$ on $|\Psi\rangle$, in general simultaneously changes the values of 2^N complex numbers.

In contrast, a classical computer with a register consisting of M classical bits is only able to represent an integer ranging from 0 to 2^M or an arbitrary floating point number up to a limited precision. For example, a double precision number, which is represented by the 64 bits IEEE 754 standard, is able to express values with approximately 15 decimal places. A change in the state of the bits alters the value of the scalar associated to them. Thus, for a classical computer the simultaneous variation of 2^N double precision complex numbers required to perform operations on $2^{(N+7)}$ bits. For a modest number of $N = 300$ qubits in the quantum mechanical case, this translates to $2^{307} \approx 10^{92}$ classical bits, which already by far exceeds the estimated number of particles present in the entire observable universe! This implies the impossibility to exactly simulate large quantum mechanical systems, like a 300 spin-1/2 chain on any foreseeable classical hardware.

However, it turns out that for low energy regimes a quantum mechanical system can often be very well described by considering only basis states within a small fraction of the full Hilbert space $\mathcal{H}$. In recent years, very successful classical algorithms have been developed, which take advantage of this fact and diagonalise the Hamiltonian only on a sufficiently large subspace that is computationally tractable though. Thereby, efficient ground state calculations and real time simulations of many-body quantum systems at low energies have become possible. Note that conversely this implies that the advantage of a quantum computer is more subtle, as classically simulatable state evolutions cannot contribute to a quantum computer being superior to a classical one. Indeed, powerful quantum algorithms, for example Shor's famous factoring algorithm [1], are based on the use of highly entangled input registers, i.e. states in which information is stored in non-local correlations. The efficient classical numerical techniques break down upon simulating highly entangled states, since they can only be described by basis sets occupying a large fraction of the Hilbert space $\mathcal{H}$.

Numerical methods for simulating quantum mechanical many-body systems have become especially interesting, since in the last few years large experimental progress has been achieved in engineering strongly correlated many-body systems. Especially cold atoms in optical lattice potentials have become an ideal context in which to study such strongly interacting systems, giving rise to interesting observations. Analytical descriptions of many-body quantum systems exist in several limits, e.g. mean-field theory in higher dimensions, but turn out to be very challenging in general. This especially affects the solution to questions related to dynamical properties. Numerical simulations could therefore lead to a lot of insight and aid both experimental and theoretical research in this domain.

Optical Lattices

One promising implementation for quantum information processing is a system of cold atoms loaded into an optical lattice potential, which is created by standing waves of laser light. This system offers both a realisation of lattice Hamiltonians on a microscopic level, and a realisation where time-dependent control is available over individual system parameters. The use of these systems to realise the Bose-Hubbard model was first proposed by D. Jaksch et al. [2] with theoretically predicting a realisation of the Bose-Hubbard model in an optical lattice. This model, already studied in 1989 by M. P. A. Fisher et al. [3], gives rise to interesting physical behaviour including the existence of different ground state quantum phases. The first experimental lattice realisation, in which these phases were observed, was successfully achieved in

a seminal experiment by M. Greiner et al. [4]. Since then, a large variety of experimental setups have been tailored to toy-model lattice Hamiltonians, partially well known from condensed matter theory, but with experimental control over nearly every system parameter.

The possibilities for the manipulation of cold atoms in optical lattice potentials are extremely versatile (Reviews can be found in [5–7]). For example, the control over the lattice depths via the laser intensity in each dimension gives rise to the opportunity to create effectively one- or two-dimensional (1D/2D) configurations and furthermore makes it possible to tune tunnelling rates and on-site interactions. A deeper lattice, for example, results in a decreased tunnelling probability to neighbouring sites and on the other hand also leads to stronger on-site interactions due to a tighter confinement at each site. Interaction strengths can even further be independently modelled by making use of magnetical or optical Feshbach resonances. Also different lattice geometries can be realised by altering angles between the confining laser beams and energy offsets can be created by external fields or even be addressed to particular sites by superimposing additional optical standing waves. More than one species of particles loaded into the same optical lattices opens another vast number of opportunities.

Recently, also systems with molecules or Rydberg atoms, atoms excited into states of high principal quantum number n, have received a lot of attention. These systems are particularly interesting since they are invoking dipolar or van der Waals long-range interactions. Rydberg atoms have become especially famous in this context since proposals arose to employ them for fast quantum logic gates [8, 9].

Despite the fact that quantum computer implementations might be a vision of the far future, at an earlier stage optical lattices could already succeed as an realisation of a universal quantum simulator [10]. Those were already proposed by R. P. Feynman in 1982. The fundamental idea is to utilise a controllable and observable quantum system, for example cold atoms in an optical lattice, to mimic the dynamical evolution of a different system under any desired Hamiltonian. Thereby, important questions from condensed matter physics, nowadays still unresolved due to their mathematical complexity, for example high T_C superconductivity, could be answered by quantum simulators.

Numerical Techniques – DMRG & TEBD

Algorithms to simulate unitary dynamics of lattice models can be useful in several domains: (i) They can be used to quickly test analytical theories for many-body quantum system, without requiring years for setting up experi-

mental apparatuses; (ii) They can be utilised to directly test the validity of model Hamiltonian implementations in experiments by direct comparison of experimental to numerical results; (iii) Because of (ii), they can be an important link towards quantum simulation or quantum computation realisations; (iv) They can lead to further insight into quantum information theory and be utilised to study emergence of entanglement.

As mentioned above, exact straight forward integration of the Schrödinger equation is prohibitive for large many-body quantum systems because of the huge dimension of the Hilbert space $\mathcal{H}$. Additionally, algorithms based on product state dynamics like the mean-field Gutzwiller ansatz, suitable for higher dimensional systems, turn out to break down for 1D systems. However, a key step towards a simulation algorithm, initially restricted to ground state calculations of large 1D quantum system, was achieved with the introduction of the density matrix renormalisation group algorithm (DMRG) in 1992 by S. R. White [11]. The origin of the early success of this method has been nowadays understood in terms of quantum correlation. DMRG is based on a truncated state representation, retaining only slightly-entangled basis states. These representations are denoted as truncated matrix products states (MPS) and turn out to be an excellent approximation in the case of most low-energy regimes of 1D lattice models. From this understanding, fruitful new algorithms capable of both time simulation and ground state calculation were invented. An example is the the time evolving block decimation algorithm (TEBD) [12], which is utilising a truncated Hilbert space that is adapted from the entire space $\mathcal{H}$ along with the time-evolution. Not only finite 1D systems, but also generalisations to infinite 1D systems (iTEBD) [13], higher dimensions [14, 15] and open quantum systems [16, 17] have been achieved in recent years. However, despite some ideas as to how long range interactions (e.g., in [18, 19]) can be implemented, these methods have been primarily applied to short-range interactions.

Purposes of this Thesis

1. We study the dynamic transport properties of an infinite 1D Bose-Hubbard model. Analytical predictions [20] and experimental observations [21] have been recently performed, addressing the stability of superfluid currents in this system. We are going to complement this work by numerical results, utilising the iTEBD algorithm to provide quantitative calculations of the behaviour of the system in 1D.

2. We extend the existing TEBD algorithm for the implementation of long-range interactions in finite and infinite systems, and thereby open

this technique to a wider range of physical applications.

3. We apply our newly developed method to a system of Rydberg atoms, excited in an optical lattice potential. There we will consider long-range dipolar interactions.

Overview

This thesis is organised in four main chapters. Chapters 2 and 4 will elaborate on the algorithmic simulation techniques, 3 and 5 on the application to physical systems.

In chapter 2 we outline the history of DMRG and introduce the TEBD algorithm as originally presented by G. Vidal [12]. In the first part (Section 2.1) we will explain the matrix product state representation (MPS) and show how it can be used to perform time simulations or ground state calculations for 1D lattice Hamiltonians. In the second part (Section 2.2) we will adopt a representation for infinite 1D systems (iMPS) and show how it can be utilised for the simulation of these systems (iTEBD).

Chapter 3 deals with the simulation of bosonic transport properties in an infinite 1D optical lattice. We are going to analyse the stability of superfluid boson currents in the Bose-Hubbard model. In the first part of this chapter (Section 3.1) we shortly introduce the general theoretical background of the Bose-Hubbard model in optical lattices, boson currents, and current instabilities. In the second part (Section 3.2 & 3.3) we present and demonstrate a method to utilise the iTEBD algorithm for this system.

An algorithm for the solution of the Schrödinger equation in large 1D lattice systems including long-range interactions is presented in chapter 4. We present a scheme to complement the existing TEBD and iTEBD frameworks. Initially we introduce an implementation for finite systems, which we denote lTEBD algorithm (Section 4.1). Afterwards (Section 4.2), we extend this scheme for infinite state representations (ilTEBD).

The lTEBD algorithm will be applied in chapter 5, where we analyse a system of Rydberg excitations in a 1D lattice, considering dipolar long-range interactions. Firstly, we will give a short theoretical outline (Section 5.1). In the second part (Section 5.2) we will study both, ground states and real time dynamics under the model Hamiltonian. We will further elaborate on a scheme to experimentally prepare an interesting "anti-ferromagnetic like" state.

Finally, chapter 6 concludes with a summary and an outlook for projects discussed in this thesis.

Bibliography

[1] M. A. Nielsen and I. L. Chuang. *Quantum Computation and Quantum Information*. Cambridge University Press, (2000).

[2] D. Jaksch, C. Bruder, J. I. Cirac, C. W. Gardiner, and P. Zoller. *Phys. Rev. Lett.* **81**, 3108 (1998).

[3] M. P. A. Fisher, P. B. Weichman, G. Grinstein, and D. S. Fisher. *Phys. Rev. B* **40**, 546 (1989).

[4] M. Greiner, O. Mandel, T. Esslinger, T. W. Hänsch, and I. Bloch. *Nature* **415**, 39 (2002).

[5] D. Jaksch and P. Zoller. *Annals of Physics* **315**, 52 (2005).

[6] I. Bloch, J. Dalibard, and W. Zwerger. *Rev. Mod. Phys.* **80**, 885 (2008).

[7] M. Lewenstein, A. Sanpera, V. Ahufinger, B. Damski, A. Sen De, and Sen U. *Adv. Phys.* **56**, 243 (2007).

[8] D. Jaksch, J. I. Cirac, P. Zoller, S. L. Rolston, R. Côté, and M. D. Lukin. *Phys. Rev. Lett.* **85**, 2208 (2000).

[9] M. D. Lukin, M. Fleischhauer, R. Cote, L. M. Duan, D. Jaksch, J. I. Cirac, and P. Zoller. *Phys. Rev. Lett.* **87**, 037901 (2001).

[10] S. Lloyd. *Science* **273**, 1073 (1996).

[11] S. R. White. *Phys. Rev. Lett.* **69**, 2863 (1992).

[12] G. Vidal. *Phys. Rev. Lett.* **93**, 040502 (2004).

[13] G. Vidal. *Phys. Rev. Lett.* **98**, 070201 (2007).

[14] F. Verstraete and J. I. Cirac. *arXiv: cond-mat/0407066* (2004).

[15] F. Verstraete, V. Murg, and J. I. Cirac. *Adv. Phys.* **57**, 143 (2008).

[16] M. Zwolak and G. Vidal. *Phys. Rev. Lett.* **93**, 207205 (2004).

[17] F. Verstraete, J. J. García-Ripoll, and J. I. Cirac. *Phys. Rev. Lett.* **93**, 207204 (2004).

[18] Y.-Y. Shi, L.-M. Duan, and G. Vidal. *Phys. Rev. A* **74**, 022320 (2006).

[19] I. P. McCulloch. *J. Stat. Mech.* **2007**, P10014 (2007).

[20] E. Altman, A. Polkovnikov, E. Demler, B. I. Halperin, and M. D. Lukin. *Phys. Rev. Lett.* **95**, 020402 (2005).

[21] J. Mun, P. Medley, G. K. Campbell, L. G. Marcassa, D. E. Pritchard, and W. Ketterle. *Phys. Rev. Lett.* **99**, 150604 (2007).

Chapter 2

Simulation of 1D Quantum Systems

Exact simulation of large quantum mechanical systems is impossible on classical computers, due to the exponential growth of the Hilbert space with the system size. A large quantum state cannot even be stored on a classical computer. For example, looking at a 1D chain of N spins (qubits), each with dimensionality 2, the state of a composite system is represented by 2^N complex numbers. Representing just 50 Spins would require to store $2{\times}2^{50} \approx 2{\times}10^{15}$ numbers, thus in double precision approximately $16{\times}10^6$ GB of storage memory would be required! Furthermore, to compute an arbitrary single evolution of this state, matrices containing approximately 10^{30} complex numbers would have to be multiplied to the state vector, requiring $\mathcal{O}(10^{30})$ basic floating point operations (FLOP). Today's most powerful supercomputer[1] can perform approximately 1000 TFLOP/s and would therefore be occupied more than 30 million years for a single evolution step. Thus, with today's or tomorrow's technology, exact simulation of large quantum mechanical systems is completely intractable.

This apparently insurmountable limitation particularly also concerns systems of particles loaded into an optical lattice potential, which will be studied in chapters 3 and 5. For example, in the 1D Bose-Hubbard model the dimension of the Hilbert space is equivalent to the number of all possible combinations of placing M bosons (with multiple occupations allowed) onto N sites and therefore given by

$$\dim \mathcal{H} = \binom{N+M-1}{M} \equiv \frac{(N+M-1)!}{M!\,(N-1)!}. \tag{2.1}$$

[1] www.top500.org, June 2008

Thus, solutions of small systems with more than a few particles and lattice sites already by far exceed the capabilities of modern computers. For example, a state vector of the system containing 20 particles on 40 lattice sites has a dimension of approximately 10^{15}!

Despite this perspective enormous progress has been achieved in the last 16 years in developing methods for near-exact numerical treatment of large quantum systems. Especially the invention of density matrix renormalisation group (DMRG) techniques has made it possible to simulate large quantum systems up to an unanticipated precision. A general extensive review of DMRG methods is found in [1].

The DMRG algorithm was first introduced by S. R. White in 1992 [2] and was able to calculate $T = 0$ ground states of large 1D quantum systems (e.g. the Heisenberg-chain over 60 sites [3]) up to an high precision with ordinary computational resources. The key idea of the algorithm is the decimation of the huge Hilbert space down to a computationally tractable smaller size without significantly changing physical properties. In the DMRG algorithm, this truncation is performed by retaining only basis states related to a small weight in the expansion of a reduced density matrix for some part of the system in terms of its eigenstates. As was pointed out later by for example S. Östlund and S. Rommer [4,5] DMRG generates ground states that can be written in a matrix product state (MPS) form. In this context, the success of DMRG could be identified due to the approximation of keeping only "slightly entangled" states corresponding to all bipartite splittings in the 1D chain (see for example [6]).

Starting in 2002, DMRG has also been successfully extended for time-evolution simulations of 1D systems. First attempts were made using direct forward integration of the Schrödinger equation on a static decimated Hilbert space by M. A. Cazalilla [7]. Following that, enormous progress has been achieved by employing adaptively decimated spaces changing during time evolution. This method, referred to as the time evolving block decimation (TEBD) algorithm was introduced by G. Vidal in 2003 [8, 9], formulated in terms of MPS. The same algorithm has been adapted for infinite sized systems [10]. In 2004 it was translated to the DMRG language by A. J. Daley et al. [11] and White and Feiguin [12]. This turned out to be very fruitful and made possible the transportation of very well known numerical improvements like the implementation of conservation laws from DMRG algorithms to the TEBD framework.

Furthermore, in recent years the TEBD algorithm has also been generalised to work with open systems by F. Verstraete and M. Zwolak [13, 14] making possible the simulation of finite temperature and master equations. Also, similar success has been achieved using projected entangled pair states

(PEPS), which generalise MPS for use with periodic boundary conditions, and in higher dimensions [15]. These methods have been reviewed in [16].

The TEBD algorithm has already been successfully applied to study dynamical properties of 1D systems in many ways. For instance, dynamics of phase transitions in the Bose-Hubbard model [17], spin-charge separation in Fermi-Hubbard [18] and two component Bose-Hubbard systems [19], evolution of magnetisation within Heisenberg spin-chains [20], currents in a single atom transistor [21], or Andreev-like reflections for fermions and bosons [22] could be analysed in detail.

In this chapter, we will introduce the TEBD (Section 2.1) and iTEBD (Section 2.2) algorithms, which we will both extensively apply to atoms in optical lattices in later chapters.

2.1 Time Evolving Block Decimation Algorithm (TEBD)

The time evolving block decimation (TEBD) algorithm, developed by G. Vidal [8] is equivalent to the adaptive time-dependent DMRG method with only notational differences as pointed out in [11]. It is based on an approximate state representation appropriate for a 1D quantum system, neglecting highly entangled basis states. This truncated representation makes an efficient storage of low energy states containing only small amounts of bipartite entanglement possible. By introducing a scheme to apply operators which act on two subsequent sites within this framework, time evolution can be efficiently simulated. This is achieved by decomposing the time-evolution operator into sweeps of two-site gates via a Suzuki-Trotter expansion. TEBD is also capable of calculating ground states by simulating evolution in imaginary time.

2.1.1 The MPS State Representation

To store an entire state for a large quantum system, one has to find an approximate state representation, which is valid in limits of certain physical quantities. Treating large quantum systems, a natural choice for such a quantity can be entanglement. The amount of entanglement in a system is related to the number of coefficients required to describe it in a bipartite Schmidt decomposition (Schmidt rank) [23], which is the key idea of the TEBD state representation.

Schmidt Decomposition

Consider a bipartite quantum state residing in the Hilbert space $\mathcal{H}$, which is composed of two subspaces A and B, $\mathcal{H} \equiv \mathcal{H}_A \otimes \mathcal{H}_B$ with dimensions d_A, d_B and orthonormal bases $\{|i\rangle_A\}$,$\{|j\rangle_B\}$ respectively.

$$|\Psi_{AB}\rangle = \sum_{i}^{d_A} \sum_{j}^{d_B} c_{i,j} |i\rangle_A \otimes |j\rangle_B. \tag{2.2}$$

The complex coefficient matrix $c_{i,j}$ can always be decomposed via a singular value decomposition (see [23]) into

$$c_{i,j} = \sum_{k}^{\chi_{AB}} u_{i,k} s_{k,k} v_{k,j}, \tag{2.3}$$

where the $u_{i,k}$ are the elements of a $d_A \times d_A$ unitary matrix, $v_{k,j}$ of a $d_B \times d_B$ unitary matrix, and $s_{k,k'}$ of a diagonal $d_A \times d_B$ matrix. The diagonal elements of $s_{k,k'}$ are the non-negative singular values of $c_{i,j}$ and shall be denoted as Schmidt coefficients $\lambda_k \equiv s_{k,k}$ They satisfy

$$\sum_{k}^{\chi_{AB}} s_{k,k}^2 = \sum_{k}^{\chi_{AB}} \lambda_k^2 = 1. \tag{2.4}$$

The Schmidt vectors $|\Phi_k^{A/B}\rangle$ residing in spaces $\mathcal{H}_A$ and $\mathcal{H}_B$ respectively are defined as

$$\begin{aligned} |\Phi_k^A\rangle &\equiv \sum_{i}^{d_A} u_{i,k} |i\rangle_A \\ |\Phi_k^B\rangle &\equiv \sum_{j}^{d_B} v_{k,j} |j\rangle_B \end{aligned} \tag{2.5}$$

and form an orthonormal basis in each subsystem A and B due to the unitarity of $u_{i,k}$ and $v_{k,j}$. Inserting (2.5) and (2.3) into (2.2) leads to the Schmidt decomposition of $|\Psi_{A,B}\rangle$,

$$|\Psi_{AB}\rangle = \sum_{k}^{\chi_{AB}} \lambda_k |\Phi_k^A\rangle \otimes |\Phi_k^B\rangle, \tag{2.6}$$

which is an expansion of $|\Psi_{AB}\rangle$ in the Schmidt bases with Schmidt coefficients λ_k.

In quantum information theory, the number of non-zero Schmidt coefficients required to exactly describe the system in a bipartite splitting is called the Schmidt number or Schmidt rank. It is a measure for the amount of entanglement between to subsystems A and B. As a simple example, the trivial Schmidt decomposition of two qubits in the non-entangled product state

$$|0\rangle \otimes |0\rangle,$$

requires only one coefficient $\lambda_k = 1\delta_{k,1}$. In contrast, the maximally entangled Bell state

$$\frac{1}{\sqrt{2}}(|0\rangle \otimes |0\rangle + |1\rangle \otimes |1\rangle),$$

requires two, which equals the maximum possible value of χ_{AB}. Here $\lambda_1 = 1/\sqrt{2}$, $\lambda_2 = 1/\sqrt{2}$ and $\chi_{AB} = \min(d_A, d_B) = 2$.

Mathematically, this bipartite entanglement can be further quantified in terms of the von Neumann entropy of the subsystems [23]. In general, this entropy is defined as

$$S(\rho) = -\mathrm{tr}\rho(\log_2 \rho), \tag{2.7}$$

where "tr" denotes the trace, and $\rho \equiv |\Psi_{AB}\rangle\langle\Psi_{AB}|$ is the density operator of the system. Inserting the Schmidt decomposition of $|\Psi_{AB}\rangle$, (2.6) into (2.7) leads to

$$S = -\sum_{k}^{\chi_{AB}} \lambda_k^2 \log_2(\lambda_k^2). \tag{2.8}$$

The von Neumann entropy is a number $0 \leq S \leq \log_2(\chi_{AB})$. Equality holds only for the completely unentangled product state with $S = 0$, which is the case in the $|0\rangle \otimes |0\rangle$ example and for the maximally entangled state with $S = \log_2(\chi_{AB})$, which is the case in the Bell-state example, where $S = \log_2(\chi_{AB}) = 1$.

Decomposition of a N-Site System

Effectively, what has been achieved by the singular value decomposition (2.3) is the fact that the complex coefficient matrix $c_{i,j}$ of the state vector of the compound system has been expanded into local matrices $u_{i,k}$ and $v_{k,j}$. They are local in the sense that $u_{i,k}$ contains the index i, belonging to system A and $v_{k,j}$ contains the index j, belonging to part B respectively. This was attained at cost of introducing a third index k, over which a sum has to be performed.

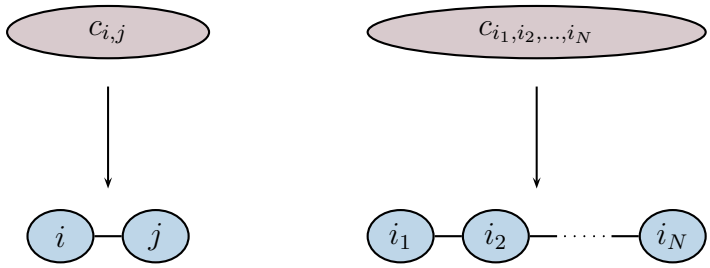

Figure 2.1: The singular value decomposition makes it possible to express complex coefficients of a bipartite quantum state into two local parts (left side). We will show how to achieve this for an arbitrary 1D state composed of N local sites (right side).

We are now going to proceed in the same manner and expand the coefficient matrix of an arbitrary 1D quantum system consisting of N sites, $c_{i_1,i_2,\ldots,i_N}$, into matrices located at individual sites as sketched in Fig. 2.1.

Consider a 1D quantum system composed of N sites, each with a local Hilbert space of dimension d. The entire Hilbert space can then be written as $\mathcal{H} \equiv \mathcal{H}_{A_1} \otimes \mathcal{H}_{A_2} \cdots \otimes \mathcal{H}_{A_N}$. A state spanned in the bipartite system $\mathcal{H}_{A_1} \otimes \mathcal{H}_{R_1}$ with $\mathcal{H}_{R_1} \equiv \mathcal{H}_{A_2} \otimes \mathcal{H}_{A_3} \cdots \otimes \mathcal{H}_{A_N}$ and dimensions $\dim(\mathcal{H}_{A_1}) = d$, $\dim(\mathcal{H}_{R_1}) = d^{(N-1)}$ can be written as (tensor product symbols omitted)

$$|\Psi\rangle = \sum_{i_1}^{d} \sum_{i_R}^{d^{(N-1)}} c_{i_1,i_R} |i_1\rangle |i_R\rangle = \sum_{\alpha_1}^{\chi_1} \lambda_{\alpha_1}^{[1]} |\Phi_{\alpha_1}^{A_1}\rangle |\Phi_{\alpha_1}^{R_1}\rangle. \tag{2.9}$$

Here, the Schmidt vectors $|\Phi_{\alpha_1}^{A_1/R_1}\rangle$ form an orthonormal basis in each subsystem A_1 and R_1. The maximum possible Schmidt rank for a general state is $\chi_1 = d$. By introducing a matrix $\Gamma_{\alpha_1}^{[1]i_1}$ to re-express the state in its original basis in subsystem A_1, one can write

$$|\Psi\rangle \equiv \sum_{\alpha_1}^{\chi_1} \sum_{i_1}^{d} \Gamma_{\alpha_1}^{[1]i_1} \lambda_{\alpha_1}^{[1]} |i_1\rangle |\Phi_{\alpha_1}^{R_1}\rangle. \tag{2.10}$$

Consider now the Schmidt decomposition of $|\Psi\rangle$ within the two-party Hilbert space $(\mathcal{H}_{A_1} \otimes \mathcal{H}_{A_2}) \otimes \mathcal{H}_{R_2}$, split into subsystems $\mathcal{H}_{A_1} \otimes \mathcal{H}_{A_2}$ and $\mathcal{H}_{R_2} \equiv \mathcal{H}_{A_3} \otimes \mathcal{H}_{A_4} \cdots \otimes \mathcal{H}_{A_N}$,

$$|\Psi\rangle \equiv \sum_{\alpha_2}^{\chi_2} \lambda_{\alpha_2}^{[2]} |\Phi_{\alpha_2}^{A_1 A_2}\rangle |\Phi_{\alpha_2}^{R_2}\rangle. \tag{2.11}$$

The dimensions are $\dim(\mathcal{H}_{A_1} \otimes \mathcal{H}_{A_2}) = d^2$, $\dim(\mathcal{H}_{R_2}) = d^{(N-2)}$ and therefore $\chi_2 = d^2$. Noting that $\{|\Phi_{\alpha_2}^{R_2}\rangle\}$ forms an orthonormal basis in $\mathcal{H}_{R_2}$, the Schmidt states $|\Phi_{\alpha_1}^{R_1}\rangle \in \mathcal{H}_{R_1} = \mathcal{H}_{A_2} \otimes \mathcal{H}_{R_2}$ can be expressed as

$$|\Phi_{\alpha_1}^{R_1}\rangle \equiv \sum_{i_2}^{d} \sum_{\alpha_2}^{\chi_2} \Gamma_{\alpha_1\alpha_2}^{[2]i_2} \lambda_{\alpha_2}^{[2]} |i_2\rangle |\Phi_{\alpha_2}^{R_2}\rangle, \tag{2.12}$$

where a new three dimensional array $\Gamma_{\alpha_1\alpha_2}^{[2]i_2}$ has been introduced. Substituting (2.12) into (2.10), the state of the whole system can be written as

$$|\Psi\rangle = \sum_{i_1,i_2}^{d} \sum_{\alpha_1,\alpha_2}^{\chi_1,\chi_2} \Gamma_{\alpha_1}^{[1]i_1} \lambda_{\alpha_1}^{[1]} \Gamma_{\alpha_1\alpha_2}^{[2]i_2} \lambda_{\alpha_2}^{[2]} |i_1\rangle |i_2\rangle |\Phi_{\alpha_2}^{R_2}\rangle. \tag{2.13}$$

Iterating the steps (2.11) and (2.12) on the remaining $(N-3)$ possible splittings of the full space $\mathcal{H}$ (i.e. between sites $3 \leftrightarrow 4, 4 \leftrightarrow 5, \ldots, (N-1) \leftrightarrow N$), the complex coefficients of an arbitrary quantum system composed of N local Hilbert spaces of dimension d

$$|\Psi\rangle = \sum_{i_1,i_2,\ldots,i_N}^{d} c_{i_1,i_2,\ldots,i_N} |i_1\rangle |i_2\rangle \ldots |i_N\rangle \tag{2.14}$$

can be re-expressed as

$$c_{i_1,i_2,\ldots,i_N} \equiv \sum_{\alpha_1}^{\chi_1} \sum_{\alpha_2}^{\chi_2} \cdots \sum_{\alpha_{N-1}}^{\chi_{N-1}} \Gamma_{\alpha_1}^{[1]i_1} \lambda_{\alpha_1}^{[1]} \Gamma_{\alpha_1\alpha_2}^{[2]i_2} \lambda_{\alpha_2}^{[2]} \ldots \lambda_{\alpha_{N-1}}^{[N-1]} \Gamma_{\alpha_{N-1}}^{[N]i_N}. \tag{2.15}$$

Diagrammatic Notation

It turns out to be useful to introduce a diagrammatic notation for the decomposition (2.15). This can be visualised as

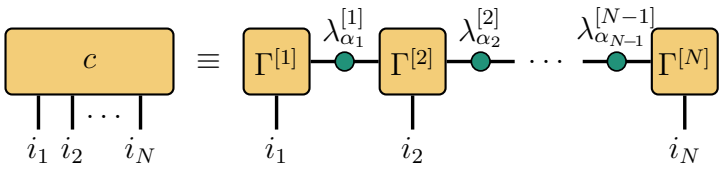

, (2.16)

which is a representation in which indices are depicted by straight lines and objects with m indices are m-dimensional arrays. For example, in (2.16) the state coefficients $c_{i_1,i_2,\ldots,i_N}$ are described by the large rectangle on the left hand side and the three dimensional $\Gamma_{\alpha_l\alpha_l}^{[l]i_l}$ $(1 < l < N)$ objects are rendered

by the smaller rectangles on the right hand site. The Schmidt coefficients are formally defined as diagonal matrices (2 indices) via $\lambda^{(\gamma)}_{\alpha_i} \equiv \lambda_{\alpha_i}\delta^{\gamma}_{\alpha_i}$. A line connecting two objects indicates a summation over the corresponding index. This visualisation of equations with many sums will turn out to be very useful to find optimal ways to transform the states in the TEBD state representation. For simplicity, in most cases the Γ- and λ-letters or index identifiers will be dropped, except in the case that they significantly contribute to the understanding of the diagram.

Truncated MPS

Representation (2.15) is denoted a "matrix product state" (MPS) and said to be in its canonical form, if for all bond indices α_j ($0 \leq j \in \mathbb{N} < N$), the state can be expanded in an orthonormal Schmidt bases $\{|\Phi^{[j]L}_{\alpha_j}\rangle\}$ to the left and $\{|\Phi^{[j]R}_{\alpha_j}\rangle\}$ to the right of the specific bond,

$$|\Psi\rangle = \sum_{\alpha_j}^{\chi_j} \lambda^{[j]}_{\alpha_j} |\Phi^{[j]L}_{\alpha_j}\rangle |\Phi^{[j]R}_{\alpha_j}\rangle, \tag{2.17}$$

with

$$\begin{aligned} |\Phi^{[j]R}_{\alpha_j}\rangle = \sum_{i_{j+1},i_{j+2},\ldots,i_N}^{d} \sum_{\alpha_{j+1}}^{\chi_{j+1}} \sum_{\alpha_{j+2}}^{\chi_{j+2}} \cdots \sum_{\alpha_{N-1}}^{\chi_{N-1}} \\ \Gamma^{[j+1]i_{j+1}}_{\alpha_j\alpha_{j+1}} \lambda^{[j+1]}_{\alpha_{j+1}} \Gamma^{[j+2]i_{j+2}}_{\alpha_{j+1}\alpha_{j+2}} \lambda^{[j+2]}_{\alpha_{j+2}} \cdots \\ \ldots \lambda^{[N-1]}_{\alpha_{N-1}} \Gamma^{[N]i_N}_{\alpha_{N-1}} |i_{j+1} i_{j+2} \ldots i_N\rangle, \end{aligned} \tag{2.18}$$

and

$$\begin{aligned} |\Phi^{[j]L}_{\alpha_j}\rangle = \sum_{i_1,i_2,\ldots,i_j}^{d} \sum_{\alpha_1}^{\chi_1} \sum_{\alpha_2}^{\chi_2} \cdots \sum_{\alpha_{j-1}}^{\chi_{j-1}} \Gamma^{[1]i_1}_{\alpha_1} \lambda^{[1]}_{\alpha_1} \Gamma^{[2]i_2}_{\alpha_1\alpha_2} \lambda^{[2]}_{\alpha_2} \cdots \\ \ldots \lambda^{[j-1]}_{\alpha_{j-1}} \Gamma^{[j]i_j}_{\alpha_{j-1}\alpha_j} |i_1 i_2 \ldots i_j\rangle. \end{aligned} \tag{2.19}$$

Expression (2.15) is still an exact formulation of the state $|\Psi\rangle$, and the arrays Γ and λ also cannot be stored for large systems, since the maximal possible Schmidt rank grows exponentially with the system size. However, $|\Psi\rangle$ can now be approximated by writing all sums over bond indices α_j in descending order and truncating terms, with bond indices larger than a fixed value of $\chi \leq \max(\chi_j)$. This reduces the Hilbert space by removing the small weighted basis states, leaving only a computationally tractable dimension.

An error per bond by doing this truncation can be quantified directly from the normalisation condition (2.4) as

$$\epsilon_j = \sum_{\alpha_j=(\chi+1)}^{\chi_j} {\lambda_{\alpha_j}^{[j]}}^2. \tag{2.20}$$

A priori, it is not clear for which systems this is a good approximation. It is clear that because of the limited number of Schmidt basis states, the approximation is only valid for states containing only little bipartite entanglement. For example, in a system of 50 qubits, the von Neumann entropy of the maximally entangled state would be $S_{max} = \log_2(\chi_{25}) = 25$. However, choosing for example a truncation value of $\chi = 128$, which is already quite large in practice, allows only states with von Neumann entropy lower than $S_\chi = 7$.

In recent years, it has been analytically shown that for 1D spin chains, entanglement contained in the ground state is in general small and that the MPS provides a faithful representation of such states [6, 16]. It has been proven that away from a quantum critical point in the limit of infinite system length, for several spin-models the ground-state von Neumann entropy saturates at some fixed value [24, 25]. Therefore, it can be expected that for large enough values of χ, the truncated MPS representation gets very close to the exact quantum state in such chains. Furthermore, the great success of DMRG/TEBD methods in simulating many different 1D systems (e.g. [17–22,26,27]) indicates that the analytical results from spin-chains hold in a much more general context.

However, in practice, the results have to be checked by using increasingly higher values of the truncation parameter χ and looking for convergence. Furthermore, during time evolution one must ensure, that the truncation errors per bond (2.20) remain small.

2.1.2 Expectation Values

Physically interesting quantities of a many-body state $|\Psi\rangle$ are typically either local expectation values of the form $\langle\Psi|\hat{O}_l|\Psi\rangle$, for example the particle number expectation value in the Bose-Hubbard model $\langle\Psi|\hat{n}_l|\Psi\rangle$ at a specific site l, or correlation functions computed over several sites. The simplest examples of these are correlation functions of the form $\langle\Psi|\hat{O}_l\hat{O}_m|\Psi\rangle$, like the single particle density matrix $\langle\Psi|\hat{b}_l^\dagger\hat{b}_m|\Psi\rangle$ (see chapter 3).

Local Expectation Values

In a canonical state representation (2.15), $|\Psi\rangle$ can be locally expressed at site l as

$$|\Psi\rangle = \sum_i \sum_{\alpha,\beta} \lambda_\alpha^{[l-1]} \Gamma_{\alpha\beta}^{[l]i} \lambda_\beta^{[l]} |i\rangle_l |\Phi_\alpha^{[l]L}\rangle |\Phi_\beta^{[l]R}\rangle. \tag{2.21}$$

Therefore, using this local Schmidt basis representation of $|\Psi\rangle$, one-site operators $\hat{O}_l \equiv O_i^{[l]j} |j\rangle_l \langle i|_l$ at this site can be applied by simply updating $\Gamma_{\alpha\beta}^{[l]i}$

$$\tilde{\Gamma}_{\alpha\beta}^{[l]j} = \sum_i O_i^{[l]j} \Gamma_{\alpha\beta}^{[l]i}. \tag{2.22}$$

In the diagrammatic picture, the process from equation (2.22) can be expressed via

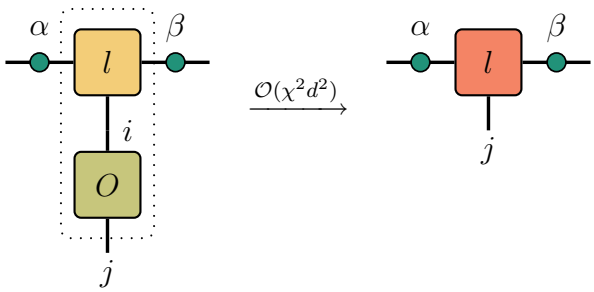

, (2.23)

where the dotted line on the left hand sites indicates the part of the "tensor network" that will be contracted in the following step. In the graphical visualisation, it is also very easy to derive the complexity of the process, by counting the index-lines involved. In this example $\mathcal{O}(\chi^2 d^2)$ basic operations are required, because we must sum over the connected indices, and all other indices of the final object (represented by the solid lines passing through the dotted line).

The local expectation value can now be calculated by evaluating the sum

$$\langle \Psi | \hat{O}_l | \Psi \rangle = \sum_j \sum_{\alpha,\beta} (\lambda_\alpha^{[l-1]})^2 \tilde{\Gamma}_{\alpha\beta}^{*[l]j} \tilde{\Gamma}_{\alpha\beta}^{[l]j} (\lambda_\beta^{[l]})^2, \tag{2.24}$$

where the orthonormality of the Schmidt bases $\{|\Phi_\alpha^{[l]L}\rangle\}$ and $\{|\Phi_\beta^{[l]R}\rangle\}$ has been exploited. In this step $\mathcal{O}(\chi^2 d)$ operations are required and it can be

visualised via

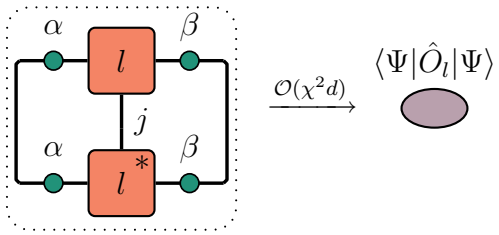

, (2.25)

where the ellipse on the right side has no index and therefore denotes a zero-dimensional matrix, i.e. a scalar.

Off-Site Expectation Values

To evaluate expectation values over distinct sites l and m, $a \equiv |l-m|$, after applying the operators $\hat{O}_l$ and $\hat{O}_m$ according to (2.22)/(2.23) on site l and m respectively, the following sum has to be evaluated:

$$\begin{aligned}\langle\Psi|\hat{O}_l\hat{O}_m|\Psi\rangle \\ = \sum_{i_1,\ldots,i_a}\sum_{\alpha_1,\ldots\alpha_a} (\lambda^{[l]}_{\alpha_1})^2\Gamma^{*[l]i_1}_{\alpha_1\alpha_2}\tilde{\Gamma}^{[l]i_1}_{\alpha_1\alpha_2}(\lambda^{[l+1]}_{\alpha_2})^2\Gamma^{*[l+1]i_1+1}_{\alpha_2\alpha_3}\Gamma^{[l+1]i_1+1}_{\alpha_2\alpha_3}(\lambda^{[l+2]}_{\alpha_3})^2\ldots \\ \ldots(\lambda^{[m-1]}_{\alpha_{a-1}})^2\Gamma^{*[m]i_a}_{\alpha_{a-1}\alpha_a}\tilde{\Gamma}^{[m]i_a}_{\alpha_{a-1}\alpha_a}(\lambda^{[m]}_{\alpha_a})^2,\end{aligned} \quad (2.26)$$

where again the orthonormality of the Schmidt bases has been exploited. An efficient way to perform this operation is:

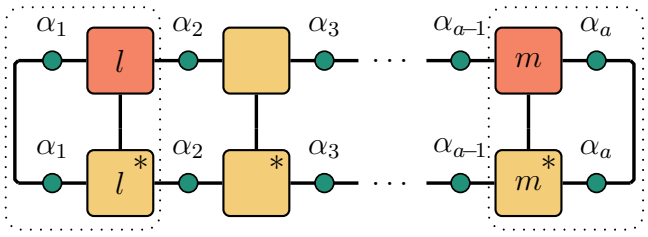

(2.27)

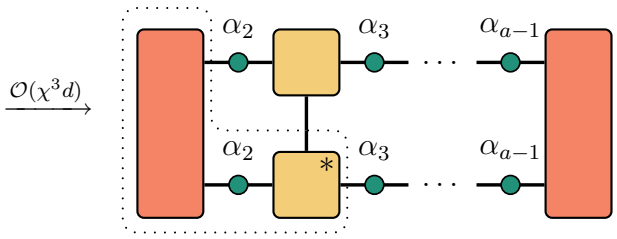

(2.28)

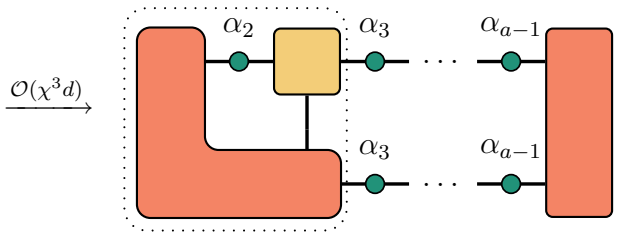

(2.29)

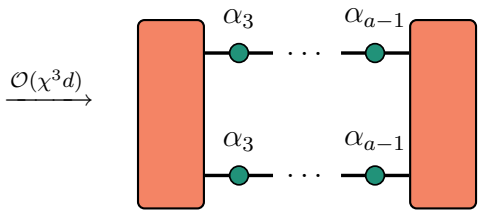

. (2.30)

Iterating steps (2.29) and (2.30) $(a-4)$ times leads to:

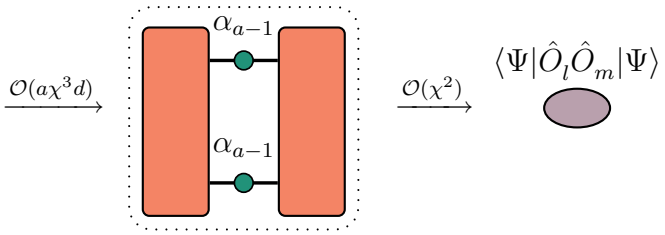

. (2.31)

Thus, in the MPS state representation the expectation values over distinct sites l and m, $\langle\Psi|\hat{O}_l\hat{O}_m|\Psi\rangle$, can be computed within a total of $\mathcal{O}(|l-m|\ \chi^3 d)$ basic operations.

2.1.3 The Algorithm

Next-Neighbour Gates

The most important step in the TEBD algorithm is the implementation of gates, acting on two subsequent sites. We begin with the state vector expanded in the basis of two neighbouring sites l and $l+1$ as

$$|\Psi\rangle = \sum_{i,j} \sum_{\alpha,\beta,\gamma} \lambda_\alpha^{[l-1]} \Gamma_{\alpha\beta}^{[l]i} \lambda_\beta^{[l]} \Gamma_{\beta\gamma}^{[l+1]j} \lambda_\gamma^{[l+1]} |i\rangle_l |j\rangle_{l+1} |\Phi_\alpha^{[l]L}\rangle |\Phi_\gamma^{[l+1]R}\rangle. \tag{2.32}$$

This allows for application of two site operators $\hat{U}_{l,l+1} \equiv U_{i,j}^{a,b} |a\rangle_l |b\rangle_{l+1} \langle i|_l \langle j|_{l+1}$ by evaluating the sum

$$\Theta_{\alpha\gamma}^{ab} \equiv \sum_{i,j} U_{ij}^{ab} \sum_\beta \lambda_\alpha^{[l-1]} \Gamma_{\alpha\beta}^{[l]i} \lambda_\beta^{[l]} \Gamma_{\beta\gamma}^{[l+1]j} \lambda_\gamma^{[l+1]}, \tag{2.33}$$

resulting in the state

$$|\Psi\rangle = \sum_{a,b} \sum_{\alpha,\gamma} \Theta^{ab}_{\alpha\gamma} |a\rangle_l |b\rangle_{l+1} |\Phi^{[l]L}_{\alpha}\rangle |\Phi^{[l+1]R}_{\gamma}\rangle, \tag{2.34}$$

and requires $\mathcal{O}(\chi^3 d^2 + \chi^2 d^4)$ operations:

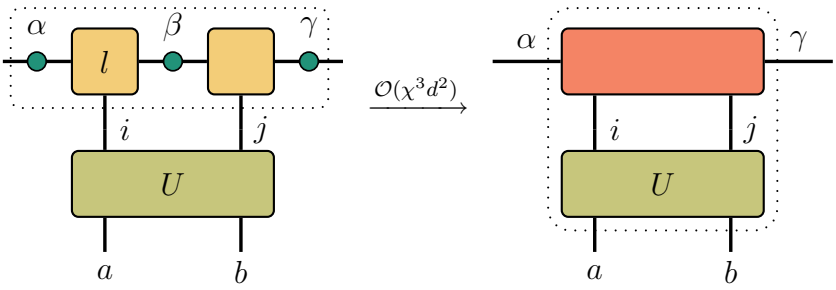

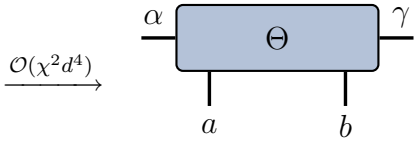

. (2.35)

By introducing Θ, the MPS has lost the bond between sites l and $l+1$. Therefore, to reintroduce the canonical form, one has to perform a Schmidt decomposition of the state (2.34), which is mathematically a singular value decomposition (see section 2.1.1) of the matrix $\Theta^{ij}_{\alpha\gamma}$ according to the index partition $(\alpha i) : (\gamma j)$ and can be computed in $\mathcal{O}(\chi^3 d^3)$ basic operations. The original form with updated $\Gamma^{[l]i}_{\alpha\beta}$, $\lambda^{[l]}_{\beta}$ and $\Gamma^{[l+1]j}_{\beta\gamma}$ can then be restored, simply by multiplying the state by the inverse of $\lambda^{[l-1]}_{\alpha}$ and $\lambda^{[l+1]}_{\gamma}$ from the left and the right respectively,

$$\Theta^{ij}_{\alpha\gamma} \overset{\text{SD}}{=} \sum_{\beta}^{\chi_i} L^{i}_{\alpha\beta} \tilde{\lambda}^{[l]}_{\beta} R^{j}_{\beta\gamma} = \sum_{\beta}^{\chi_i} \lambda^{[l-1]}_{\alpha} \tilde{\Gamma}^{[l]i}_{\alpha\beta} \tilde{\lambda}^{[l]}_{\beta} \tilde{\Gamma}^{[l+1]j}_{\beta\gamma} \lambda^{[l+1]}_{\gamma}. \tag{2.36}$$

Since $\chi_i = \chi d > \chi$, only the largest χ terms should be kept in order to bring the state back in its original truncated MPS representation. At this point, the error introduced can be evaluated using equation (2.20). After building Θ and performing the truncation in the Schmidt decomposed form, the full state is represented in a newly adapted Hilbert space, with the same

dimensionality as before. Equation (2.36) can be visualised via

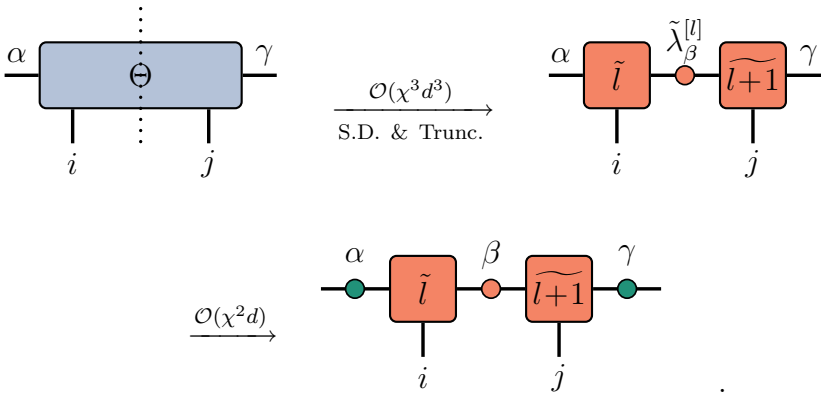

. (2.37)

These two steps (2.35) and (2.37) form the heart of the TEBD algorithm.

Suzuki-Trotter Decomposition

The TEBD algorithm for simulating the time evolution of a 1D quantum state consists of using steps (2.35) and (2.37) to apply small next-neighbour time evolution operators. Thereby, efficient simulation of any slightly entangled 1D state becomes possible. The only condition is that the Hamiltonian $\hat{H}_{\mathrm{NN}}$ contains only next-neighbour terms and can therefore be written as sum over two-site Hamiltonians $\hat{H}_{\mathrm{NN}} \equiv \sum_j^{N-1} \hat{H}_{j,j+1}$. Then, the full time evolution operator

$$\hat{U}_{\mathrm{NN}}(\Delta t) \equiv e^{-i\hat{H}_{\mathrm{NN}}\Delta t} = e^{-i\sum_j^{N-1}\hat{H}_{j,j+1}\Delta t}, \tag{2.38}$$

($\hbar \equiv 1$) can be expressed via a Suzuki-Trotter Decomposition [28] as product of individual next-neighbour evolution gates

$$\hat{U}_{j,j+1} \equiv e^{-i\hat{H}_{j,j+1}\Delta t'}, \tag{2.39}$$

with possibly differing time steps $\Delta t'$. Since, in general, the gates $\hat{U}_{j,j+1}$ do not commute with each other, this expansion is an approximation with an error depending on the size of the commutators between different terms and on the time step. For instance, the simplest decomposition would be a first order expansion of an operator $e^{(\hat{A}+\hat{B})\Delta t}$ with $[\hat{A}, \hat{B}] \neq 0$,

$$e^{(A+B)\Delta t} = e^{\hat{A}\Delta t}e^{\hat{B}\Delta t} + \mathcal{O}(\Delta t^2), \tag{2.40}$$

which simply follows from the standard Baker-Hausdorff identity. Thus, for $\hat{U}_{\mathrm{NN}}(\Delta t)$, a possible first order expansion into next-neighbour gates would be

to use (2.40) with $e^{\hat{A}} \equiv \prod_j e^{-i\hat{H}_{2j,2j+1}}$ and $e^{\hat{B}} \equiv \prod_j e^{-i\hat{H}_{2j+1,2j+2}}$. If the gates $e^{-i\hat{H}_{j,j+1}\Delta t}$ for even j are consecutively applied via (2.35) and (2.37), followed by all odd-j-gates, the time evolution over a small time step Δt of the full MPS is simulated up to an error of $\mathcal{O}(\Delta t^2)$.

However, for better performance in general higher-order expressions are desired. For example, a second order decomposition can be simply achieved via

$$e^{(A+B)\Delta t} = e^{\hat{A}\Delta t/2} e^{\hat{B}\Delta t} e^{\hat{A}\Delta t/2} + \mathcal{O}(\Delta t^3). \tag{2.41}$$

Therefore, for a second order expansion, consecutively the gates $e^{-i\hat{H}_{j,j+1}\Delta t'}$ with even j have to applied with half a time-step $\Delta t' = \Delta t/2$, followed by all full time-step gates $e^{-i\hat{H}_{j,j+1}\Delta t}$ for odd j-values.

Even higher order expressions have been systematically analysed in [29]. For our TEBD algorithm, we define a sweep $\hat{P}_{\Delta t'}$ as the consecutive implementation of the gates (2.39) as

$$\hat{P}^T_{\Delta t'} \equiv \hat{U}_{1,2}\hat{U}_{2,3}\hat{U}_{3,4}\ldots\hat{U}_{N-1,N}. \tag{2.42}$$

As presented in [29], an n-th order method can be implemented, by applying $\hat{P}_{\Delta t'}$ and its transposed version in an adequate order. Specifically, we use a 4th order decomposition, for which $\Delta t' = \Delta t/12$ and which reads

$$\begin{aligned}\hat{U}_{\mathrm{NN}}(\Delta t) = {} & \hat{P}_1^T\hat{P}_1\hat{P}_1^T\hat{P}_{-2}\hat{P}_1^T\hat{P}_1^T\hat{P}_1^T\hat{P}_1^T\hat{P}_1\hat{P}_1^T\hat{P}_1\hat{P}_1\hat{P}_1\hat{P}_1\hat{P}_{-2}^T\hat{P}_1\hat{P}_1^T\hat{P}_1 \\ & + \mathcal{O}(\Delta t^5).\end{aligned} \tag{2.43}$$

Thus, the simulation of a full Δt time step up to an error of $\mathcal{O}(\Delta t^5)$ requires a total of $[18(N-1)]$ applications of next-neighbour gates, according to (2.35) and (2.37). Hence, $\mathcal{O}(N\chi^3 d^3)$ basic operations for such a single time step are required, using the TEBD algorithm in our case.

Imaginary Time Evolution

TEBD is not only limited to real time evolution, it also supports the calculation of ground states for any one-dimensional next-neighbour Hamiltonian. This can be achieved by simply simulating evolution in negative imaginary time. It is easy to verify that the ground state of a system can be written as

$$|\Psi_G\rangle = \lim_{\tau\to\infty} \frac{e^{-\hat{H}\tau}|\Psi_0\rangle}{\|e^{-\hat{H}\tau}|\Psi_0\rangle\|}, \tag{2.44}$$

with some initial state $|\Psi_0\rangle$, as long as the overlap of this state with the ground state is non-zero, $\langle\Psi_0|\Psi_G\rangle \neq 0$, and there exists an energy gap

between the ground an the first excited state $\Delta \equiv E_1 - E_0 > 0$. Then, $|\Psi_0\rangle$ can be expanded in its energy eigenbasis $\{|E_n\rangle\}$ with eigenenergies $E_0 < E_1 < \ldots$,

$$|\Psi_0\rangle = \sum_{n=0} c_n |E_n\rangle \tag{2.45}$$

and therefore

$$\begin{aligned} |\Psi_G\rangle &\propto \lim_{\tau\to\infty} \sum_n e^{-E_n\tau} c_n |E_n\rangle \\ &\propto \lim_{\tau\to\infty} \left(c_o|E_0\rangle + \sum_n e^{-(E_n-E_0)\tau} c_n \right) = c_0|E_0\rangle, \end{aligned} \tag{2.46}$$

since $(E_n - E_0) > 0$. Thus, by evolving a MPS in imaginary time steps $\Delta\tau = -i\Delta t$ and keeping it normalised, it converges to the ground state of the system. The normalisation step is ideally performed after each application of a two-site operation, when building the matrix Θ in (2.35).

Note that especially for infinite systems discussed below in section 2.2, the conditions $\langle\Psi_0|\Psi_G\rangle \neq 0$ and $\Delta > 0$ are not necessarily fulfilled and special care should be taken. A quality check for a calculated ground state $|\Psi_c\rangle$ can for example be performed by simulating the real time evolution of this state under the same time-independent Hamiltonian. The aim is then to verify, that physical quantities like long-range expectation values do not change on long timescales, thus ensuring the fact that $|\Psi_c\rangle$ is at least an eigenstate. Additionally, as for the real time evolution, convergence in the truncation parameter χ and the time-step Δt has to be tested.

This procedure for calculating ground states turns out to be very robust against numerical noise. This can be understood because of the fact that a corrupted intermediate state calculated during imaginary time evolution can in principle again be considered as a new initial state $|\Psi_0\rangle$. Furthermore, numerical noise even helps to fulfil the condition $\langle\Psi_0|\Psi_G\rangle \neq 0$. Note that because of the equivalence of the MPS representation to the DMRG state representation [11], in principle also the standard variational DMRG techniques can be used to obtain a MPS ground state, which can then be further used for real time simulations within TEBD. The advantage of the standard DMRG technique is that it converges faster than an imaginary time-evolution within TEBD.

Orthogonality Problems

Another important issue when applying a general two-site gate $\hat{V}_{j,j+1}$ to a MPS is that it might lead to non-orthogonality and therefore destroy the

canonical form of the MPS. This can arise either in the case of non-unitary operators like in imaginary time evolution, or even for unitary operators due to the truncation step. Consider, for example the following situation of an initially canonical MPS

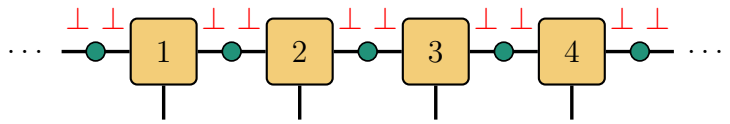

. (2.47)

The $\perp$ symbols are denoting orthogonality of the Schmidt bases to the left (left symbol) and to the right (right symbol) if the state would be expanded at a specific bond according to (2.17). Consider now the situation after the two processes in the application of a next-neighbour non-unitary gate $\hat{V}$

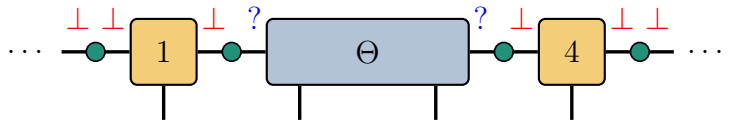

(2.48)

and

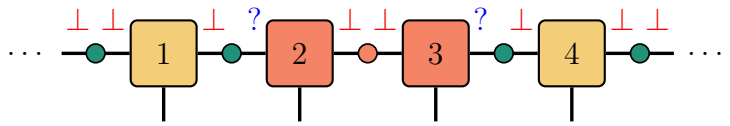

. (2.49)

In expression (2.48), the Θ matrix has been built within an expansion in the Schmidt basis $\{|\Phi^L_{12}\rangle\}$, where "12" stands for the bond index between 1 and 2, and $\{|\Phi^R_{34}\rangle\}$. Thus, by applying $\hat{V}$, these basis states, and all others to the left and the right respectively are not modified and remain orthonormal. However, the former bases $\{|\Phi^R_{12}\rangle\}$ and $\{|\Phi^L_{34}\rangle\}$ have been absorbed into Θ with an unknown result in terms of orthonormality. Unfortunately, by the singular value decomposition leading to (2.49), only for $\{|\Phi^L_{23}\rangle\}$ and $\{|\Phi^R_{23}\rangle\}$ is orthonormality explicitly reintroduced. If $\hat{V}$ were unitary, the orthonormal states $\{|\Phi^R_{12}\rangle\}$ and $\{|\Phi^L_{34}\rangle\}$, transformed into Θ would have been remained orthonormal throughout the whole process. But in the general non-unitary case (2.49) has lost its canonical form. Note that this problem arises not only due to explicitly non-unitary operators applied during imaginary time evolution, but also due to the truncation of the bases after a Schmidt decomposition, also in real time evolution.

There are three possible solutions to this problem. In the case of imaginary time evolution, where the non-unitarity arises mainly from the operator itself, one can reduce this problem by using a very small time-step. Then, $e^{-\hat{H}_{j,j+1}\Delta\tau}$ gets very close to the unitary identity operator and the orthogonality error becomes small, with orthonormality being reintroduced at each bond in the system during the corresponding singular value decomposition. However, this is not quite satisfying, since the purpose of implementing a high order Suzuki-Trotter expansion was partly to avoid having to use an extremely small time-step. The second possibility is to apply a general orthogonalisation scheme, working for any non-canonical MPS, which has been introduced in [30]. However, in our case it is more efficient to use the fact that the state (2.49) only suffers from 2 out of $2(N-1)$ non-orthogonal basis sets. Consider, for example the sets $\{|\Phi^L_{23}\rangle\}$ and $\{|\Phi^R_{45}\rangle\}$, which are both orthonormal. The first set is orthonormal due to the preceding Schmidt decomposition and the second one due to that fact that it has not yet been modified. Due to their orthonormality, it is no problem to apply a non-unitary operator $\hat{V}$ between sites 3 and 4, resulting in

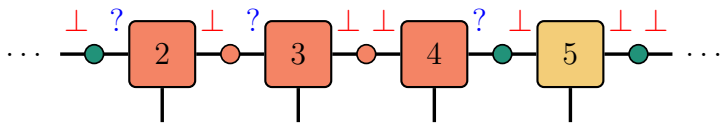

. (2.50)

On the other hand, in (2.49) it would have also been possible to act with a gate between sites 1 and 2, or once again on 2 and 3. Even better, also in (2.50), a gate-application to the left (sites 2,3) or to the right (sites 4,5) of the previously created bond index (34) or between 3 and 4 itself is possible. This holds in general: Schmidt bases might lose their orthogonality, but some relevant sets will always remain orthonormal, so that in any case an operation to the left or to the right of the previous gate or at the same location is always possible, assuming that the initial state was in a canonical form prior to the previous operation.

Thus, in the Suzuki-Trotter decomposition (2.43) used in our algorithm, no problem arises, as long as a sweep $\hat{P}_{\Delta t'}$ is followed by a transposed sweep $\hat{P}^T_{\Delta t'}$ or the other way along the sites. Unfortunately products like $\hat{P}^T_1\hat{P}^T_1$ or $\hat{P}_1\hat{P}_1$ appear in (2.43). This leads to following situations after applying for example $\hat{P}_1$

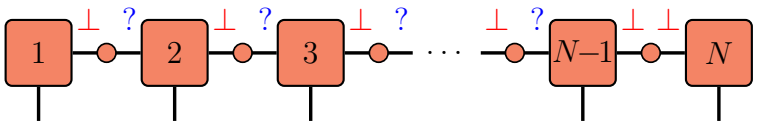

. (2.51)

Implementing $\hat{P}_1$ at this point would fail due to the fact, that the first gate $\hat{U}_{1,2}$ would be applied within the possibly non-orthogonal basis set $\{|\Phi^R_{23}\rangle\}$. This problem can however be easily overcome, by inserting a sweep of two-site (unitary) identity operators

$$\hat{P}^T_{\mathrm{id}} \equiv \mathbb{1}_{2,3}\mathbb{1}_{3,4}\mathbb{1}_{4,5}\ldots\mathbb{1}_{N-2,N-1}, \tag{2.52}$$

changing products of the form $\hat{P}_1\hat{P}_1$ into $\hat{P}_1\hat{P}^T_{\mathrm{id}}\hat{P}_1$ and $\hat{P}^T_1\hat{P}^T_1$ into $\hat{P}^T_1\hat{P}_{\mathrm{id}}\hat{P}^T_1$. Because of the unitarity of the identity operators, applying $\hat{P}^T_{\mathrm{id}}$ to (2.51) for example, leads to

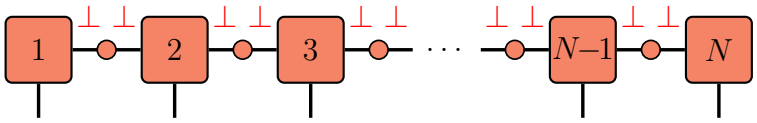

, (2.53)

allowing for an following implementation of $\hat{U}_{1,2}$ and the rest of $\hat{P}_1$.

Hence, to avoid orthogonality issues, the Suzuki-Trotter expansion (2.43) that we use has to be modified to

$$\begin{aligned}\hat{U}^{\mathrm{imag}}_{\mathrm{NN}}(\Delta t) = \hat{P}^T_1\hat{P}_1\hat{P}^T_1\hat{P}_{-2}\hat{P}^T_1\hat{P}_{\mathrm{id}}\hat{P}^T_1\hat{P}_{\mathrm{id}}\hat{P}^T_1\hat{P}_{\mathrm{id}}\hat{P}^T_1\hat{P}_1\ldots \\ \ldots\hat{P}^T_1\hat{P}_1\hat{P}^T_{\mathrm{id}}\hat{P}_1\hat{P}^T_{\mathrm{id}}\hat{P}_1\hat{P}^T_{\mathrm{id}}\hat{P}_1\hat{P}^T_{-2}\hat{P}_1\hat{P}^T_1\hat{P}_1 + \mathcal{O}(\Delta t^5),\end{aligned} \tag{2.54}$$

to allow for example consecutive applications of the full non-unitary imaginary time step evolution operator $\hat{U}^{\mathrm{imag}}_{\mathrm{NN}}(\Delta t)$. Thereby, $[6(N-3)]$ additional gates, each requiring $\mathcal{O}(\chi^3 d^3)$ basic operations have to be added, not changing the overall complexity of $\mathcal{O}(N\chi^3 d^3)$ for a single time-step.

Note that the state (2.53) is in a fully canonical form. To obtain physically useful results, it is important to ensure that expectation value evaluations only take place if this is the case! Thus, before calculating expectation values after certain time steps in imaginary time evolution simulations, the identity sweep $\hat{P}_{\mathrm{id}}$ has to be performed.

2.1.4 Practical Considerations

Our implementation of the TEBD algorithm is fully written in stand alone C-Code. For the singular value decomposition, the *LAPACK* routines *ZGESVD* for real and *DGESVD* for imaginary time evolutions are utilised. In most real time evolution cases a time-step, of 0.1 in the units of the energy scale suffices due to the 4th order Suzuki-Trotter decomposition if the eigenenergies of the Hamiltonian are of the order of one. Typical values of χ are ranging from 10–100, strongly depending on the physical system and the entanglement contained in it, of course. Depending on the magnitude of the gap between a ground and a first excited state, the order of imaginary time-steps required to produce a fully converged matrix product ground state ranges between 1000 an 10000.

Product States

The typical numerical procedure consists of calculating a ground state, and afterwards simulating the real time evolution whilst changing some external parameters. The initial state before starting the imaginary time evolution is typically a product state, which can be easily translated into the MPS language, since

$$\begin{aligned} |\Psi_{\text{prod}}\rangle &\equiv \left(\sum_{i_1} c_{i_1}|i_1\rangle\right) \otimes \left(\sum_{i_2} c_{i_2}|i_2\rangle\right) \otimes \ldots \left(\sum_{i_N} c_{i_N}|i_N\rangle\right) \\ &= \sum_{i_1,i_2,\ldots,i_N} c_{i_1} c_{i_2} \ldots c_{i_N} |i_1 i_2 \ldots i_N\rangle \end{aligned} \tag{2.55}$$

and the coefficients c_{i_m} can always be chosen to fulfil

$$c_{i_1} c_{i_2} \ldots c_{i_N} \stackrel{!}{=} \sum_{\alpha_1}^{\chi_1} \sum_{\alpha_2}^{\chi_2} \cdots \sum_{\alpha_{N-1}}^{\chi_{N-1}} \Gamma_{\alpha_1}^{[1]i_1} \lambda_{\alpha_1}^{[1]} \Gamma_{\alpha_1\alpha_2}^{[2]i_2} \lambda_{\alpha_2}^{[2]} \ldots \lambda_{\alpha_{N-1}}^{[N-1]} \Gamma_{\alpha_{N-1}}^{[N]i_N} \tag{2.56}$$

by setting $\lambda_{\alpha_l}^{[l]} = \delta_{\alpha_l,0}, \forall\ 1 \leq l < N$ and $\Gamma_{00}^{[m]i_l} = c_{i_l}, \forall\ 1 \leq m \leq N$.

Numerical Improvements

There are some numerical tricks used in our code to significantly improve performance and accuracy of the TEBD algorithm.

The first one is to use an adaptive value of χ for each bond between the sites. Consider for example the first bond in the MPS decomposition (2.16). The maximum possible value for the index α_1, $\chi_1 = d$ is equal to the in

general small local dimension of the Hilbert space. Thus, due to boundary effects a relevant amount of computational resources can be saved if d is small, by not using a fixed value of χ for all bonds, but an adaptive one, depending on the maximum χ value actually required. We define a small zero-threshold for the value of any λ, and before each application of a two site gate, the χ-values for each bond between sites relevant for this operation is determined by the threshold. Then, for the contractions and the singular value decomposition, only these $\chi_n \leq \chi$-values are used instead of χ. This not only improves the performance due to the boundary effects, but even more in the case, that little entanglement is present at a certain bond. This occurs for all bonds during the first few time-steps, provided one starts in a non-entangled product state.

In the second step of the scheme to apply a two-site evolution operator (2.37), the newly created Γ-arrays have to be multiplied by λ^{-1} values to restore the original MPS form. Since these values can become extremely small, this step is problematic due to numerical errors arising from a division of small numbers close to the specific data type precision. This can be overcome by using a threshold value above the critical precision of the used data type below which the division isn't performed. Note that the corresponding number in the Γ-array is anyway irrelevant. Alternatively, we may keep track of the position in the MPS where a λ-matrix has been multiplied to a Γ-array and always store Γ-arrays multiplied by λ-vectors to the left or the right. Thereby one finds, that for the way TEBD is implemented in our case, the division is actually never required. Suppose for example, that a two site evolution gate has been applied on sites 2 and 3 of a MPS, without exhibiting the λ-division in (2.37)

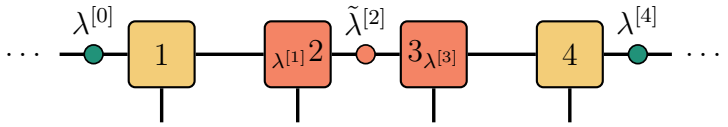

. (2.57)

If we now just remember, as indicated in (2.57), that $\lambda^{[1]}$ and $\lambda^{[3]}$ are multiplied into the Γ-arrays 2 and 3 respectively, we can now easily evaluate the next step in the time evolution process. This is because our Suzuki-Trotter decomposition has been implemented in a way that the next gate after (2.57) in any case acts on 1 and 2 or 3 and 4. In both cases, $\lambda^{[2]/[3]}$ would have to be multiplied to Γ-array 2 or 3 again, to build the Θ matrix in (2.35). This, and the preceding division can therefore anytime be fully avoided.

There is another way to tremendously improve the performance of the TEBD algorithm. This is the optimisation of storage and manipulation of

the state representation due to the implementation of physical conservation laws. Unfortunately, for the physical problems discussed in this thesis, such improvements are either not possible because this could not yet be implemented for infinite system (Superfluid boson currents, chapter 3; iTEBD algorithm, Section 2.2), or is not very advantageous in a finite system of Rydberg atoms (Chapter 5), where the number of excitations is not constant in time.

2.1.5 A Test System: Ising Model

We are going to compare our TEBD algorithm with a small exactly solvable spin model for $N = 10$ sites. We choose an Ising model with a transverse field, i.e. the Hamiltonian

$$\hat{H} \equiv \sum_{n}^{N-1} \hat{\sigma}_n^x \hat{\sigma}_{n+1}^x + h_z \sum_{n}^{N} \hat{\sigma}_n^z, \tag{2.58}$$

where $\hat{\sigma}_n^x$ and $\hat{\sigma}_n^z$ denote the Pauli spin operators at site n defined by

$$\begin{aligned} \hat{\sigma}_n^x \, |\uparrow\rangle_n &\equiv |\downarrow\rangle_n & \hat{\sigma}_n^x \, |\downarrow\rangle_n &\equiv |\uparrow\rangle_n \\ \hat{\sigma}_n^z \, |\uparrow\rangle_n &\equiv |\uparrow\rangle_n & \hat{\sigma}_n^z \, |\downarrow\rangle_n &\equiv -|\downarrow\rangle_n, \end{aligned} \tag{2.59}$$

and h_z is an magnetic field in z direction.

We expect the most interesting behaviour at the quantum critical field of $h_z = 1$. We are going to test the real time simulation of the total magnetisation $M_z \equiv \sum_k \langle \hat{\sigma}_k^z \rangle$ and the ground state spin-spin correlation $\langle \hat{\sigma}_0^z \hat{\sigma}_k^z \rangle$.

In figure 2.2 we plot M_Z as the system evolves under Hamiltonian (2.58) with $h_z = 1$, initially starting in the state $|\downarrow\rangle^{\otimes 10}$. Time-steps are of the size $\Delta t = 0.1$ and we are utilising truncation parameters $\chi = 4, 8, 16, 32$. We find that for increasingly large χ the evolution is represented correctly up to larger times, i.e. the curves are converging to the exact one. This indicates that bipartite entanglement is emerging during time-evolution. For $\chi = 16$, the magnetisation is already satisfactorily reproducing the exact evolution with errors of less than 1%.

We expect the results to become exact when employing a truncation parameter of $\chi = 32$, since in a 10-qubit system the maximally entangled state residing in in a bipartite splitting at the centre of the chain can be expressed exactly with $2^5 = 32$ Schmidt basis states. Indeed, in figure 2.3 we find that the largest truncation error occurring during each time-step, is drops to values markedly below machine precision, when $\chi = 32$ in contrast to the case of $\chi = 31$. Furthermore, figure 2.2 indicates that the total difference

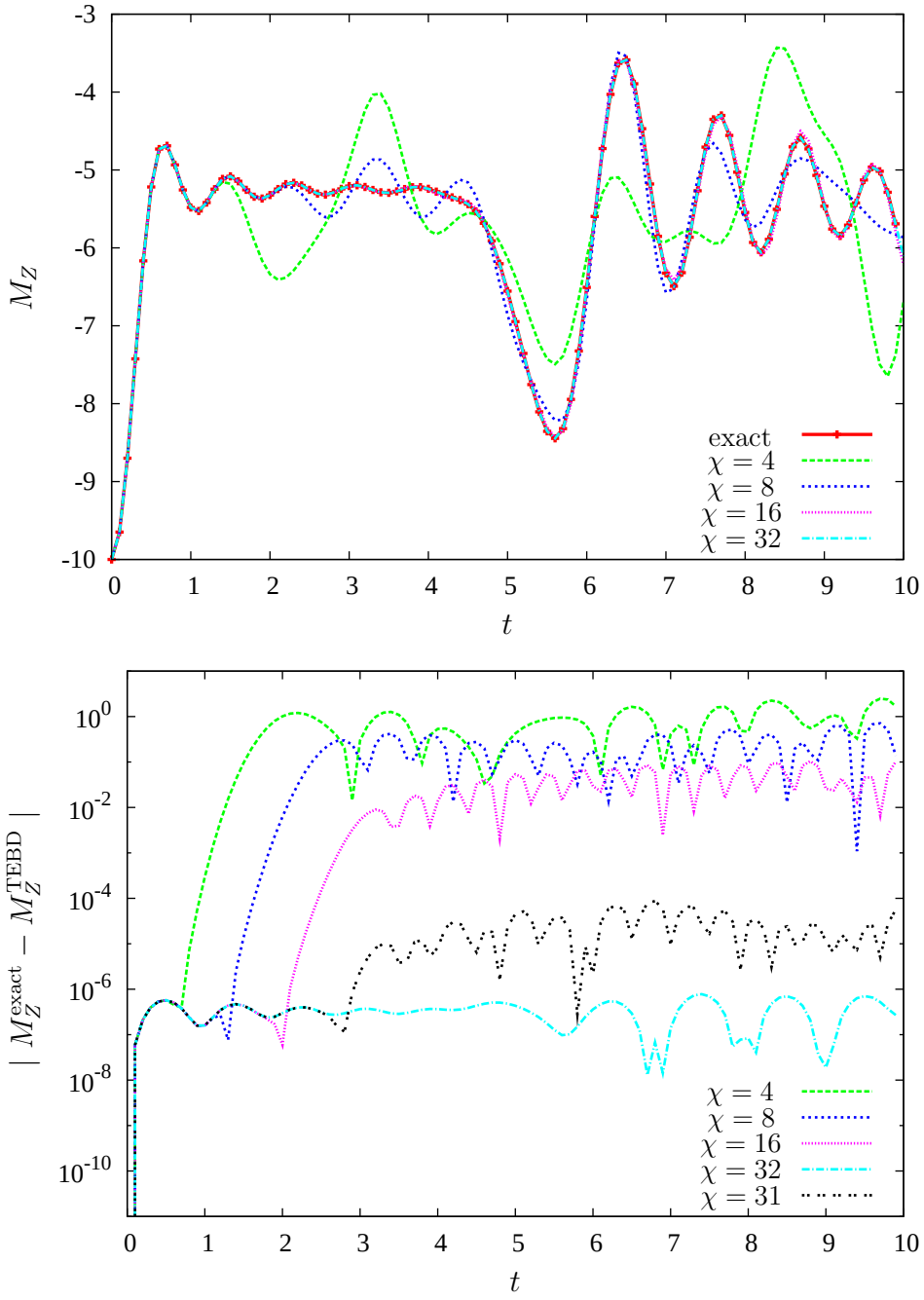

Figure 2.2: Comparison of the time evolution of the magnetisation M_z from an exact diagonalisation of the full Hamiltonian (2.58) to results from the TEBD algorithm, employing several values of the Hilbert space truncation parameter $\chi = 4, 8, 16, 32$. The initial state is $|\downarrow\rangle^{\otimes 10}$. The lower picture shows the absolute differences to the exact results. $\Delta t = 0.1$.

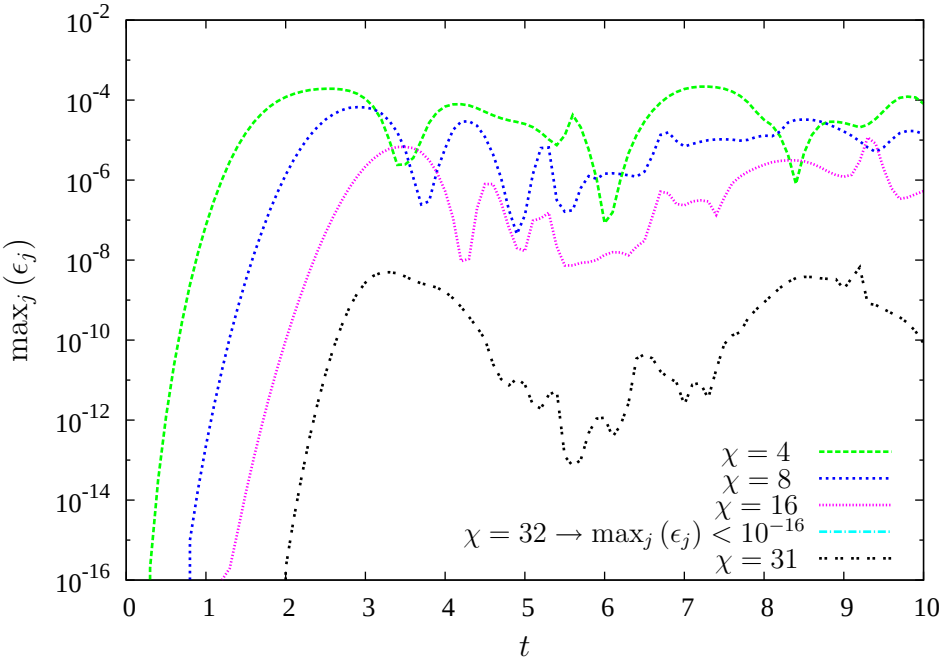

Figure 2.3: The largest truncation error (Equation (2.20)) occurring in each time-step for the simulations of figure 2.2. For $\chi = 32$ the error is below machine precision at all times.

in the magnetisation remains constant at values of approximately 10^{-8}–10^{-6} throughout the whole time evolution process in the $\chi = 32$ case. Therefore, we conclude that this is the size of the error due to the Trotter expansion and other numerical noise processes.

In figure 2.4 we additionally visualise the emergence of entanglement by plotting the von Neumann entropy S from equation (2.8) for each bipartite splitting (bond) in the system. We observe oscillations with a maximum value of approximately $S = 3$. Thus, we conclude that truncation parameters, which are at least larger than $\chi > 2^3 = 8$ are required to represent the quantum states during the time evolution. However, comparing this to above results we find that χ has to be markedly larger than this lower limit to obtain faithful representations.

We obtain similar results concerning the convergence in χ, when performing ground state calculations and comparing the spin-spin correlation $\langle \hat{\sigma}_0^z \hat{\sigma}_k^z \rangle$ to exact values. However, we find out that the ground state contains only very little entanglement and much smaller χ-values are sufficient. In figure 2.5 we plot results from imaginary time-evolution over 1000 time-steps $\Delta t = 0.1$ within the TEBD algorithm for values of $\chi = 2, 4, 8, 16$. We plot

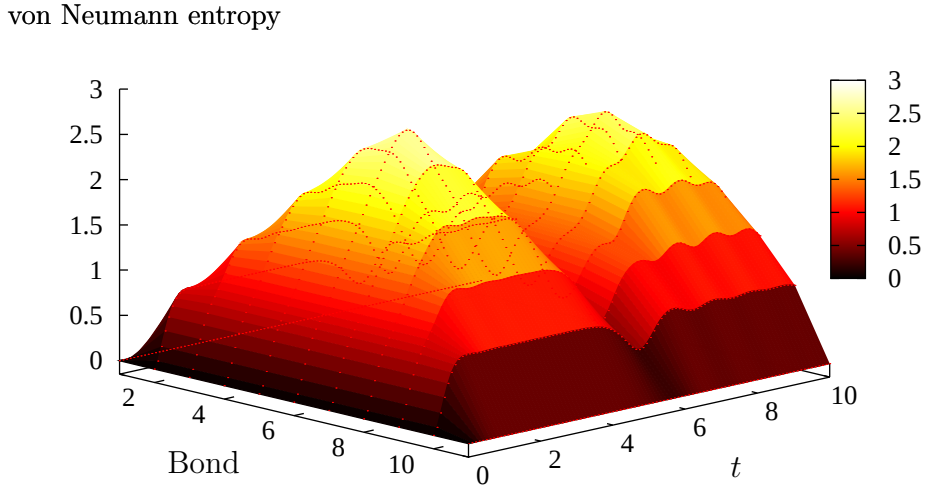

Figure 2.4: The von Neumann entropy as a function of time for all bipartite splittings (Bonds) for the evolution process of figure 2.2. $\chi = 32$.

$\langle \hat{\sigma}_0^z \hat{\sigma}_k^z \rangle$ and the differences to the exact results for sites ranging from 1 to 10. Already for $\chi = 4$ we find excellent agreement with the exact spin-spin correlation. The von Neumann entropy in the centre of the system is only $S_{\mathrm{GS}} \approx 0.55$!

Finally, we want to give some benchmark values for the computational time required for typical simulations. For the model (2.58) on our hardware[2], 100 imaginary time-steps can be performed within the following runtimes, depending on χ and the system size N (For comparability, adaptive χ optimisations have been switched off):

	$\chi = 40$	$\chi = 70$	$\chi = 100$
$N = 40$	10 min	50 min	2.6 h
$N = 70$	16 min	1.3 h	4.0 h
$N = 100$	22 min	1.7 h	5.3 h

For real time steps, this table modifies to:

[2]Intel Xeon 5345 (2.33 GHz) CPU, 8 GB RAM, GNU C-Compiler 4.1.2

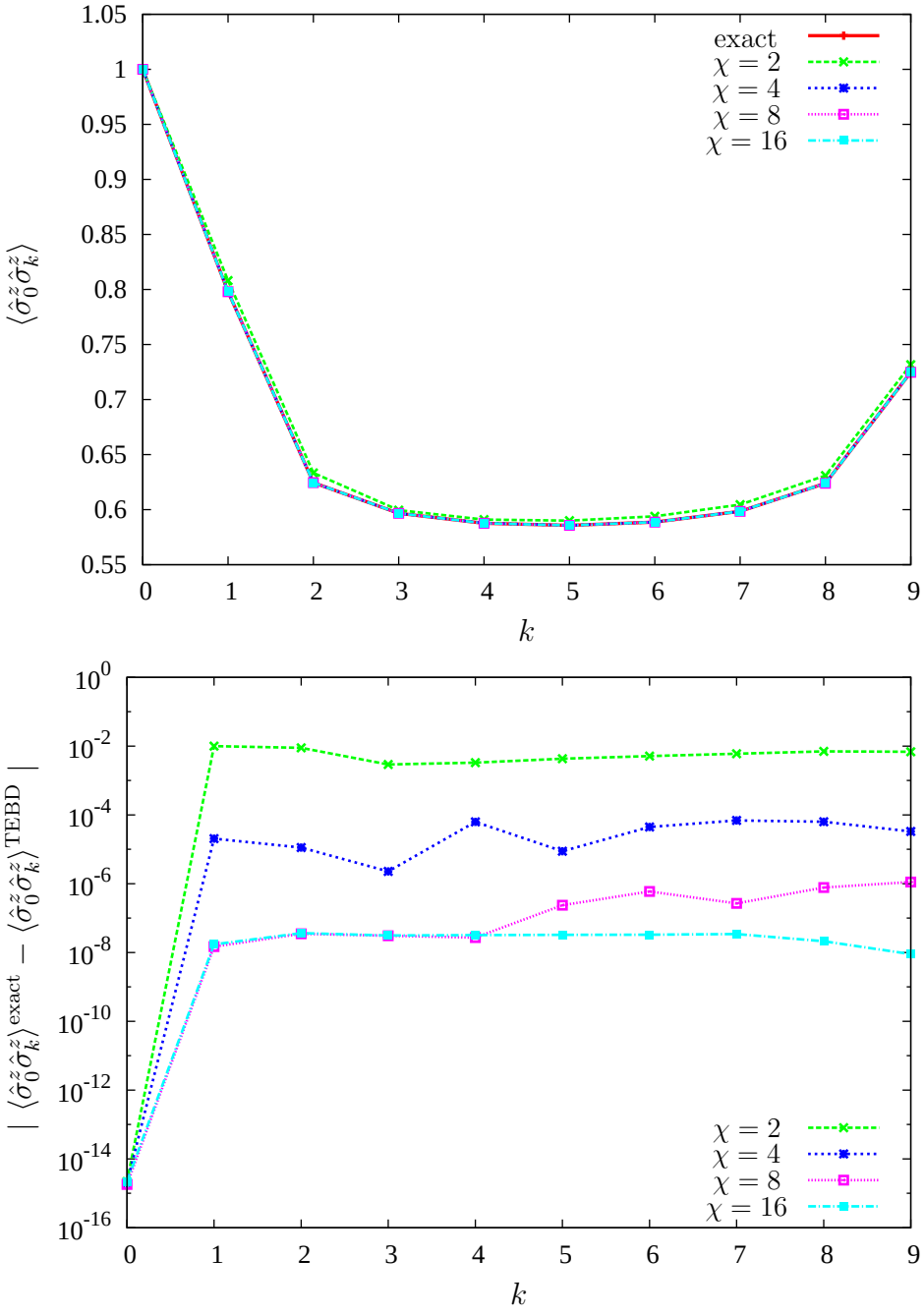

Figure 2.5: Comparison of the spin-spin correlation $\langle\hat{\sigma}_0^z\hat{\sigma}_k^z\rangle$ (Sites 1–10) of the ground state from an exact diagonalisation of the full Hamiltonian (2.58) to results from imaginary time evolution within the TEBD algorithm, employing several values of the Hilbert space truncation parameter $\chi = 2, 4, 8, 16$. The lower picture shows the absolute differences to the exact results.

	$\chi = 40$	$\chi = 70$	$\chi = 100$
$N = 40$	20 min	1.8 h	5.4 h
$N = 70$	30 min	2.4 h	9.4 h
$N = 100$	42 min	3.2 h	11.3 h

The results are roughly consistent with the expected complexity of $\mathcal{O}(N\chi^3 d^3)$ and we find that ground state calculations and real time simulations of spin-systems with more than 100 sites can be achieved within affordable computational resources, if the entanglement is bounded by a value $S_{\max} \ll \log_2(100)$.

2.2 Infinite TEBD (iTEBD)

So far, the TEBD algorithm has been presented for one-dimensional finite quantum systems. Many physical problems, appearing for example in solid state physics are of such large dimensions, that they are considered to be infinite in analytical models, thereby completely ignoring boundary effects. In this chapter, we want to introduce a version of the TEBD algorithm, that allows the near exact simulation of purely infinite systems, by exploiting translation symmetries. The infinite TEBD algorithm (iTEBD) was developed by G. Vidal [10].

2.2.1 State Representation

Attempts have been made to simulate infinite systems by extrapolating results from finite systems with an increasing number of sites. These methods are slow because of the fact, that large amounts of arrays have to be handled and furthermore suffer from large uncertainties in the final results. However, quite surprisingly one actually only needs a very few number of sites to implement the simulation of an translationally invariant infinite system.

Translation Invariance

As in the TEBD algorithm, we are going to use a matrix product state representation (MPS). Consider an infinite chain of local Hilbert spaces, each of dimension d. The state of the system can be written in terms of the Schmidt bases, to the left and the right of a certain bond b, $\{|\Phi_\alpha^{[b]L/R}\rangle\}$

$$|\Psi\rangle \equiv \sum_{\alpha}^{\chi} \lambda_\alpha^{[b]} |\Phi_\alpha^{[b]L}\rangle |\Phi_\alpha^{[b]R}\rangle, \tag{2.60}$$

where the $\lambda_\alpha^{[b]}$ denote the Schmidt coefficients (see section 2.1.1). In general, χ will be infinite in this case, but we are again going to set χ to a finite value, truncating highly entangled basis states and verify the validity of this approximation by convergence tests. Like in equation (2.10), we now expand the vectors $|\Phi_\alpha^{[b]R}\rangle$ into the orthonormal Schmidt bases to the right of bond $b+1$, $\{|\Phi_\beta^{[b+1]R}\rangle\}$ with coefficients $\lambda_\beta^{[b+1]}$, and the local basis of the site between bond b and $b+1$, $\{|i_b\rangle\}$. Therefore, we introduce the three-index array $\Gamma_{\alpha\beta}^{[b]i_b}$,

$$|\Phi_\alpha^{[b]R}\rangle \equiv \sum_\beta^\chi \sum_{i_b}^d \Gamma_{\alpha\beta}^{[b]i_b} \lambda_\beta^{[b+1]} |i_b\rangle |\Phi_\beta^{[b+1]R}\rangle. \tag{2.61}$$

Inserting (2.61) into (2.60) results in the state representation

$$|\Psi\rangle = \sum_{\alpha,\beta}^\chi \sum_{i_b}^d \lambda_\alpha^{[b]} \Gamma_{\alpha\beta}^{[b]i_b} \lambda_\beta^{[b+1]} |i_b\rangle |\Phi_\alpha^{[b]L}\rangle |\Phi_\beta^{[b+1]R}\rangle. \tag{2.62}$$

In the diagrammatic notation, equation (2.62) is written as

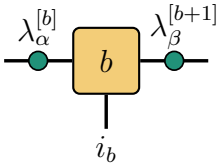

. (2.63)

We now assume, that $|\Psi\rangle$ is translationally invariant by shifts of a single site, which means that exactly the same state vector results from a representation at site $b+1$ instead of b,

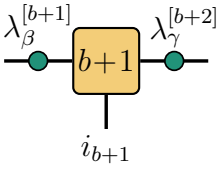

. (2.64)

Hence it follows, that $\lambda_\alpha^{[b]} = \lambda_\beta^{[b+1]} = \lambda_\gamma^{[b+2]} = \cdots \equiv \lambda$, and we only require one λ to appear in the full state expansion. In the same way $\Gamma^{[b]} = \Gamma^{[b+1]} = \Gamma^{[b+2]} = \cdots \equiv \Gamma$, and therefore only one Γ-array is required, too. Thus, by only storing one Γ and one λ, a full infinite system can be represented via

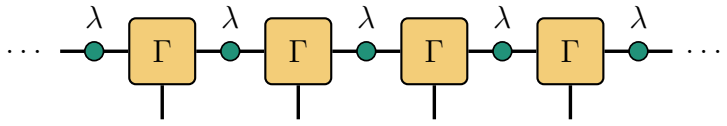

. (2.65)

Translation Invariance by two-site Shifts

As in section 2.1, we are going to want to simulate time evolution by repeated application of small next-neighbour evolution gates in a Suzuki-Trotter decomposition. Unfortunately, these gates act on two subsequent sites and are therefore partially breaking the invariance of representation (2.65). Thus, we simply go one step further and expand the basis vectors $|\Phi_\beta^{[b+1]R}\rangle$ from bond $b+1$ in equation (2.61) into the Schmidt basis at bond $b+2$, $\{|\Phi_\gamma^{[b+2]R}\rangle\}$ with Schmidt coefficients $\lambda_\gamma^{[b+2]}$, and the local basis at site $b+1$, $\{|i_{b+1}\rangle\}$. This leads to a two-site representation

$$|\Psi\rangle = \sum_{\alpha,\beta,\gamma}^{\chi} \sum_{i_b,i_{b+1}}^{d} \lambda_\alpha^{[b]} \Gamma_{\alpha\beta}^{[b]i_b} \lambda_\beta^{[b+1]} \Gamma_{\beta\gamma}^{[b+1]i_{b+1}} \lambda_\gamma^{[b+2]} |i_b\rangle |i_{b+1}\rangle |\Phi_\alpha^{[b]L}\rangle |\Phi_\gamma^{[b+2]R}\rangle, \quad (2.66)$$

or

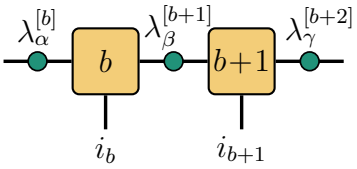

. (2.67)

With the same symmetry argument as above, now assuming invariance by shifts of two sites, it follows that the full infinite state can be represented by just two arrays Γ^A, Γ^B and two λ^A, λ^B as

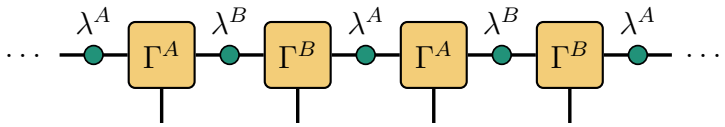

. (2.68)

An infinite MPS (iMPS), as in (2.68) or (2.65) is again called to be in a canonical form, if at each bond it can be expanded in orthonormal Schmidt bases, like in (2.60).

It is important, not to confuse the real infinite state representation (2.68) with the case of simple periodic boundary conditions. For example, a two-qubit system with periodic boundary conditions would be only able to represent states, spanned by the four basis-vectors $|\ldots 01010\ldots\rangle$, $|\ldots 10101\ldots\rangle$, $|\ldots 0000\ldots\rangle$ and $|\ldots 1111\ldots\rangle$, by storing $|01\rangle$,$|10\rangle$, $|00\rangle$ and $|11\rangle$ respectively. In marked contrast, with a two-site infinite MPS representation, the only limitation to the number of basis state used to span an arbitrary infinite 1D state, is the amount of allowed entanglement in the expansion according to χ.

2.2.2 Expectation Values

The computation of any expectation value can be accomplished completely analogous to the finite case in Section 2.1. Simply, instead of the finite MPS in (2.16), the canonical iMPS representation (2.68) expanded up to any desired site difference has to be utilised for the contraction in (2.27).

2.2.3 The Algorithm

The iTEBD algorithm also works analogous to its finite TEBD counterpart, described in Section 2.1. We decompose the real or imaginary time evolution operator, build from the matrix exponential of a two-site translationally invariant Hamiltonian $\hat{H}_{\mathrm{NN,inf}} \equiv \sum_j^\infty \hat{H}_{j,j+1}$, $\hat{U}_{\mathrm{NN,inf}}(\Delta t) \equiv e^{-i\hat{H}_{\mathrm{NN,inf}}\Delta t}$, with small time-step Δt, into next-neighbour gates via a Suzuki-Trotter expansion. The gates are again applied by using steps (2.35) and (2.37) to update the infinite MPS state representation. The only remaining task is to find a sweep $\hat{P}_{\Delta t'}$, ensuring an application of these small gates on the full system. For example, a 4th order decomposition can be performed via

$$\begin{aligned}\hat{U}_{\mathrm{NN,inf}}(\Delta t) = \hat{P}_1^T \hat{P}_1 \hat{P}_1^T \hat{P}_{-2} \hat{P}_1^T \hat{P}_1^T \hat{P}_1^T \hat{P}_1^T \hat{P}_1 \hat{P}_1^T \hat{P}_1 \hat{P}_1 \hat{P}_1 \hat{P}_1 \hat{P}_{-2}^T \hat{P}_1 \hat{P}_1^T \hat{P}_1 \\ + \mathcal{O}(\Delta t^5),\end{aligned} \tag{2.69}$$

with $\Delta t' \equiv \Delta t/12$.

Two-site iTEBD

In the easiest case, a sweep $\hat{P}_{\Delta t'}$ only consists of two gates, denoted by $\hat{U}_{AB} \equiv e^{-i\hat{H}_{j,j+1}\Delta t'}$ and $\hat{U}_{BA} \equiv e^{-i\hat{H}_{j,j+1}\Delta t'}$,

$$\hat{P}_{\Delta t'}^T \equiv \hat{U}_{AB}\hat{U}_{BA}. \tag{2.70}$$

Note that the functional form of $\hat{U}_{AB}$ and $\hat{U}_{BA}$ is exactly the same. Their definition only differs in the state representation they are acting on. $\hat{U}_{AB}$ is applied to an "AB"-state representation

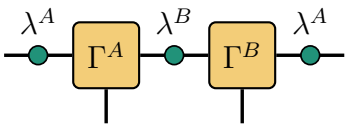

, (2.71)

and is therefore equivalent to the following operation on the full infinite system,

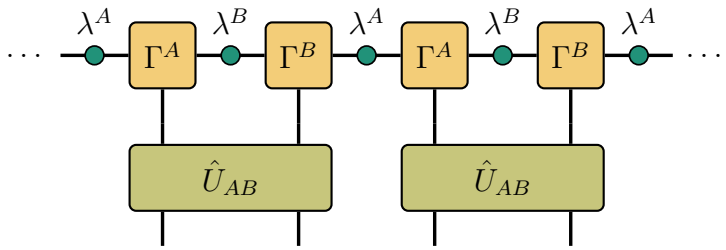

(2.72)

In the same way $\hat{U}_{BA}$ acts on the "BA"-state representation,

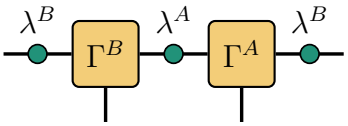

(2.73)

and thus realises the other half of all operations, required to update the full infinite chain under $\hat{P}_{\Delta t'}$,

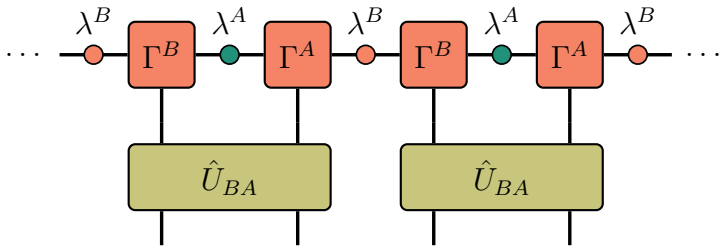

(2.74)

$\hat{U}_{AB}$ updates both Γ-arrays and λ^B, $\hat{U}_{BA}$ the two Γ-arrays and λ^A.

Since the Suzuki-Trotter decomposition (2.43) requires 18 sweeps of the form (2.70), for each full time step only 36 gate applications have to be performed. Due to the singular value decomposition being again the bottleneck in the computation of steps (2.35) and (2.37), a total of $\mathcal{O}(\chi^3 d^3)$ basic operations are required. Note that compared to the finite TEBD algorithm, which utilises $\mathcal{O}(N\chi^3 d^3)$ basic computations, this is even a saving of the order of the number of N operations.

l-site iTEBD

It is important to note that of course the number of two Γ- and two λ-arrays required to apply next-neighbour evolution gates is just a lower bound. If

required, as for example in chapter 3, the whole infinite chain can also be represented by $l > 2$ Γ- and λ-arrays,

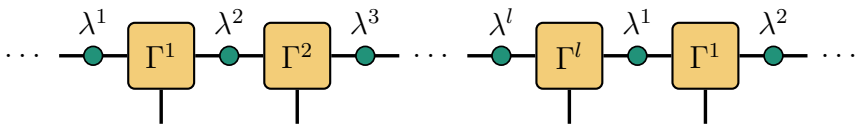

. (2.75)

In this case, the Suzuki-Trotter sweep $\hat{P}_{\Delta t'}$ can be extended to

$$\hat{P}^{(l)\ T}_{\Delta t'} \equiv \hat{U}_{1,2}\hat{U}_{2,3}\ldots\hat{U}_{l-1,l}\hat{U}_{l,1}, \tag{2.76}$$

where $\hat{U}_{i,i+1}$ denotes the evolution operator $e^{-i\hat{H}_{j,j+1}\Delta t'}$, updating Γ^i, Γ^{i+1} and λ_{i+1}. Thus, in general a sweep on representation (2.75) requires l gate operations rendering the overall complexity more precisely to $\mathcal{O}(l\chi^3 d^3)$.

Orthogonality Problems

The problem of possibly non-orthogonal Schmidt bases occurring during imaginary time evolution, or in general during any application of non-unitary gates is also present for the iTEBD algorithm. However, here the problem has to be solved in a slightly different way than in Section 2.1.[3]

Consider the initially two-site canonical iMPS

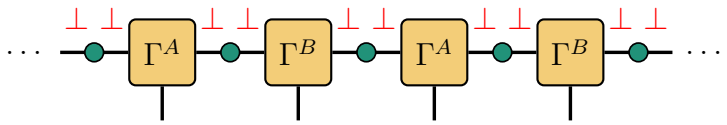

. (2.77)

After applying a non-unitary gate $\hat{V}_{AB}$ to half of the infinite chain, the resulting situation looks like

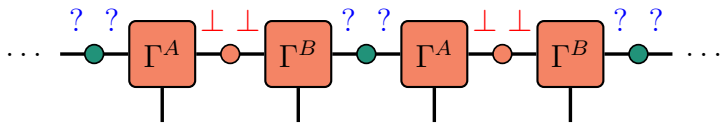

. (2.78)

[3] An alternative scheme to bring back any iMPS into its canonical form has been presented by R. Orus [31]

Thus, we find out that despite of losing the canonical form of the iMPS we are lucky and still can apply a gate $\hat{V}_{BA}$ to the other half of the infinite state, leading to

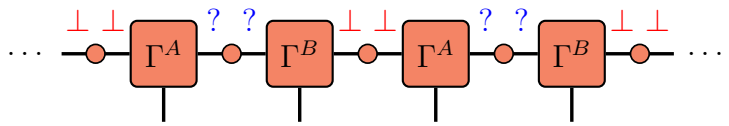

. (2.79)

However, in contrast to the finite case, we now conclude that we are *not* allowed to apply an half-infinite non-unitary gate on the same gate position as the previous one. For example, both, applying $\hat{V}_{AB}$ to (2.78) and using $\hat{V}_{BA}$ on representation (2.79) would fail. Hence, just in contrast to the amendments of identity sweeps in equation (2.54), we now have to avoid terms like $\hat{P}_{\Delta t'}\hat{P}^T_{\Delta t'}$ or $\hat{P}^T_{\Delta t'}\hat{P}_{\Delta t'}$ in the Suzuki-Trotter expansion. Therefore, equation (2.43) can be supplemented by identity operators $\mathbb{1}_{AB}$ and $\mathbb{1}_{BA}$, which act on the half-infinite "AB" chain (2.71) or "BA" chain (2.73) respectively. Then, again with $\Delta t' \equiv \Delta t/12$,

$$\begin{aligned}\hat{U}^{\text{imag}}_{\text{NN,inf}}(\Delta t) = \mathbb{1}_{BA}\hat{P}^T_1\mathbb{1}_{AB}\hat{P}_1\mathbb{1}_{BA}\hat{P}^T_1\mathbb{1}_{AB}\hat{P}_{-2}\mathbb{1}_{BA}\hat{P}^T_1\hat{P}^T_1\ldots\\ \ldots\hat{P}^T_1\hat{P}^T_1\mathbb{1}_{AB}\hat{P}_1\mathbb{1}_{BA}\hat{P}^T_1\mathbb{1}_{AB}\hat{P}_1\hat{P}_1\ldots\\ \ldots\hat{P}_1\hat{P}_1\mathbb{1}_{BA}\hat{P}^T_{-2}\mathbb{1}_{AB}\hat{P}_1\mathbb{1}_{BA}\hat{P}^T_1\mathbb{1}_{AB}\hat{P}_1\\ +\mathcal{O}(\Delta t^5)\end{aligned} \tag{2.80}$$

can be utilised as decomposition of a full time-step, in which orthogonality is guaranteed in every next-neighbour gate application. Note that due to the final $\mathbb{1}_{BA}$ at the end of the expansion, after every time-step Δt, the iMPS is in a fully canonical form and any expectation value evaluation can be performed. This can immediately be seen by applying the unitary operation $\mathbb{1}_{BA}$ on (2.78). By the amendments in equation (2.80) a total of 12 gate applications had to be added, not changing the overall complexity.

The orthogonality problem is a little bit more subtle, if in place of the two-site invariant representation (2.68), an l-site iMPS (2.75) is employed. Consider for example the possibly non-unitary gate $\hat{V}_{1,2}$, performed on an iMPS as the first step of an implementation of $\hat{P}^{(l)}_{\Delta t'}$. The situation afterwards can be expressed as

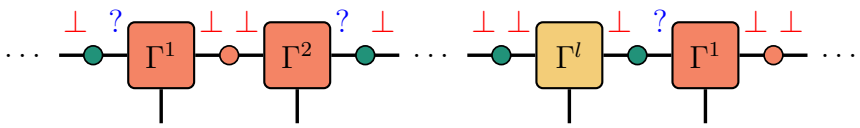

. (2.81)

We find that we would run into problems if we continued with the l-site iTEBD sweep from equation (2.76), since at some point we would have to apply a gate between sites $l-1$ and l with the possibly non-orthogonal basis set to the right of the bond between sites l and 1. Thus, we have to ensure that this basis set remains orthonormal already at this stage. This can be achieved by applying an identity gate between sites l and 1. Due to the fact that the final element of $\hat{P}^{(l)}_{\Delta t'}$ acts between sites l and 1, we also require the Schmidt bases to the right of the bond between 1 and 2 to remain orthonormal. The same care has to be taken for the transposed sweep and additional problems arise if terms like $\hat{P}^{(l)}_{\Delta t'}\hat{P}^{(l)}_{\Delta t'}$ or $\hat{P}^{(l)\,T}_{\Delta t'}\hat{P}^{(l)\,T}_{\Delta t'}$ appear in the Suzuki-Trotter decomposition. Hence, to fully avoid problems for l-site iMPS representations, we are in general already extending the sweep (2.76),

$$\hat{P}^{(l)\ \mathrm{imag}}_{\Delta t'} \equiv \mathbb{1}_{1,2}\mathbb{1}_{l-1,l}\hat{U}_{l,1}\mathbb{1}_{l-2,l-1}\hat{U}_{l-1,l}\ldots\hat{U}_{3,4}\mathbb{1}_{1,2}\hat{U}_{2,3}\mathbb{1}_{l,1}\hat{U}_{1,2} \tag{2.82}$$

and separately define the "transposed" sweep, which is actually *not* related by the transposition operation to (2.82),

$$\hat{P}^{(l)\ \mathrm{imag,transp}}_{\Delta t'} \equiv \mathbb{1}_{l,1}\mathbb{1}_{2,3}\hat{U}_{1,2}\mathbb{1}_{3,4}\hat{U}_{2,3}\ldots\hat{U}_{l-2,l-1}\mathbb{1}_{l,1}\hat{U}_{l-1,l}\mathbb{1}_{1,2}\hat{U}_{l,1}. \tag{2.83}$$

Equations (2.82) and (2.83) inserted into our 4th order Suzuki-Trotter decomposition (2.69) guarantees full orthogonality throughout time-evolution. A total of $18\times(l+1)$ identity gates have to be added, also not changing the final complexity of $\mathcal{O}(l\chi^3 d^3)$.

Numerical Drawbacks

Unfortunately, none of the numerical tricks discussed in section 2.1.4 can be implemented in the infinite case.

The adaptive χ-method could actually be used also in the iTEBD algorithm, however it is only of little use there. The computational saving due to lower entanglement in bipartite splittings close to the boundary is absent, and the savings for the first few time-steps in an imaginary time evolution due to the initial product state also turn out to not justify this optimisation.

Furthermore, the storage of λ-values within the Γ-arrays to avoid division of small numbers is not applicable in the iTEBD algorithm. If, for example, one applies a gate $\hat{U}_{AB}$ that acts on representation "AB" (2.71) without exhibiting the according division by λ^B, the resulting situation is the following,

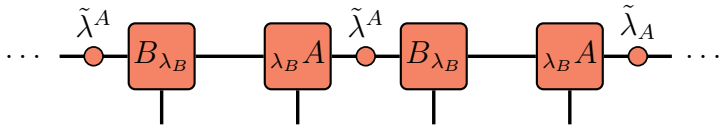

. (2.84)

If one would now try perform a gate on the "BA" representation (2.71), in the construction of the matrix Θ in step (2.35), $(\lambda^B)^2$ instead of λ^B would be inserted. Therefore in any case, at least one division by λ-values has to take place. The same holds for an l-site iMPS. Hence, in the iTEBD algorithm we use a small threshold value below which numbers are defined to be zero as described in section 2.1.4 to avoid numerical inaccuracies.

Application to the Bose-Hubbard Model

We are going to extensively use the iTEBD algorithm presented in this section to simulate transport properties of a system of bosons loaded into an optical lattice potential in chapter 3.

Bibliography

[1] U. Schollwöck. *Rev. Mod. Phys.* **77**, 259 (2005).

[2] S. R. White. *Phys. Rev. Lett.* **69**, 2863 (1992).

[3] S. R. White. *Phys. Rev. B* **48**, 10345 (1993).

[4] S. Östlund and S. Rommer. *Phys. Rev. Lett.* **75**, 3537 (1995).

[5] S. Rommer and S. Östlund. *Phys. Rev. B* **55**, 2164 (1997).

[6] F. Verstraete and J. I. Cirac. *Phys. Rev. B* **73**, 094423 (2006).

[7] M. A. Cazalilla and J. B. Marston. *Phys. Rev. Lett.* **88**, 256403 (2002).

[8] Guifré Vidal. *Phys. Rev. Lett.* **91**, 147902 (2003).

[9] G. Vidal. *Phys. Rev. Lett.* **93**, 040502 (2004).

[10] G. Vidal. *Phys. Rev. Lett.* **98**, 070201 (2007).

[11] A. J. Daley, C. Kollath, U. Schollwöck, and G. Vidal. *J. Stat. Mech.* **2004**, P04005 (2004).

[12] S. R. White and Adrian E. Feiguin. *Phys. Rev. Lett.* **93**, 076401 (2004).

[13] F. Verstraete, J. J. García-Ripoll, and J. I. Cirac. *Phys. Rev. Lett.* **93**, 207204 (2004).

[14] M. Zwolak and G. Vidal. *Phys. Rev. Lett.* **93**, 207205 (2004).

[15] F. Verstraete and J. I. Cirac. *arXiv: cond-mat/0407066* (2004).

[16] F. Verstraete, V. Murg, and J. I. Cirac. *Adv. Phys.* **57**, 143 (2008).

[17] S. R. Clark and D. Jaksch. *Phys. Rev. A* **70**, 043612 (2004).

[18] C. Kollath, Schollwock U., and Zwerger W. *Phys. Rev. Lett.* **95**, 176401 (2005).

[19] A. Kleine, C. Kollath, I. P. McCulloch, T. Giamarchi, and U. Schollwöck. *Phys. Rev. A* **77**, 013607 (2008).

[20] D. Gobert, C. Kollath, U. Schollwöck, and G. Schutz. *Phys. Rev. E)* **71**, 036102 (2005).

[21] A. J. Daley, S. R. Clark, D. Jaksch, and P. Zoller. *Phys. Rev. A* **72**, 043618 (2005).

[22] A. J. Daley, P. Zoller, and B. Trauzettel. *Phys. Rev. Lett.* **100**, 110404 (2008).

[23] M. A. Nielsen and I. L. Chuang. *Quantum Computation and Quantum Information*. Cambridge University Press, (2000).

[24] G. Vidal, J. I. Latorre, E. Rico, and A. Kitaev. *Phys. Rev. Lett.* **90**, 227902 (2003).

[25] T. J. Osborne and M. A. Nielsen. *Phys. Rev. A* **66**, 032110 (2002).

[26] T. D. Kühner, S. R. White, and H. Monien. *Phys. Rev. B* **61**, 12474 (2000).

[27] C. Kollath, U. Schollwöck, J. von Delft, and W. Zwerger. *Phys. Rev. A* **69**, 031601 (2004).

[28] M. Suzuki. *J. Math. Phys.* **32**, 2 (1991).

[29] A. T. Sornborger and E. D. Stewart. *Phys. Rev. A* **60**, 1956 (1999).

[30] Y.-Y. Shi, L.-M. Duan, and G. Vidal. *Phys. Rev. A* **74**, 022320 (2006).

[31] R. Orus and G. Vidal. *arXiv:0711.3960* (2007).

Chapter 3

Superfluid Boson Currents in 1D Lattices

In recent years, cold bosons in an optical lattice potential have developed into an excellent system for studying coherent many-body quantum effects in one, two or three dimensions. Seminal experiments have demonstrated the existence of Mott insulating (MI) and superfluid (SF) quantum phases [1], arising in the Bose-Hubbard model [2] and therefore indicating the validity of this model in the optical-lattice realisation [3].

Recently, also non-equilibrium dynamics within the Bose-Hubbard model have become a rising field of interest, especially the fate of a finite current, induced to bosons initially in an equilibrium SF ground state. A dynamical instability of this current was discovered experimentally [4] and its dependence on current magnitude and interaction strength has been extensively theoretically studied by E. Altman, A. Polkovnikov et al. [5], [6]. On the mean-field level, a stability phase diagram could be computed, interpolating between a classical instability in the limit of vanishing interactions (Gross-Pitaevskii regime) and the static SF-MI transition for strong interactions. Excellent agreement to this instability phase-diagram has been demonstrated in recent experiments [7] for a 3D system. However, the same experiment showed large deviations in the 1D case. In lower dimensions, quantum fluctuations are causing this breakdown of the mean-field ansatz. They can be analytically included in the limit of weak interactions and in the vicinity of the SF-MI transition [6]. However, they turn out to be very challenging for the case of an arbitrary interaction strength.

With the iTEBD algorithm (Section 2.2) at hand we have the possibility to fill this gap of intermediate interaction strength, simulating full time-evolution of currents under the full Bose-Hubbard Hamiltonian, in order to make quantitative predictions as to what should be measured in an experi-

ment.

In this chapter, firstly we will give a short theoretical overview of the infinite 1D Bose-Hubbard model, which we are utilising in our numerical calculations and will outline the dynamical instability theory, developed in [6] (Section 3.1). We then present a way to study boson currents with the iTEBD algorithm by making use of ground state calculations via imaginary time-evolution and real time simulations (Section 3.2). Finally we will show our results and build a stability crossover diagram for boson currents in an infinite 1D lattice from them (Section 3.3).

3.1 Theoretical Overview

We will first introduce the Bose-Hubbard model, which turns out to be an excellent model for treating cold bosons in an optical lattice potential [3] under certain conditions. We will mention the main static ground state features, i.e. the existence of the Superfluid (SF) and the Mott Insulating (MI) $T = 0$ quantum phases [2]. Afterwards we introduce the boson current operator, and develop a method to theoretically impose any desired mean quasi momentum to the atoms in a lattice. We conclude with an overview of the analytical results obtained for the onset of instability of the boson current, developed by E. Altman, A. Polkovnikov et al. [5, 6].

3.1.1 Bose-Hubbard Model

It was shown by D. Jaksch et al. [3] that under certain circumstances, the Bose-Hubbard model accurately describes a system of cold bosons loaded into an optical lattice potential. Without trapping potential, the Bose-Hubbard Hamiltonian takes the form ($\hbar \equiv 1$)

$$\hat{H} = -J \sum_{\langle ij \rangle} \hat{b}_i^\dagger \hat{b}_j + \frac{U}{2} \sum_i \hat{n}_i(\hat{n}_i - 1). \tag{3.1}$$

In the first term, $\hat{b}_i$ ($\hat{b}_i^\dagger$) are the bosonic annihilation (creation) operators at lattice site i, obeying the bosonic commutation relations $[\hat{b}_i, \hat{b}_j] = [\hat{b}_i^\dagger, \hat{b}_j^\dagger] = 0$ and $[b_i, b_j^\dagger] = \delta_{i,j}$. J is the hopping amplitude between neighbouring sites, whose combinations of indices are denoted by $\langle ij \rangle$. The second term provides a repulsive on-site interaction U, where $\hat{n}_i \equiv \hat{b}_i^\dagger \hat{b}_i$ is the particle number operator at site i. The filling factor of N particles on M lattice sites shall be denoted $\bar{n} \equiv N/M$. A sketch of the terms in (3.1) is given in figure 3.1. The Bose-Hubbard model is valid in the regime where excitations to the

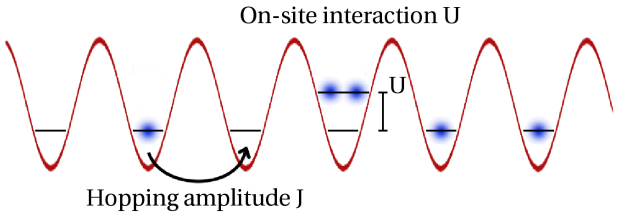

Figure 3.1: Sketch of the terms occurring in the Bose-Hubbard Hamiltonian.

second Bloch band can be neglected, which requires that temperature and interaction energy are sufficiently small compared to the trapping frequency of the optical lattice (see below). Furthermore, only tunnelling between next-neighbour sites is taken into account and interactions between particles not located on the same site are neglected.

Derivation of the Bose-Hubbard Hamiltonian

We are going to sketch the derivation of the Bose-Hubbard Hamiltonian (3.1) as it was first introduced in [3].

The spatially varying ac-Stark shift from a standing wave of laser light far detuned from an internal transition of an atom gives rise to a potential of the form $V_L \equiv V_0 \sin^2(k_l x)$ (in 1D), with wavenumber $k_l \equiv 2\pi/\lambda \equiv 2\pi/2a$ and lattice constant a. With this external potential in each dimension, we start from the microscopic model, the second quantised Hamiltonian

$$\hat{H} = \int d^3x\, \hat{\Psi}^\dagger(\vec{x}) \left(-\frac{\hbar^2}{2m}\nabla^2 + V_L(\vec{x}) \right) \hat{\Psi}(\vec{x}) + \frac{1}{2}\frac{4\pi a_s \hbar^2}{m} \int d^3x\, \hat{\Psi}^\dagger(\vec{x})\hat{\Psi}^\dagger(\vec{x})\hat{\Psi}(\vec{x})\hat{\Psi}(\vec{x}) \tag{3.2}$$

with the bosonic field operator $\hat{\Psi}(\vec{x})$. The first term consists of the kinetic energy and the lattice potential, the second term gives rise to the interaction of the particles which is approximated by a pseudopotential with sufficiently short s-wave scattering length a_s (in the Born approximation).

The Bose-Hubbard Hamiltonian arises if the field operators are expanded into maximally localised Wannier functions $w_n(\vec{x} - \vec{x}_i)$ with band index n,

$$\hat{\Psi}(\vec{x}) \equiv \sum_{i,n} \hat{b}_{i,n} w_n(\vec{x} - \vec{x}_i). \tag{3.3}$$

Under the assumption that interaction energies and temperatures are much smaller than the trapping frequency ω_T, which is of the order of the separation of the lowest two Bloch bands as defined in the harmonic deep-lattice

approximation via $(k_l x)^2 V_0 \equiv m\omega_T^2 x^2/2$, it is a very good approximation to only consider the lowest band ($n = 1$). Then, the Bose-Hubbard parameters U and J in equation (3.1) can be computed by inserting (3.3) into (3.2) and identifying

$$J = -\int dx\, w_0(x) \left(-\frac{\hbar^2}{2m}\frac{d^2}{dx^2} + V_L(x) \right) w_0(x-a), \tag{3.4}$$

$$U = \frac{4\pi a_s \hbar^2}{m} \int d^3x\, |w_0(\vec{x})|^4. \tag{3.5}$$

Thereby, the two approximations have been made that tunnelling parameters calculated over more than two neighbouring sites and all interaction energies other than the on-site term U were neglected. All three approximations in this derivation of the Bose-Hubbard model turn out to be valid if the lattice depth V_0, which can be controlled by the laser intensity, is sufficiently large. That means $V_0 \gtrsim 2E_R$ with the recoil energy $E_R \equiv \hbar^2 k_l^2/2m$ of the corresponding atoms [8].

By using very strong laser intensities in one (two) dimensions, hopping in certain directions can be suppressed and the Bose-Hubbard model can be effectively also implemented as two (one) dimensional system.

Quantum Phases

For integer $\bar{n}$, ground states of the Bose-Hubbard Hamiltonian (3.1) exist in two different quantum phases depending on the ratio of the on-site interaction to the tunnelling parameter $u \equiv U/J$. This was first investigated by M. P. A. Fisher et al. in reference [2].

In one dimension with $\bar{n} = 1$ for $u \lesssim 3.37$ [9], the system is in a superfluid phase, which is a quasi-condensate with a single particle density matrix (SPDM) $\langle \hat{b}_i^\dagger \hat{b}_j \rangle$ exhibiting quasi off-diagonal long-range order. In the limit $u \to 0$, the state of the system takes the form

$$|\Psi_{SF}\rangle = \frac{1}{\sqrt{N! M^N}} \left(\sum_j^M \hat{b}_j^\dagger \right)^N |0\rangle, \tag{3.6}$$

with $|0\rangle$ denoting the vacuum state with no particle in the lattice. In the limit $M \to \infty$ and $N \to \infty$ at fixed $\bar{n}$, (3.6) can be computed to tend to a locally coherent product state,

$$|\Psi_{SF}\rangle \propto \prod_j \left(e^{\sqrt{\bar{n}}\ \hat{b}_j^\dagger} |0\rangle_j \right). \tag{3.7}$$

On each site the ideal SF state (3.7) is characterised by Poisson number statistics. This can be seen by noting that on a particular site k the local state takes the normalised form

$$|\Psi_{SF}\rangle_k = e^{-\bar{n}/2} \sum_l \frac{\sqrt{\bar{n}}^{\,l}}{\sqrt{l!}} |l\rangle_k, \tag{3.8}$$

and therefore the probability for m particles at this site is

$$P_m = |\langle m|\Psi_{SF}\rangle|^2 = e^{-\bar{n}} \frac{\bar{n}^m}{m!}. \tag{3.9}$$

For $u \gtrsim 3.37$, the system is in a Mott insulating phase, a localised state with exponentially decaying off-diagonal $\langle \hat{b}_i^\dagger \hat{b}_j \rangle$ elements. In the ideal limit $u \to \infty$, the MI state becomes a Fock state with fixed number of particles $\bar{n}$ at each site,

$$|\Psi_{MI}\rangle = \prod_j^M |\bar{n}\rangle_j. \tag{3.10}$$

Note that the transition from a SF to an MI phase is only possible for exactly integer filling factors $\bar{n}$. Otherwise, even in the extreme MI limit $u \to \infty$ a fraction of bosons will remain delocalised on top of a frozen MI phase.

To show some examples, we do numerical ground state calculations using imaginary time evolution within the iTEBD algorithm (Section 2.2) for an homogeneous infinite 1D Bose-Hubbard model. We analyse the off-diagonal long-range behaviour, i.e. look at the off-diagonal elements of the SPDM $\langle \hat{b}_i^\dagger \hat{b}_j \rangle$, and the eigenvalues of this matrix.

In figure 3.2, off-diagonal long-range behaviour over 400 sites is shown in a system with filling factor $\bar{n} = 1$ for a SF phase at $u = 3.0 < u_c$ and a MI case at $u = 4.0 > u_c$. To show over which range our algorithm represents the real long-range behaviour, we plot results for increasing values of the Hilbert space truncation parameter $\chi = 50, 70, 100$. We find that our calculation with $\chi = 100$ represents long-range behaviour well over a range of approximately 100 sites. In the SF case we find an algebraic decay (linear on the double logarithmic scale) of the off-diagonal SPDM elements, indicating the quasi long-range order, whereas in the MI case these elements decay exponentially.

To further observe the quasi condensate properties of our two example phases, we compute the SPDM for a reduced portion of our system, typically 100 sites. A typical eigenvalue spectrum for this density matrix is shown in figure 3.3. Whilst the condensate fraction is zero for the full infinite system, we expect that the quasi-condensate will be recognisable as a strongly

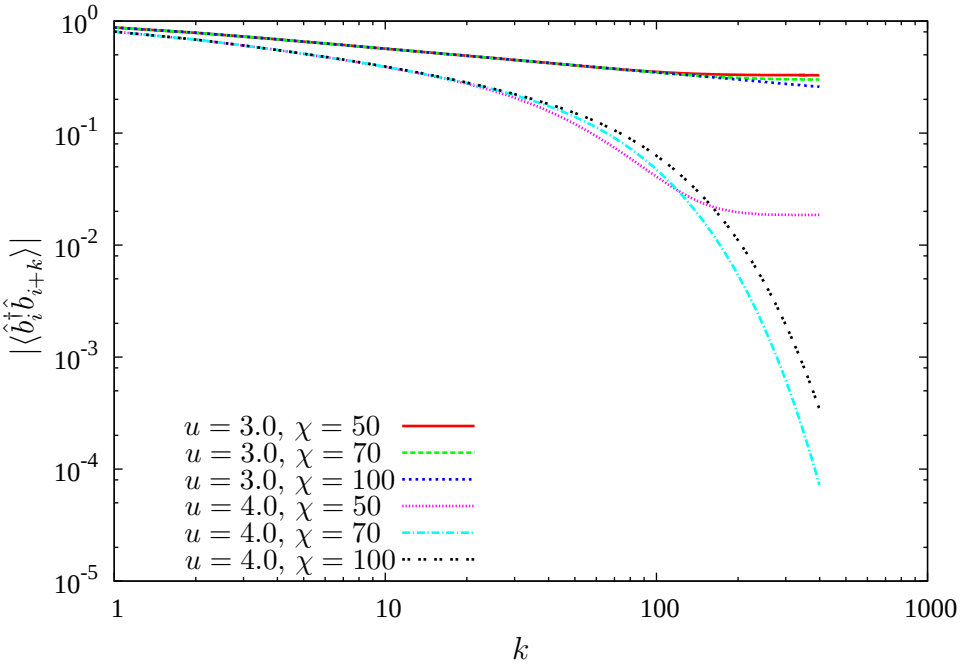

Figure 3.2: The off-diagonal elements of the SPDM $\langle \hat{b}_i^\dagger \hat{b}_j \rangle$ in the case of on-site interaction $u = 3.0$ (SF regime) and $u = 4.0$ (MI regime) in an infinite 1D Bose-Hubbard model with commensurate filling $\bar{n} = 1$. The results are obtained by imaginary time evolution within the iTEBD algorithm, for different values of the truncation parameter χ.

occupied mode in the SPDM in any finite part of the system. Numerically, we indeed find that in the SF regime there exists a large first eigenvalue λ_1, indicating a quasi condensate with most particles in one quantum state, namely the first eigenstate of the SPDM, whereas in the MI regime all SPDM eigenstates have similar occupation numbers. Note that from the eigenvalues of the SPDM, a quasi condensate fraction can be evaluated by building the ratio

$$\mathcal{C}_S \equiv \lambda_1 / \sum_m^S \lambda_m = \lambda_1 / N \tag{3.11}$$

over a certain range S. In general, we have found that an accurate evaluation of $\mathcal{C}_S$ over S sites requires larger values of χ as S is increased. For $S = 100$ we have found that $\chi = 100$ typically provides well converged results.

The location of the SF to MI transitions in the Bose-Hubbard model can be calculated analytically using a mean-field ansatz [2, 10]. In general, for the $\bar{n} = 1$ transition in arbitrary dimensions it can be located at $u_c^{MF} \approx 5.8z$,

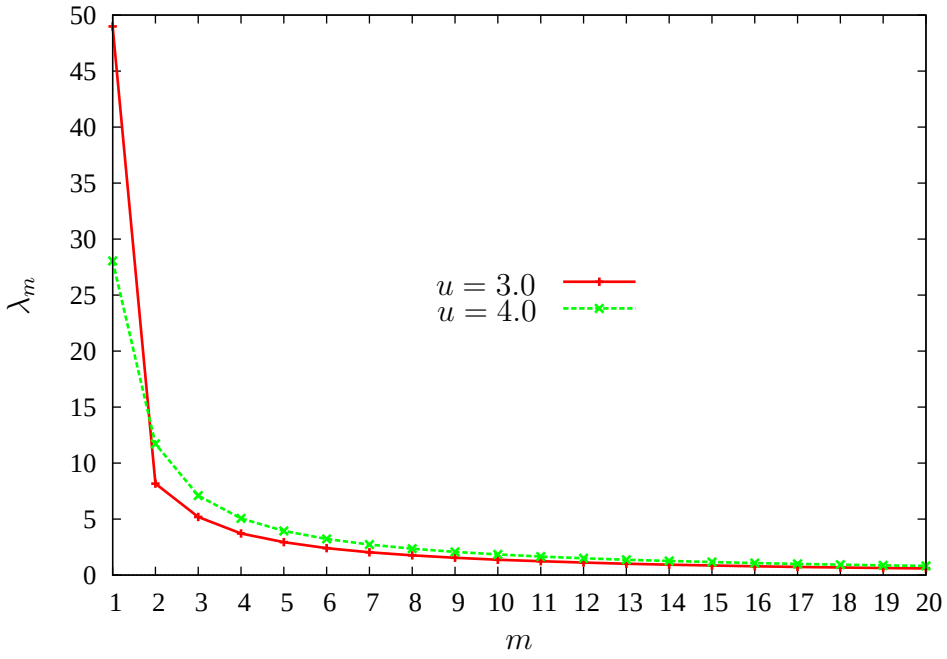

Figure 3.3: The eigenvalue spectrum of the SPDM $\langle \hat{b}_i^\dagger \hat{b}_j \rangle$ resulting from a diagonalisation over a region of 100 sites from the infinite system for a SF state ($u = 3.0$) and a MI state ($u = 4.0$) in an infinite 1D Bose-Hubbard model with commensurate filling $\bar{n} = 1$. For this plot $\chi = 100$ and no changes are visible if $\chi = 50, 70$.

where z is the coordination number i.e. the number of nearest neighbours. Whilst finding good agreement to experiments and numerical simulations in 3D and 2D, mean-field results have shown to be poor in 1D as can be seen by comparing the real transition point of $u_c \approx 3.37$ found in [9] to the mean-field prediction of $u_c^{MF} \approx 11.6$. This is because large quantum fluctuations invalidate the mean-field approach in the case of small z and therefore lower dimensions. From figure 3.2 also in our simulations we conclude that the critical on-site interaction is $3.0 \lesssim u_c \lesssim 4.0$, but we are not going to find the transition point more exactly here. This has been analysed in detail using variational DMRG methods in [9]. We will now go on to study dynamic transport properties within the 1D Bose-Hubbard model.

3.1.2 Boson Currents

A quantity of interest for the dynamics of the particles is the boson current $\hat{j}$ and its fate during time evolution. The evolution of the particle number

operator at a given site k, $\frac{d}{dt}\hat{n}_k$ can be evaluated in the Bose-Hubbard model, by inserting (3.1) into the Heisenberg equation of motion ($\hbar \equiv 1$),

$$\frac{d}{dt}\hat{n}_k = i[\hat{H}, \hat{n}_k] = \frac{J}{i}\sum_l \left[\hat{b}_l^\dagger \hat{b}_{l+1} + \hat{b}_{l+1}^\dagger \hat{b}_l\,,\ \hat{b}_k^\dagger \hat{b}_k\right]. \tag{3.12}$$

Exploiting the bosonic commutation relations, (3.12) immediately reduces to

$$\frac{d}{dt}\hat{n}_k = \frac{J}{i}\left(\hat{b}_{k+1}^\dagger \hat{b}_k - \hat{b}_k^\dagger \hat{b}_{k+1} - \hat{b}_k^\dagger \hat{b}_{k-1} + \hat{b}_{k-1}^\dagger \hat{b}_k\right). \tag{3.13}$$

Analogous to the continuous case, where in the continuity equation the spatial derivative of the current density equals the time derivative of the particle density, we define the boson current by

$$\hat{j}_k - \hat{j}_{k-1} \equiv \frac{d}{dt}\hat{n}_k \tag{3.14}$$

and identify from (3.13)

$$\hat{j}_k = \frac{J}{i}\left(\hat{b}_{k+1}^\dagger \hat{b}_k - \hat{b}_k^\dagger \hat{b}_{k+1}\right). \tag{3.15}$$

Note that the average of the current expectation values $\frac{1}{M}\sum_m^M \langle \hat{j}_m \rangle$ is proportional to the average group velocity calculated via the quasi momentum of the particles. This can be seen by introducing the discrete Fourier transform of the annihilation and creation operators $\hat{b}_m \equiv \frac{1}{\sqrt{M}}\sum_q^M e^{-iq\frac{2\pi}{M}m}\,\hat{a}_q$ (periodic boundary conditions) and calculating

$$\begin{aligned}
\frac{1}{M}\sum_m^M \langle \hat{j}_m \rangle &= \frac{J}{iM}\sum_m^M \langle \hat{b}_{m+1}^\dagger \hat{b}_m \rangle + \text{H.c.} \\
&= \frac{J}{iM^2}\sum_m^M \sum_{q_1,q_2}^M e^{i(q_1-q_2)\frac{2\pi}{M}m} e^{i\frac{2\pi}{M}q_1} \langle \hat{a}_{q_1}^\dagger \hat{a}_{q_2} \rangle + \text{H.c.} \\
&= \frac{1}{M}\sum_q^M 2J \sin\left(\frac{2\pi}{M}q\right) \langle \hat{a}_q^\dagger \hat{a}_q \rangle \\
&\equiv \frac{1}{M}\sum_q^M 2J \sin\left(k_q a\right) n_{k_q a},
\end{aligned} \tag{3.16}$$

where in the last step, the lattice momentum $k_q \equiv q\ 2\pi/L$ (with system length L), the lattice constant $a \equiv L/M$ and the quasi momentum distribution function (MDF) $n_{k_q a} \equiv \langle \hat{a}_q^\dagger \hat{a}_q \rangle$ have been defined. Here, $2aJ\sin(ka)$

represents the group velocity corresponding to a particle with lattice momentum k, as defined by $v_k \equiv dE(k)/dk$ from the lowest Bloch band dispersion relation $E(k) = -2J\cos(ka)$.

The MDF can be evaluated directly from the SPDM via

$$n_p \equiv \frac{1}{M}\sum_{n,m} e^{-ip(n-m)}\langle \hat{b}_n^\dagger \hat{b}_m\rangle, \tag{3.17}$$

which is obtained by simply inserting the Fourier decompositions of $\hat{a}_q^\dagger$ and $\hat{a}_q$ in (3.16) and defining $p \equiv k_q a$, which is the quasi momentum measured in units of the inverse lattice constant.

The Kick Operator

Bosons, moving at a mean quasi momentum (per lattice unit) ka can be created by applying the operator

$$\hat{K}(ka) \equiv \prod_l e^{i(ka)l\hat{n}_l} \tag{3.18}$$

to a ground state vector of the system. To see this, it is useful to introduce the relations

$$\hat{K}\hat{b}_{j_i}^\dagger = \hat{b}_{j_i}^\dagger \hat{K} e^{ikaj_i} \tag{3.19}$$

$$\hat{K}^\dagger \hat{b}_{j_i}^\dagger = \hat{b}_{j_i}^\dagger \hat{K}^\dagger e^{-ikaj_i}. \tag{3.20}$$

These immediately follow from the Baker-Hausdorff identity

$$e^A\ B\ e^{-A} = B + \sum_{m=1}\frac{1}{m!}[A,B]_m \tag{3.21}$$

with $[A,B]_1 \equiv [A,B]$ and $[A,B]_m \equiv [A,[A,B]_{m-1}]\ \ \forall m \in \mathbb{N} > 1$ and the commutator

$$[\pm ika\sum_l l\hat{n}_l, \hat{b}_{j_i}^\dagger]_m = (\pm ikaj_i)^m\ \hat{b}_{j_i}^\dagger \quad \forall m \in \mathbb{N}. \tag{3.22}$$

Equations (3.19) and (3.20) allow to directly calculate the effect of the operator $\hat{K}(ka)$ on the MDF n_p of an arbitrary initial state:

$$\frac{1}{M}\sum_{n,m} e^{-ip(n-m)}\langle \hat{K}^\dagger \hat{b}_n^\dagger \hat{b}_m \hat{K}\rangle = \frac{1}{M}\sum_{n,m} e^{-i(p+ka)(n-m)}\langle \hat{b}_n^\dagger \hat{b}_m\rangle. \tag{3.23}$$

Thus, $\hat{K}(ka)$ translates the MDF by an amount of ka, conserving its initial shape. Therefore, if the initial state is a ground state with n_p distributed around $p = 0$, the bosons are moving at an average quasi momentum of ka after applying $\hat{K}(ka)$.

If the initial state is an ideal superfluid ground state (3.6) ($u \to 0$), the operator $\hat{K}$ places all condensate atoms in the same ka-quasi momentum state, characterised by a uniform phase difference of ka between neighbouring sites. This follows from iteratively using (3.19),

$$\begin{aligned}\hat{K}\left(\sum_j \hat{b}_j^\dagger\right)^N |0\rangle &= \sum_{j_1,j_2,\ldots,j_N} e^{ikaj_1}e^{ikaj_2}\ldots e^{ikaj_N}\ \hat{b}_{j_1}^\dagger \hat{b}_{j_2}^\dagger \ldots \hat{b}_{j_N}^\dagger\ |0\rangle \\ &= \left(\sum_j e^{ikaj}\hat{b}_j^\dagger\right)^N |0\rangle. \end{aligned} \tag{3.24}$$

Furthermore, in the ideal superfluid case it is possible to calculate the boson current expectation value immediately after applying $\hat{K}(ka)$. Therefore, it is useful to note that

$$\hat{b}_n\left(\sum_j e^{ikaj}\hat{b}_j^\dagger\right)^N |0\rangle = e^{ikan}\sum_{l=1}^{N}\left(\sum_j e^{ikaj}\hat{b}_j^\dagger\right)^{N-1} |0\rangle, \tag{3.25}$$

which simply follows from applying the bosonic commutation relation N times. If one now assumes that all particles are in the normalised state $|\Psi_{SF}\rangle = 1/\sqrt{N!M^N}\left(\sum_j e^{ikaj}\hat{b}_j^\dagger\right)^N |0\rangle$, relation (3.25) leads to

$$\begin{aligned}\langle\Psi_{SF}|\hat{K}^\dagger\hat{j}_n\hat{K}|\Psi_{SF}\rangle &= \frac{N}{iM}\left(e^{ika(n+1)}e^{-ikan} - e^{-ika(n+1)}e^{ikan}\right) \\ &= 2\bar{n}\sin(ka) \end{aligned} \tag{3.26}$$

This is consistent to equation (3.16) with

$$n_p = N\delta_{p,ka}. \tag{3.27}$$

In the case of non-zero interaction energy U, the number of particles in the state $\propto \sum_j e^{ikaj}\ \hat{b}_j^\dagger\ |0\rangle$ will decrease, leading to a finite width in the MDF. Thus, in the case of $ka < \pi$ (the sine function is concave), due to the symmetry of the ground state MDF, the quasi-momentum average and therefore the initial current will decrease.

In the opposite limit of infinite interaction strength, the ideal MI state (3.10) does not support any current, which can be immediately seen by writing

$$\hat{b}_m \hat{K}|\Psi_{MI}\rangle = \hat{b}_m \prod_j^M e^{ikaj\bar{n}}|\bar{n}\rangle_j \propto |\bar{n}-1\rangle_m \prod_{j\neq m}^M |\bar{n}\rangle_j \tag{3.28}$$

and noting that therefore

$$\langle\Psi_{MI}|\hat{K}^\dagger \hat{j}_n \hat{K}|\Psi_{MI}\rangle = \frac{J}{i}\langle\Psi_{MI}|\hat{K}^\dagger \hat{b}_{n+1}^\dagger \hat{b}_n \hat{K}|\Psi_{MI}\rangle + \text{H.c.} = 0. \tag{3.29}$$

Having introduced the MDF and the kick operator, we will give some examples for the action of the kick operator applied to an infinite SF and MI matrix product ground state within our iTEBD algorithm.

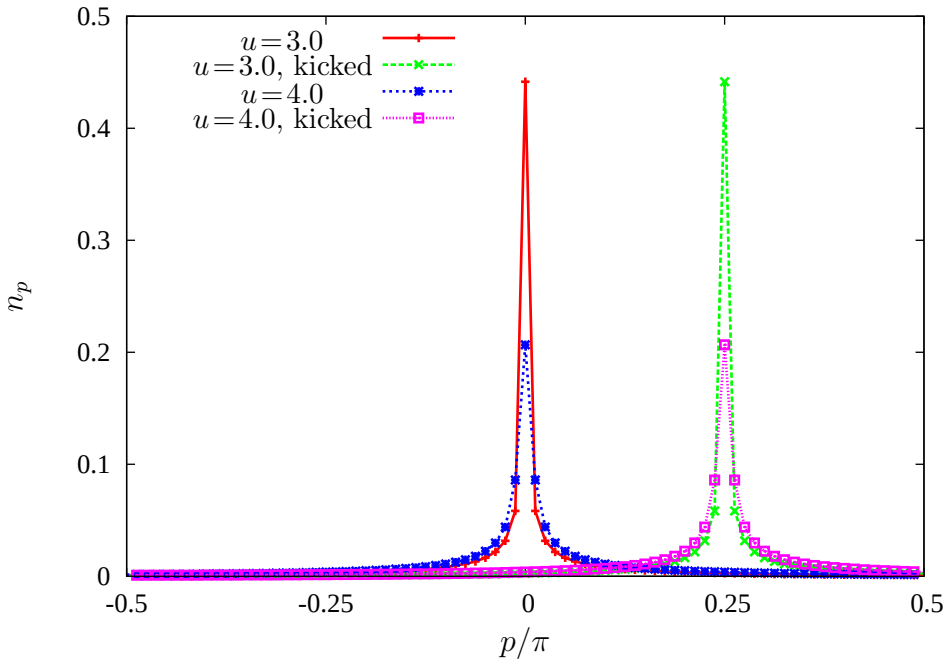

Figure 3.4: The normalised momentum distribution functions for a SF ($u = 3.0$) and a MI ground states ($u = 4.0$) before and after applying a kick operator (3.18), $\hat{K}(ka = 0.25\pi)$, which translates the MDF by a quasi momentum of $ka = \pi/4$. For this plot, 160 SPDM samples were used and $\chi = 100$. No changes are visible compared to $\chi = 50, 70$ results.

In figure 3.4, we show the quasi momentum distributions (normalised to one) of the SF ground state with $u = 3.0$ and the MI ground state with

$u = 4.0$. The results are obtained from an imaginary time evolution within the iTEBD algorithm with a truncation parameter of $\chi = 100$ and a SPDM evaluation range of 160 sites. As in the eigenvalue spectrum of the SPDM in figure 3.3, also here we can distinguish between the two quantum phases. Sharp distributed peaks around $p = 0$ arise in the SF phase whereas a broader MDF indicates a MI phase. In the ideal SF limit, the peak would become a Kronecker delta, (3.27). As shown in equation (3.23), the application of the kick operator (3.18) $\hat{K}(ka = \pi/4)$ with kick strength $ka = \pi/4$ leads to a translation of the whole MDF by an amount of $\pi/4$ in quasi-momentum space.

3.1.3 Current Instabilities

Having created a finite current from a ground state of the Bose-Hubbard model via (3.18), it is an interesting question if this current remains constant in time (i.e. is really superfluid) or if it vanishes, and to which extent this depends on the on-site interaction u and the kick strength ka. This can be directly related to an experimental situation (like in [7]), where the application of the Kick operator corresponds to an accelerated lattice, which can for example be induced by slightly detuning the lattice laser beams. Analytical solutions for this problem have been computed in several limits by E. Altman, A. Polkovnikov et al. [5, 6].

In the limit of weak interactions $\bar{n}J \gg U$ with many particles occupying one state, the system can be approximately described in a mean-field sense by classical fields $\Psi_i(\Psi_i^*)$ corresponding to $\langle b_i \rangle$ ($\langle b_i^\dagger \rangle$). The evolution of the fields is governed by the discrete time-dependent Gross-Pitaevskii equation, which for the one dimensional system takes the form

$$i\frac{d\Psi_i}{dt} = -J\left(\Psi_{i-1} + \Psi_{i+1}\right) + U|\Psi_i|^2\Psi_i. \tag{3.30}$$

In this weakly interacting Gross-Pitaevskii regime, solutions to equation (3.30) are provided by current carrying plane waves $\Psi_l = \Psi_0 e^{i(kal-\omega t)}$ with $\omega = -2J\cos(ka) + U|\Psi_0|^2$. The stability of these states can be evaluated in a simple linear stability analysis [11, 12]. It turns out, that for $\cos(ka) < 0$, and therefore $\pi/2 < ka < 3\pi/2$ eigenfrequencies of perturbations become imaginary, rendering the state unstable due to the exponential growth of this perturbations in time.

A physical picture of this instability is given in [6]: In the limit of weak interactions, a condensate is moving in the lowest Bloch band with a quasi momentum independent superfluid density. For small linear perturbations in

the uniform phase gradient ka, the resulting energy reads

$$\begin{aligned} E'(ka) &= \frac{1}{2}E(ka+\delta(ka)) + \frac{1}{2}E(ka-\delta(ka)) \\ &= E(ka) + \frac{d^2E(ka)}{d(ka)^2}(\delta(ka))^2 + \mathcal{O}((\delta ka)^4). \end{aligned} \tag{3.31}$$

Hence, the energy difference $\delta E \propto \frac{d^2E(ka)}{d(ka)^2}$ and it is a necessary condition for stability that $\frac{d^2E(ka)}{d(ka)^2} > 0$. Otherwise small perturbations would lead to a decrease in the energy. Therefore, in the lowest Bloch band with energy $E \propto -\cos(ka)$, $d^2E/d(ka)^2 \propto \cos(ka)$ and this stability condition is violated if the quasi momentum ka is larger than the critical value of $\pi/2$.

In the regime of strong interactions, stability is obviously limited by the static SF–MI transition, since the MI state does not support any superfluid current. Thus, for integer filling and $ka \approx 0$, superfluid current becomes unstable if the interaction $u \equiv U/J$ reaches the critical value u_c of the transition. In the non-commensurate case, superfluidity is still possible beyond u_c, since parts of the system will always remain in the SF phase. However, in this thesis we will only consider the case of $\bar{n} = 1$.

It is an interesting question, how the current stability for commensurate filling interpolates in the region of intermediate interaction strength u and arbitrary phase gradient ka as sketched in figure 3.5.

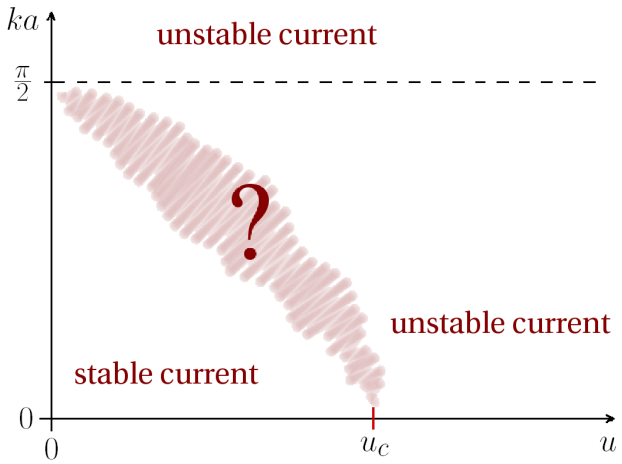

Figure 3.5: How does the current stability interpolate between the classical instability of $ka = \pi/2$ and the SF to MI transition point for an infinite homogeneous 1D Bose-Hubbard model?

In general, the question has to be addressed numerically. Stability crossover diagrams have been calculated in [6] using the Gutzwiller ansatz, assuming

factorisable (non-entangled) wavefunctions throughout the time-evolution. This is equivalent to the mean-field approximation. Quantum fluctuations of the condensate are completely neglected. Therefore, this method leads to a sharp boundary causing a current decay when crossing a critical value of ka and u. However, in contrast to higher dimensions, in a one dimensional system quantum fluctuations play a crucial role. Quantum tunnelling out of the condensate is causing a decay of the state before the mean-field transition and therefore broadening it. Rates for phase slips due to quantum tunnelling as well as thermal activation have been calculated in [6] in the limit of weak and strong interactions, quantifying this broadening. So far, for arbitrary values of ka and u, no analytical calculations or exact numerical simulations were possible. Exact numerical simulations are limited to very small systems and can therefore only be used for very few values of ka and are further suffering from boundary effects. By employing the iTEBD algorithm (Section 2.2) for this problem, we are using a new approach of numerical simulations for infinite systems. Thereby we are fully taking into account quantum fluctuations in the sense that a large enough amount of entanglement is considered throughout the time-evolution.

3.2 iTEBD Calculations

In this section, we discuss how to use the iTEBD algorithm to observe boson currents in a homogeneous infinite 1D Bose-Hubbard model. We will explain the numerical procedure and comment on the main numerical obstacles.

3.2.1 Numerical Procedure

To arrive at our goal, calculating a stability crossover diagram as indicated in figure 3.5, we proceed in 3 major steps:

1. We prepare the ground state $|\Psi_G\rangle$ for given parameters U, J and $\bar{n}$ using imaginary time evolution for an infinite two-site MPS representation within the iTEBD algorithm. We investigate values of $0.5 \leq u \leq 4.0$ over the range from the SF ground state at $u = 0.5$ to the MI regime ($u_c \approx 3.37$) with steps of $\Delta u = 0.5$. All simulations are performed for the commensurate $\bar{n} = 1$ filling case. To obtain a ground state with a certain filling factor $\bar{n}$, we add a chemical potential term $-\mu \sum_i \hat{n}_i$ to the Bose-Hubbard Hamiltonian (3.1) and dynamically change μ to adjust $\bar{n}$ during imaginary time evolution. Convergence is tested by observing asymptotic off-diagonal long-range behaviour of the SPDM (see figure 3.2). The quality of the stationary ground state $|\Psi_G\rangle$ is

further tested by switching to real time evolution and verifying a SPDM staying constant in time.

2. For a desired quasi momentum shift in inverse lattice units ka we apply the operator $\hat{K}(ka)$ to $|\Psi_G\rangle$. Therefore, to take into account the translational invariance of the kick operator, we extend the two-site iMPS representation to l sites, depending of the value of ka. We are using steps $\Delta ka = 0.05\pi$ for a range from very small kicks to the classical instability limit, i.e. $0.05 \leq ka \leq 0.50$. Thus, for example in the worst case of $ka = 0.05\pi$ we have to use a $l = 40$ sites iMPS representation to account for the 40 site periodicity of $\hat{K}(\pi/20)$. The application of $\hat{K}$ is then computed, by simply contracting the on-site operator $\hat{O}_K^{[m]}(ka) \equiv e^{i(ka)m\hat{n}_m}$ as indicated in (2.23) to each site m of the iMPS.

3. We simulate the real time evolution of the kicked ground state, $|\Psi(t)\rangle = e^{-i\hat{H}t}\hat{K}(ka)|\Psi_G\rangle$, using the same values of U and J as in the ground state calculations. We evaluate the expectation value of the current operator $\langle\hat{j}_k\rangle = \frac{J}{i}\langle\hat{b}_{k+1}^\dagger\hat{b}_k - \hat{b}_k^\dagger\hat{b}_{k+1}\rangle$ as a function of time as well as the SPDM $\langle\hat{b}_i^\dagger\hat{b}_j\rangle$ and the MDF $n_p \equiv \frac{1}{M}\sum_{n,m} e^{-ip(n-m)}\langle\hat{b}_n^\dagger\hat{b}_m\rangle$. We compute condensate fractions $\mathcal{C}_S$ over a region of S sites by diagonalising the SPDM up to a maximum off-diagonal distance S and relating the eigenvalues via $\lambda_1/\sum_m^S \lambda_m$.

Quality Checks

To obtain valid results from the iTEBD algorithm, three main approximations have to be met and convergence tests for different quantities have to be performed.

1. The main approximation of the iTEBD algorithm is to use an adaptive truncated MPS representation utilising only a computationally tractable small number of slightly entangled basis states. To ensure that sufficiently many of these states are taken into account, we compare results for truncation parameters $\chi = 50, 70, 100$ and find good convergence within these values. Additionally, we keep track of the largest truncation error ϵ_j (2.20) occurring in each time step.

   As an example for the ground state calculations, figure 3.2 in section 3.1 shows the χ-convergence in the off-diagonal elements of the SPDM with increasing χ. Figure 3.6 shows example results for real time simulations of the boson current and the quasi condensate fraction (evaluated over

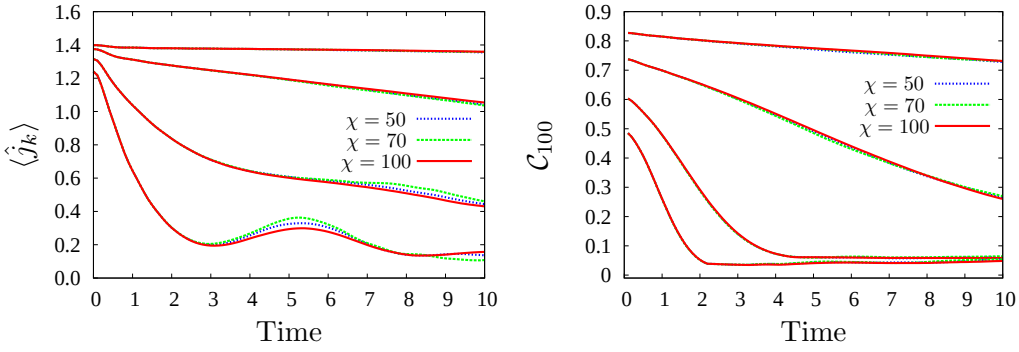

Figure 3.6: Results for boson currents and condensate fractions $\mathcal{C}_{100}$ as a function of time after applying a momentum kick of $ka = \pi/4$. Plotted are results for $u = 0.5$, $u = 1.0$, $u = 2.0$ and $u = 3.0$ (in this order from the top to the bottom). For each value of u, three χ-values $\chi = 50, 70, 100$ are utilised. We find convergence for increasingly large χ. Total differences are reasonably small (up to 1% for $u = 0.5, 1.0$) on a timescale $0 \leq t \leq 10$ ($J \equiv \hbar \equiv 1$), except if the current drops to zero quickly (differences up to 10% for $u = 2.0, 3.0$).

100 sites). Truncation errors $\max_j(\epsilon_j)$ for two of these examples are plotted in figure 3.7.

We find convergence for increasingly large values of χ with differences of a maximum of approximately 1% between the results of $\chi = 70$ and $\chi = 100$ for $u = 0.5$ and $u = 1.0$ at time 10. In cases of larger u, where the boson current drops to zero rapidly we observe larger differences up to about 10%. In this regions we observe current oscillations and small condensate fractions that are slowly increasing for large times. Despite the fact that in this case the quantitative values between the results of different χ-values are quite large, qualitatively we still find the same behaviour of an oscillating decreasing current and a monotonically decreasing condensate fraction.

In figure 3.7 we find that the largest truncation error of each time-step continuously increases during time evolution. This indicates a general increase of the entanglement in the system with time. Comparing figure 3.7 with figure 3.6 leads to the conclusion that roughly at a truncation error of 10^{-5}, errors become visible on the scales on which we observe the boson currents and the quasi condensate fractions.

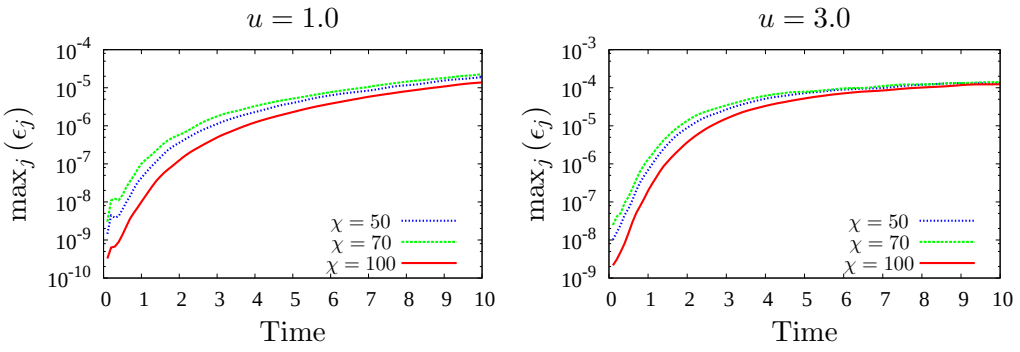

Figure 3.7: The largest truncation error ϵ_j (Equation (2.20)) in each time-step for the real time simulations with $u = 1.0$ and $u = 3.0$ from figure 3.6.

2. Dealing with an infinite Bose-Hubbard-model, in principle the dimension of the local Hilbert space at a particular site (i.e. the maximum possible occupation number) is infinite and therefore cannot be treated numerically. Nevertheless, it is clear that for a filling factor of $\bar{n} = 1$, the probability for high occupations at a single site becomes very small. For example, in case of an ideal MI product ground state, a local dimension of $d = 1$ would suffice and for an ideal SF locally coherent state with Poisson number statistics (3.7) we expect the probability of k particles at a particular site to decay like $\frac{1}{k!}$ (see equation (3.9)). Therefore, it is a very good approximation to truncate the local Hilbert space at some small upper dimension. In our simulations we compare local dimensions of 6 and 8, without observing any noticeable effect. We furthermore evaluate the probability for the maximum allowed single site occupation as a function of time and verify that this number is close to zero.

   In figure 3.8, we plot results of boson current simulations for $u = 1.0$ and $u = 3.0$ ground states kicked by $ka = 0.25\pi$ and compare the effect of increasing the local dimension from $d = 6$ to $d = 8$. Furthermore we show the local probabilities for the maximally allowed single site occupation p ($\langle \hat{n}_i \rangle = d$).

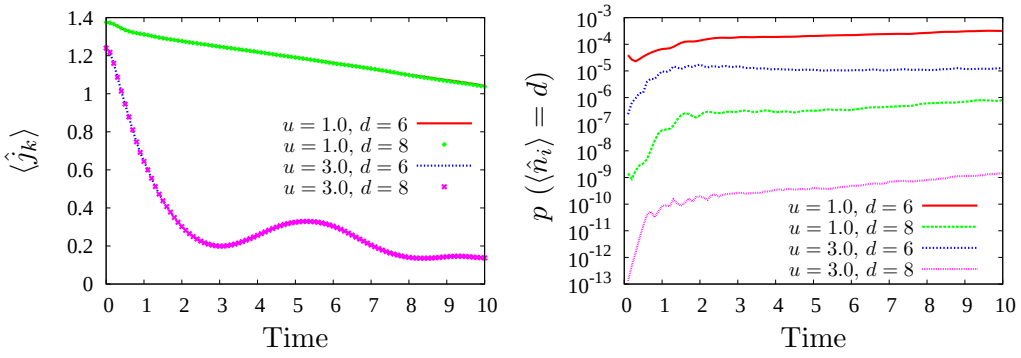

Figure 3.8: The left plot shows a comparison between the boson current evolution computed with local dimensions $d = 6$ and $d = 8$ for $u = 1.0$ and $u = 3.0$ with quasi momentum kick $ka = 0.25\pi$. Only differences of less than 0.5% are visible. The right picture shows the time evolution of the local probabilities for d particles being at one particular site. In the cases of larger on-site interactions, the particles are localised to a larger extent and the probability for high single site occupations in the $\bar{n} = 1$ case decreases.

We find that on the scale we analyse the boson current, almost no differences (smaller than 0.5%) are visible comparing calculations with $d = 6$ to $d = 8$. The probabilities for the maximum single site occupation remains smaller than 10^{-3} for all values of u. The error by setting a limited local dimension increases with decreasing on-site interaction, since in that case the state of the system is delocalised to a larger extent and states with higher occupations on single sites become more probable.

3. We are splitting the full evolution operator $\hat{U} \equiv e^{-i\hat{H}t}$ into two-site gates, employing a 4th order Suzuki-Trotter decomposition (Section 2.2.3). Hence, sufficiently small time-steps Δt have to be used to keep the errors from the non-commutativity between these two-site gates small. Due to the high order of our decomposition, we use time-steps of $\Delta t = 0.1$ ($J \equiv \hbar \equiv 1$) in all our simulations. We compared results to calculations with smaller time-steps and confirmed that the Trotter error is thereby reduced well below other errors occurring during the simulations.

   An example simulation, comparing time steps of $\Delta t = 0.1$ with time-steps $\Delta t = 0.05$ is shown in figure 3.9. Like in figure 3.6 we compare a system kicked with quasi-momentum $ka = 0.25\pi$, for values of $u = 0.5, 1.0, 2.0, 3.0$. The truncation parameter is $\chi = 100$.

   We find that the differences in figure 3.9 are very small and even give

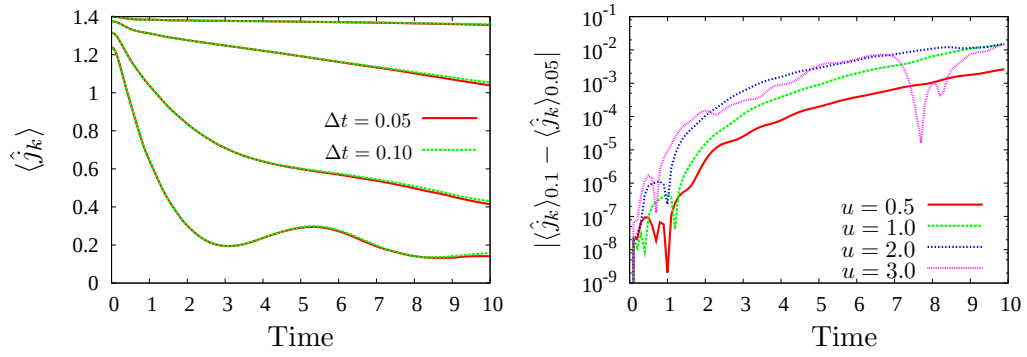

Figure 3.9: Time evolution of the boson current after a momentum kick of $ka = 0.25\pi$ with $u = 0.5, 1.0, 2.0, 3.0$ (from the top to the bottom) for different values of the time step $\Delta t = 0.1$ and $\Delta t = 0.05$ (left side) and the absolute differences between the curves (right side). Even the fast decaying initial behaviour for $u = 3.0$ is simulated correctly in the case of $\Delta t = 0.1$

rise to the correct fast decaying behaviour for small times in the rapid decaying case of $ka = 0.40\pi$. The differences are only increasing in regions where the errors from the Hilbert space truncation becomes relevant and therefore do not originate from the Trotter error.

3.3 iTEBD Results

We are now going to show the results of our numerical simulations of the bosonic transport properties in an infinite homogeneous 1D Bose-Hubbard model. We will first examine the properties immediately after translating the ground states of our systems by an amount of ka in quasi momentum space. We then start the real time simulations and will observe some example curves of decaying boson currents and quasi condensate fractions. The dynamics of the decay, i.e. the change in the off-diagonal long-range properties with time as well as the evolution of the MDF will be analysed for varying u and ka. Finally we present a stability crossover diagram as sketched in figure 3.5, separating regions of specific quasi momenta ka and on-site interactions u that exhibit superfluid behaviour on long timescales from regions of rapid current decay.

3.3.1 Properties at t=0

We can verify the properties of the state at time $t = 0$, immediately after applying the operator $\hat{K}(ka)$ to the ground state. For the case that the kick

operator is applied to an ideal SF ground state, the expectation value of the current operator was calculated in (3.26). For a filling factor of $\bar{n} = 1$ it reads

$$\langle \hat{j}_n \rangle = 2 \sin(ka) \tag{3.32}$$

at all sites n of the homogeneous infinite system. In section 3.1.2, it was further argued that introducing interactions between the particles will lead to a general decrease of these values. Finally in the ideal MI limit with $u \to \infty$, the initial boson current is expected to completely vanish.

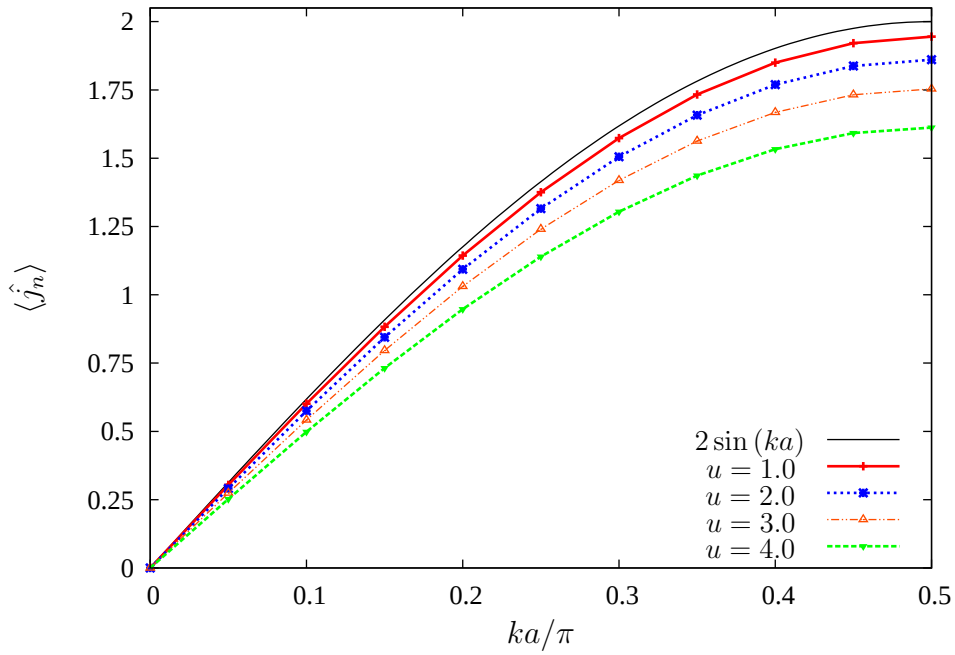

Figure 3.10: Boson current expectation value $\langle \hat{j}_n \rangle$ immediately after applying the initial momentum kick operator $\hat{K}(ka)$ to the ground for several on-site interactions $u = 1.0, 2.0, 3.0, 4.0$.

We find very good agreement with this prediction, shown in figure 3.10. We plot the values of $\langle \hat{j}_n \rangle$ that arise from an application of the operator $\hat{K}(ka)$ with quasi momentum ka ranging from 0.05π to 0.5π. Curves are shown for several values of the on-site interaction u, ranging from $u = 1.00$ to $u = 4.0$, including the SF-MI transition at $u_c \approx 3.37$. It is interesting that even in the MI case at $u = 4.0$, the current only decreases by a relatively small amount from the ideal SF case. This indicates a still existent off-diagonal order in the MI regime, decaying exponentially though. We conclude that the regime

of the ideal non-current allowing MI ground state for which equation (3.29) holds is located at on-site interactions $u \gg 4$.

3.3.2 Current / Condensate Fraction Decay

After computing the ground states for $0.5 \leq u \leq 4.0$ and applying the kick operator with $0.05\pi \leq ka \leq 0.5\pi$, we simulate the real time evolution of the boson current and the condensate fraction for times $0 \leq t \leq 10$ ($J \equiv \hbar \equiv 1$). We thereby find considerable differences in the decay for different values of ka and u. Figure 3.11 shows the time evolution of $\langle \hat{j}_n \rangle$ for a constant initial momentum kick $ka = \pi/10$ with increasing values of the on-site interaction u, ranging from the SF to the MI regime. The second example in figure 3.11 shows the differences of the decay for a fixed on-site interaction of $u = 1.0$ whilst increasing initial quasi momentum kicks.

We find a constant superfluid current only in the case of very small values of $ka = 0.1\pi$ at $u = 1.0$. For a slightly increased initial quasi momentum or on-site interaction ($ka = 0.2\pi$ at $u = 1.0$ and $ka = 0.1\pi$ at $u = 2.0$), a small decay of about 10% on the timescale of the simulation becomes visible. With further increasing ka and u ($u = 3.0$ at $ka = 0.1\pi$ and $ka = 0.3\pi$ at $u = 1.0$) the decay increases rapidly. For $u \gtrsim 3.0$ at $ka = 0.1\pi$ and $ka \gtrsim 0.3\pi$ at $u = 0.1$, the current has completely vanished at $t = 10$.

Qualitatively, we find that the dependence of the current decay on ka and u is analogous to the behaviour of the condensate fraction $\mathcal{C}_{100}$ decay on these two quantities. In figure 3.12 the same plot as for the boson currents in figure 3.11 is shown for the evolution of the quasi condensate fraction, which is obtained by diagonalising the SPDM for a finite region of 100 sites.

A very important result that is clear from both figure 3.11 and figure 3.12 is that we do not find a sharp transition point in terms of certain values of u and ka separating the current evolution into superfluid and non-superfluid regions. Such sharp transition points are found in a Gutzwiller mean-field analysis in [6]. But, like suggested in [6] for a 1D system in which large quantum fluctuations destroy the sharp mean-field transition, we find a broad crossover and superfluidity can only be distinguished from non-superfluidity on a certain timescale.

We are going to further investigate this smooth crossover behaviour by looking at snapshots of the normalised condensate fraction decay. We define this quantity by

$$\Delta\mathcal{C}_S(\tau) \equiv \frac{|\mathcal{C}_S(t=\tau) - \mathcal{C}_S(t=0)|}{\mathcal{C}_S(t=0)}. \tag{3.33}$$

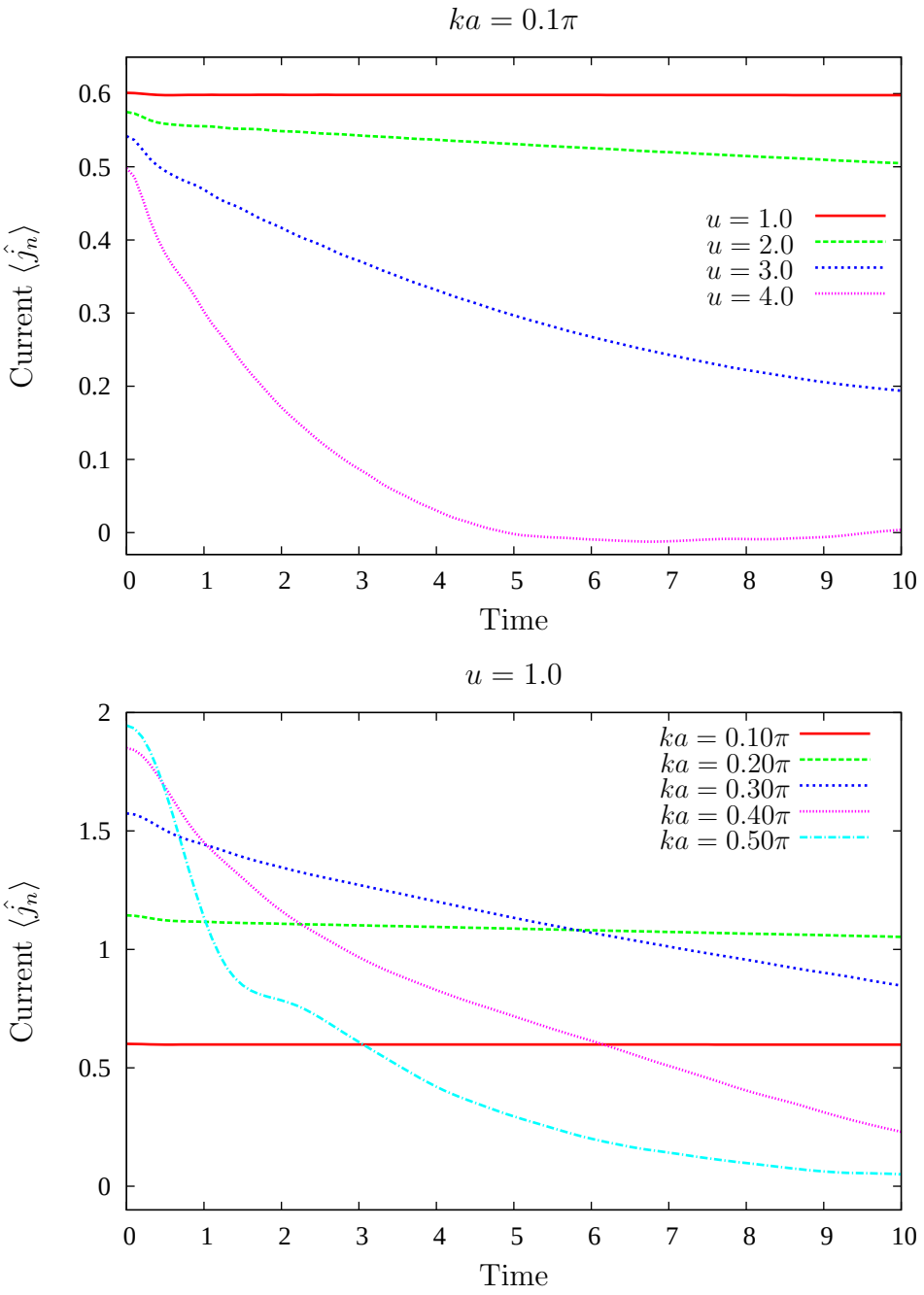

Figure 3.11: Time evolution of the boson current $\langle \hat{j}_n \rangle$, ranging from superfluid behaviour to rapid decay for increasing values of $u = 1.0, 2.0, 3.0, 4.0$ for a small initial momentum kick of $ka = 0.10\pi$ and for varying initial kicks $ka = 0.1\pi, 0.2\pi, 0.3\pi, 0.4\pi, 0.5\pi$ at fixed on-site interaction $u = 1.0$.

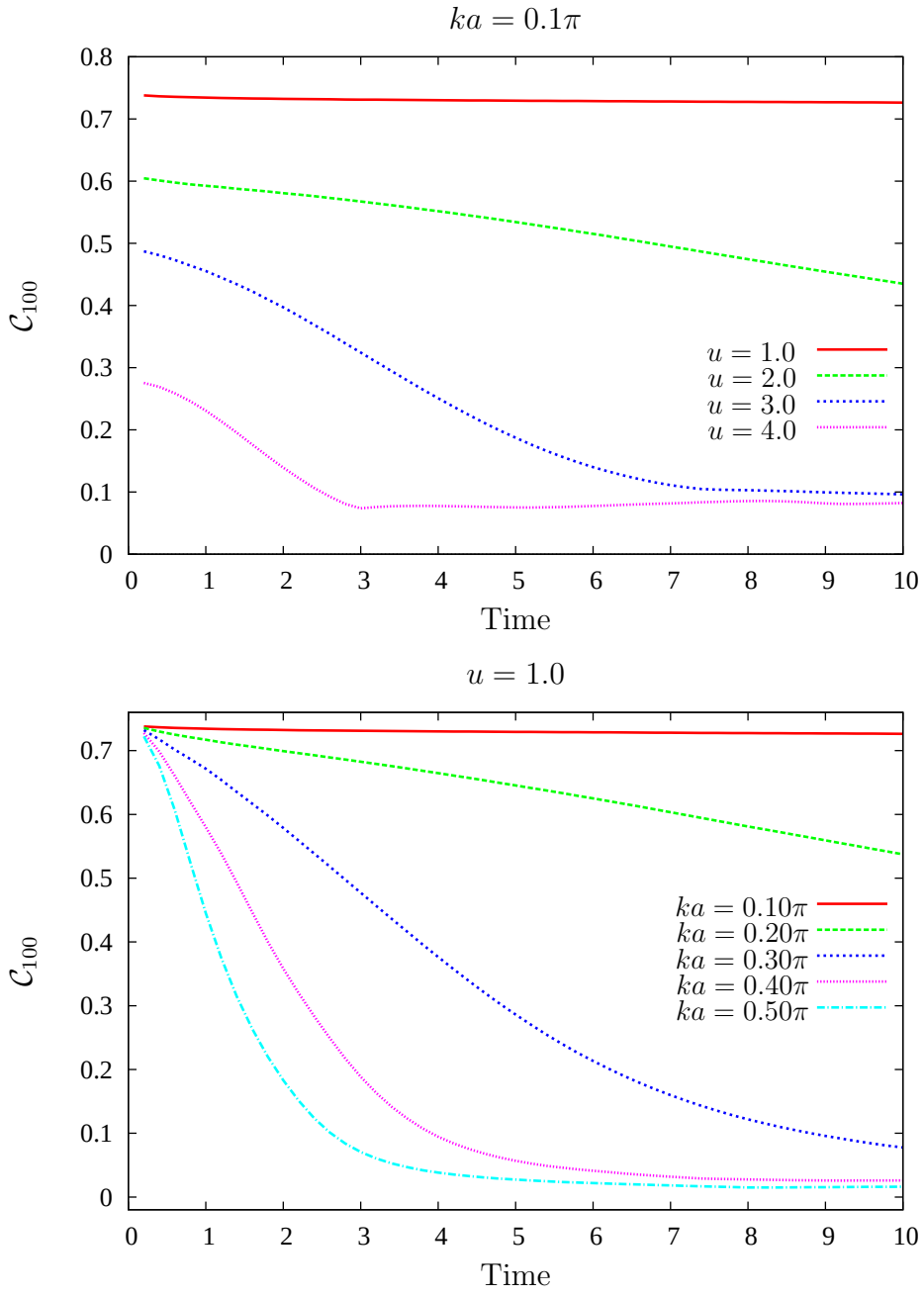

Figure 3.12: Time evolution of the condensate fraction $\mathcal{C}_{100}$, ranging from superfluid behaviour to rapid decay for increasing values of $u = 1.0, 2.0, 3.0, 4.0$ after a small initial momentum kick of $ka = 0.10\pi$, and for varying initial kicks $ka = 0.1\pi, 0.2\pi, 0.3\pi, 0.4\pi, 0.5\pi$ at fixed on-site interaction $u = 1.0$. The behaviour is analogous to the boson current in figure 3.11.

$\Delta\mathcal{C}_S$ at time τ is one in the case that the quasi condensate fraction has completely vanished at τ and zero if no decay has occurred. Figure 3.13 visualises the broad crossover by showing $\mathcal{C}_{100}$ at several times for a constant on-site interaction $u = 1.0$ whilst changing the initial quasi momentum kick from $ka = 0.05\pi$ to $ka = 0.5\pi$.

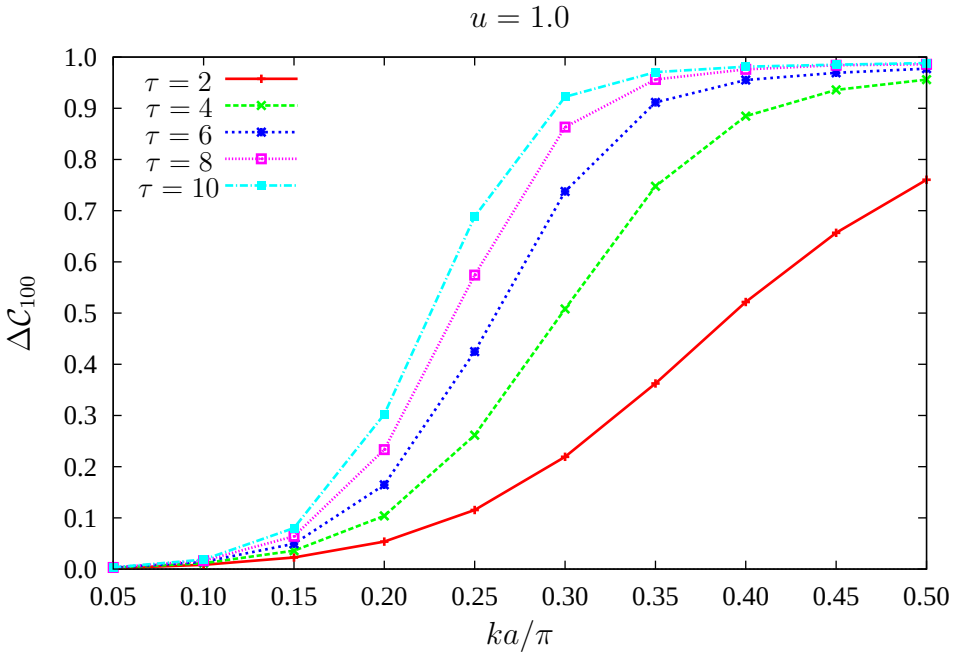

Figure 3.13: Time snapshots of the decay of the condensate fraction $\Delta\mathcal{C}_{100}$ for constant $u = 1.0$ as a function of ka.

A similar plot is obtained when crossing the boundary of superfluid to non-superfluid regions at a constant value of the initial momentum kick of $ka = 0.1\pi$ and varying the on-site interactions from $u = 0.5$ to $u = 4.0$. Results are shown in figure 3.14.

In figure 3.14 the condensate fraction decay seems to decrease again for especially large on-site interactions. However, this effect can be explained by oscillations of the boson current when dropping to zero quickly and is therefore present in the case of large on-site interactions, e.g. $u = 3.5$ and $u = 4.0$ and large kick strengths. This effect of "revival" of the current can for example already be observed in figures 3.11 and 3.12 for $u = 4.0$ and in figure 3.6 for the curve of $u = 3.0$. When the boson current decreases rapidly it starts oscillating, whereas the condensate fraction reaches a minimum at the beginning of these oscillations and then starts to slowly increase again.

In both figures 3.13 and 3.14, the transition curves seem to converge to

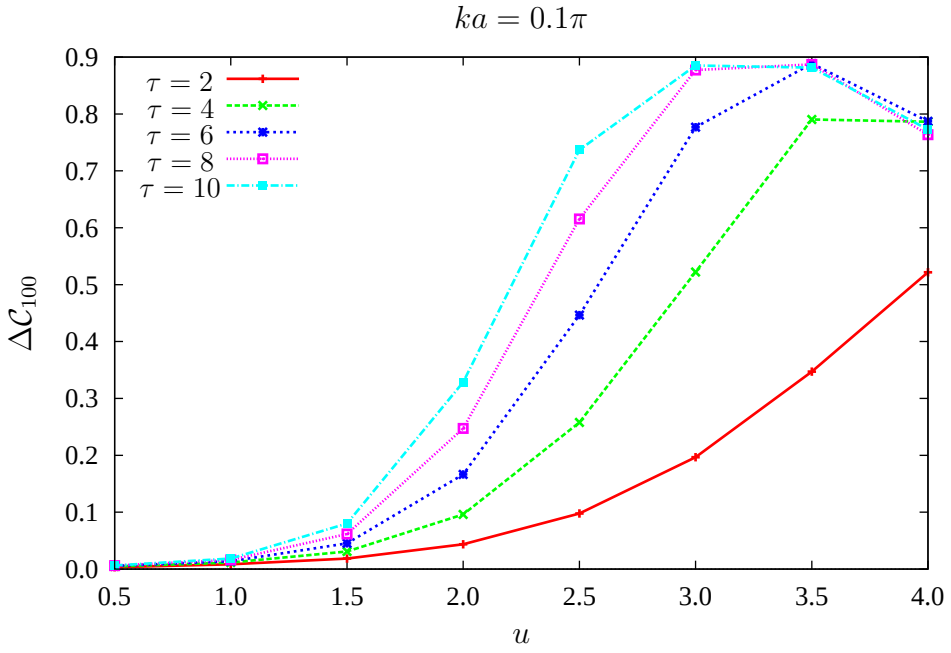

Figure 3.14: Time snapshots of the decay of the condensate fraction $\Delta\mathcal{C}_{100}$ when crossing the "instability boundary" at a constant quasi momentum kick of $ka = 0.1\pi$ as a function of u. The results are similar to figure 3.13.

a crossover with a fixed shape of non-zero transition width for times $\tau \gg 10$. This shape does not have the form of a Θ function, which would be the case if a sharp transition was present. Simulation of the system over larger timescales becomes inefficient, as the errors due to the Hilbert space truncations grow too large, resulting in qualitatively differences of the decay behaviour for different values of the truncation parameter χ. Thus, it remains unclear if the "slightly" superfluid currents, decreasing only little over the simulation timescale will saturate at some fixed value or finally also decay to zero.

However, we are not mainly interested in exact values of the condensate fraction $\mathcal{C}_{100}$, which is calculated over an artificially finite region of our infinite system, but we want to make a statement about the shape of a superfluid to non-superfluid crossover on experimentally observable timescales. These are of the order of 10 ms for typical ^{87}Rb experiments like [4, 7], and could in principle be extended up to the order of seconds due to the good isolation of lattice systems from their environment. In regions where the Bose-Hubbard model is valid, the typical lattice depth V_0 is of the order of 10 E_R, where E_R denotes the recoil energy of the atoms $E_R \equiv p_r^2/2m$ with the recoil momentum

$p_r \equiv h/\lambda_l$. For these lattice depths, the tunnelling parameter $J/\hbar$ is of the order of 100 Hz. Thus, since our simulation time is given in units of $1/J$ with $J \equiv \hbar \equiv 1$, a time of $\tau = 10$ corresponds to a time of the order of 100 ms in realistic experiments, depending of the utilised lattice depth V_0. Therefore, simulating up to a time of $\tau = 10$ in our units already reflects the behaviour over an interesting experimentally observable timescale.

3.3.3 Dynamics of the Decay

Origins of the current stability or instability can be observed by analysing time dependently the properties of the SPDM and the MDF.

Time Evolution of the Off-Diagonal SPDM Order

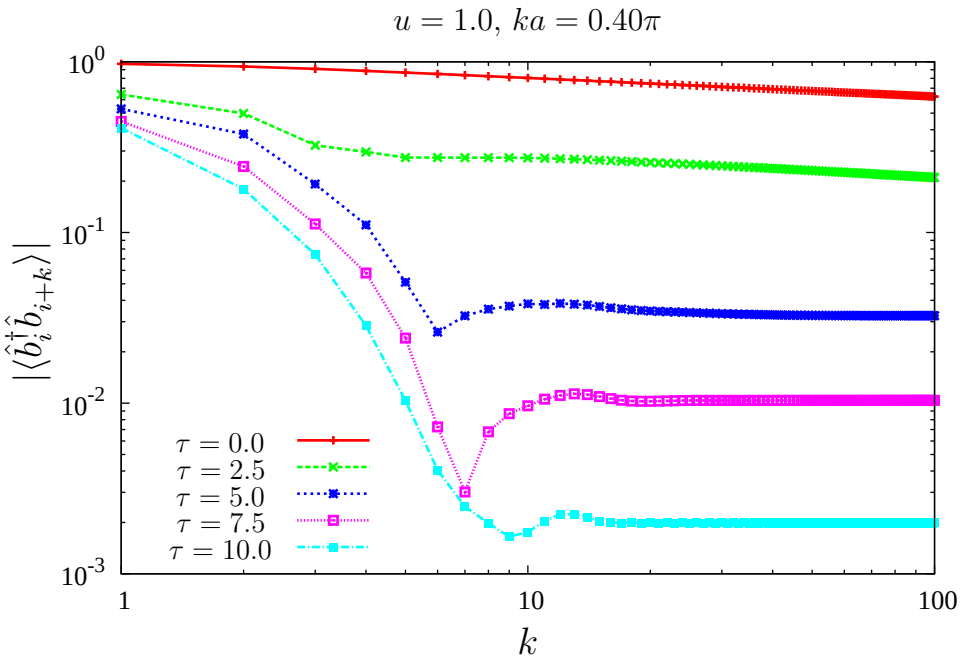

Figure 3.15: The evolution of the off-diagonal long-range order for an initially SF ground state ($u = 1.0$), which is kicked by $ka = 0.40\pi$. The initially algebraic decay is converted into an exponential one.

In Fig. 3.15 the off-diagonal elements of the SPDM are shown at several times of the evolution. Initially the system is in a SF ground state with $u = 1.0$ and is translated by $ka = 0.40\pi$ in quasi momentum space. As we

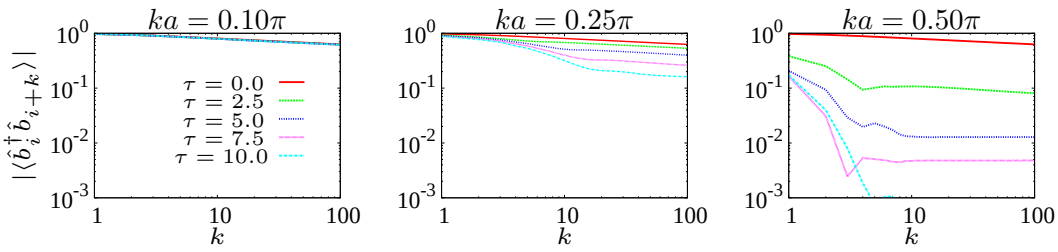

Figure 3.16: More examples for the evolution of the off-diagonal elements in the SPDM for an initially SF ground state ($u = 1.0$), kicked with several values of ka.

know from figures 3.11 and 3.12, the boson current is going to decay to zero in this example.

We find that the off-diagonal correlation starts to decrease rapidly. Over a large off diagonal distance that increases with time, the decay of the long range order is converted from an algebraic into an exponential one. The $\tau = 10$ state is found to have an exponentially decaying off-diagonal SPDM elements over approximately 10 sites like in a MI ground state case. Therefore, we conclude that in the case of a non-superfluid boson-current decay, the quasi condensate is destroyed and the particles are redistributed into a localised final state from the initial quasi-condensate mode.

In figure 3.16, more examples for the time-dependence of the off-diagonal SPDM elements are shown for stable superfluid behaviour ($u = 1.0$, $ka = 0.10\pi$), intermediate behaviour ($u = 1.0$, $ka = 0.25\pi$) and rapid decay ($u = 1.0$,$ka = 0.50\pi$). In the superfluid case, we find that the off-diagonal long-range order is completely preserved over the full simulation time.

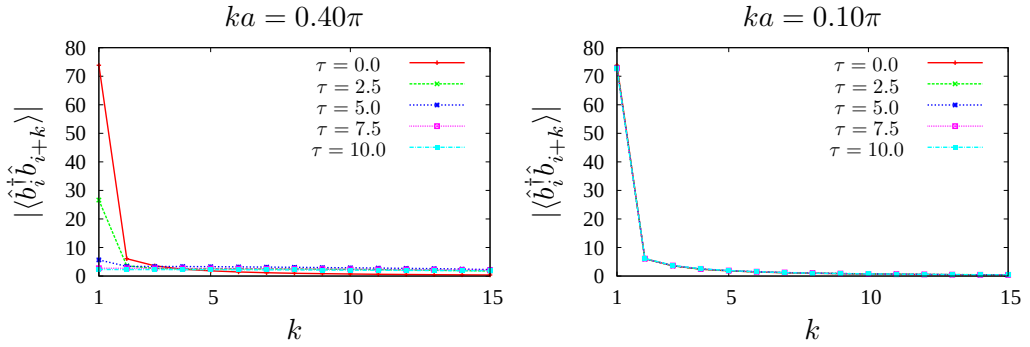

Figure 3.17: The evolution of the eigenvalue spectrum of the SPDM from a diagonalisation in a region of 100 sites for an initially SF ground state ($u = 1.0$), which is kicked by $ka = 0.10\pi$ and $ka = 0.40\pi$.

Alternatively, the loss of the quasi condensate in the case of a decaying

current can also be analysed by observing the time-evolution of the eigenvalue spectrum of the SPDM that is evaluated for a finite region of the system of 100 sites as shown in figure 3.17.

We find, that in the case of decaying current with $ka = 0.40\pi$, the large occupation of the first SPDM eigenstate has vanished at the end of the simulation, whereas in the superfluid case of $ka = 0.10\pi$, the largest eigenvalue remains constant in time.

Time Evolution of the MDF

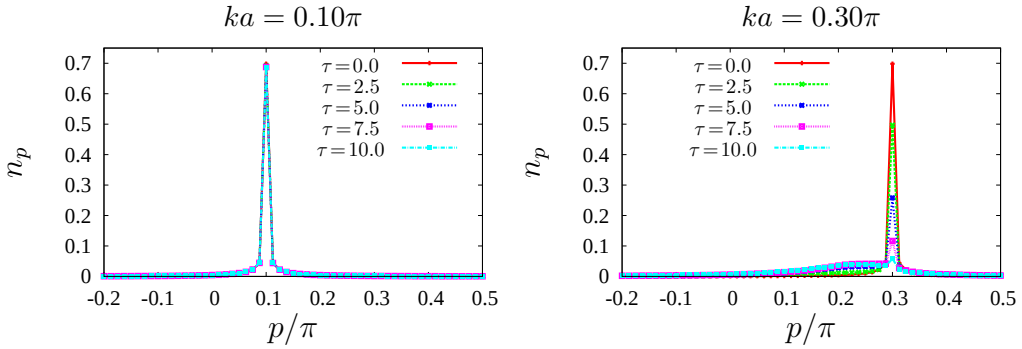

Figure 3.18: The time evolution of the MDF in the stable superfluid regime at $u = 1.0$ after a momentum kick of $ka = 0.10\pi$ and in the unstable regime in case of a momentum kick of $ka = 0.30\pi$.

We can analyse the time evolution of the quasi momentum distribution function after the quasi-momentum translation due to the application of the kick operator. In figure 3.18 we observe the system in the stable superfluid region of $u = 1.0$ and $ka = 0.10\pi$ and compare the decay behaviour to the non-stable case, when applying a kick of $ka = 0.30\pi$.

As expected from the previous results, in 3.18 we observe an almost completely stable momentum distribution if $\hat{K}(0.10\pi)$ is applied. The sharp peak almost remains constant in terms of width and position in quasi momentum space. If instead a kick of $ka = 0.3\pi$ is applied, at $t = 10$ the particles have completely redistributed from the initially sharp peak to a new much broader MDF at a lower average quasi momentum. The increasing width of the distribution is again related to the fact that the final state is localised and off diagonal correlations are decaying exponentially. However, as was already seen in figure 3.11, the current and therefore also the average quasi momentum has not completely decayed to zero at $t = 10$.

We can compare this dynamics of the MDF to regimes of stronger on-site interactions in which case we expect a much faster decay. Therefore, we

show the same plots as in figure 3.18 for an increased interaction of $u = 3.0$ in figure 3.19.

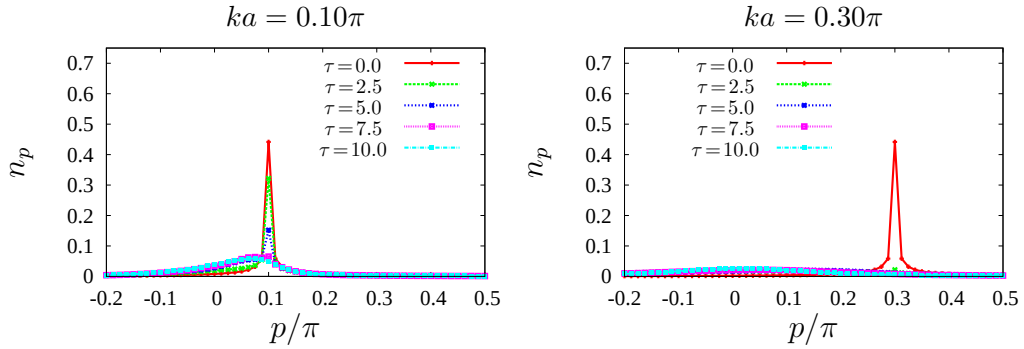

Figure 3.19: The same plot like in figure 3.18 but with a larger on-site interaction of $u = 3.0$, showing the time evolution of the MDF for momentum kicks of $ka = 0.1, 0.3$.

We observe similar dynamics of the decay for the case of $u = 3.0$ with $ka = 0.1\pi$ as for $u = 1.0$ and $ka = 0.3\pi$ in figure (3.18). This is not surprising, since also the behaviour of the current and the condensate fraction decay in figures 3.11 and 3.12 is similar. For a momentum kick of $ka = 0.3\pi$ at $u = 3.0$, however, we find an extremely rapid decay and already at time $\tau = 2.5$ the sharp peak has completely vanished. In this case, the final state at $\tau = 10$ has a very broad MDF with a FWHM of approximately half of the first Brillouin zone and is distributed around zero quasi momentum.

3.3.4 Stability Crossover Diagram

Finally, we present results for a stability crossover diagram as sketched in figure 3.5. To obtain this diagram from our simulations we are observing time-snapshots of the decay of the boson current, which we define as

$$\Delta\langle\hat{j}_n\rangle(\tau) \equiv \frac{|\langle\hat{j}_n\rangle(t=\tau) - \langle\hat{j}_n\rangle(t=0)|}{\langle\hat{j}_n\rangle(t=0)}, \tag{3.34}$$

and the decay of the condensate fraction $\Delta\mathcal{C}_S$ as defined in (3.33) on a ka-U grid. We use on-site interaction values of $0.5 \leq u \leq 4.0$ with grid spacing of $\Delta u = 0.5$ and quasi momentum kicks between $0.05\pi \leq ka \leq 0.50\pi$ with spacing $\Delta ka = 0.05\pi$. To get smooth results, we use a spline interpolation between the data points. To see a convergence effect within our timescale like in figures 3.13 and 3.14 we build the crossover diagram for times $\tau = 4$, $\tau = 7$ and $\tau = 10$.

The results for the boson current decay are shown in figure 3.20, the same plots for the quasi condensate fraction decay obtained from a diagonalisation of the SPDM over 100 sites is shown in figure 3.21.

The behaviour in the stability crossover diagrams is more clear from the condensate fraction decay $\Delta\mathcal{C}_{100}$ than from the current decay $\Delta\langle\hat{j}_n\rangle$, because as we have seen earlier, the decay behaviour of the current exhibits oscillations, whereas the condensate fraction typically decreases monotonically (see figures 3.11 and 3.12).

In both, figure 3.20 and 3.21 we find regions with real superfluid behaviour for values of $u \lesssim 1.5$ and $ka \lesssim 0.15\pi$ and regions where the current vanishes for $u \gtrsim 2.5$ and $ka \gtrsim 0.25\pi$. In the intermediate region we observe a smooth crossover. The width of this crossover region is decreasing for increasing times $\tau = 4, 7, 10$, however the shape remains identical at all three times. We verify that in the classical limit of small on-site interactions, the stability crossover tends to the classical limit of $ka = 0.5\pi$ and for $ka \approx 0$ to the vicinity of the SF-MI transition at $u_c \approx 3.37$. We find that the critical momentum kicks and on-site interactions are in general smaller than predicted by a Gutzwiller mean-field analysis in [6], in which the transition curve interpolates between the classical instability limit and the mean-field critical on-site interaction of $u_c = 11.6$.

The shape of this crossover should be directly accessible in experiments like [7]. The application of the kick operator can be implemented by accelerating the lattice potential via detuning the counterpropagating laser beams forming the lattice. The time evolution of condensate fractions can be evaluated in time-of-flight measurements after switching off all confining potentials [7]. Also in the experiment, a condensate fraction will be visible due to the finite size of the observed system.

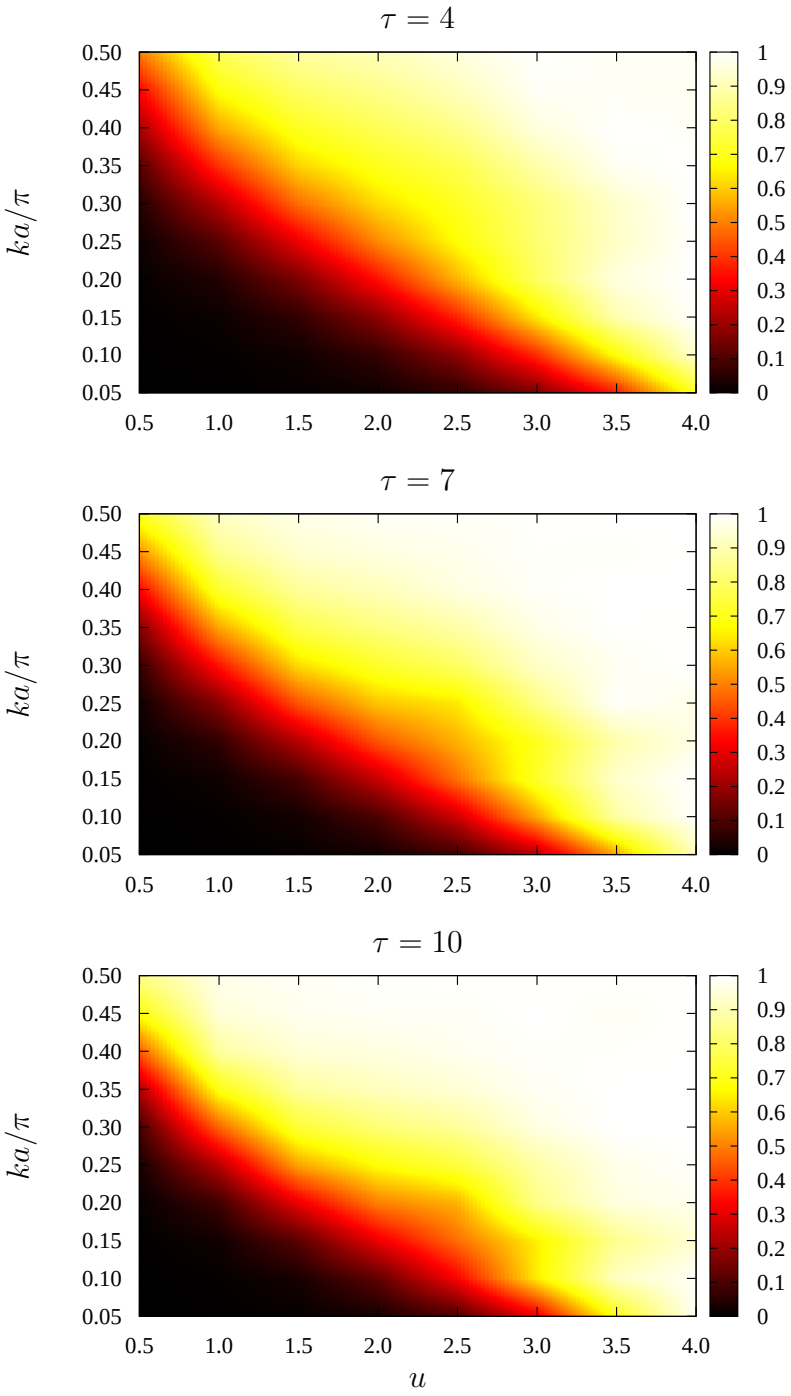

Figure 3.20: Stability crossover, visualised by an interpolation between values of the boson current decay $\Delta\langle\hat{j}_n\rangle(\tau)$ at times $\tau = 4, 7, 10$.

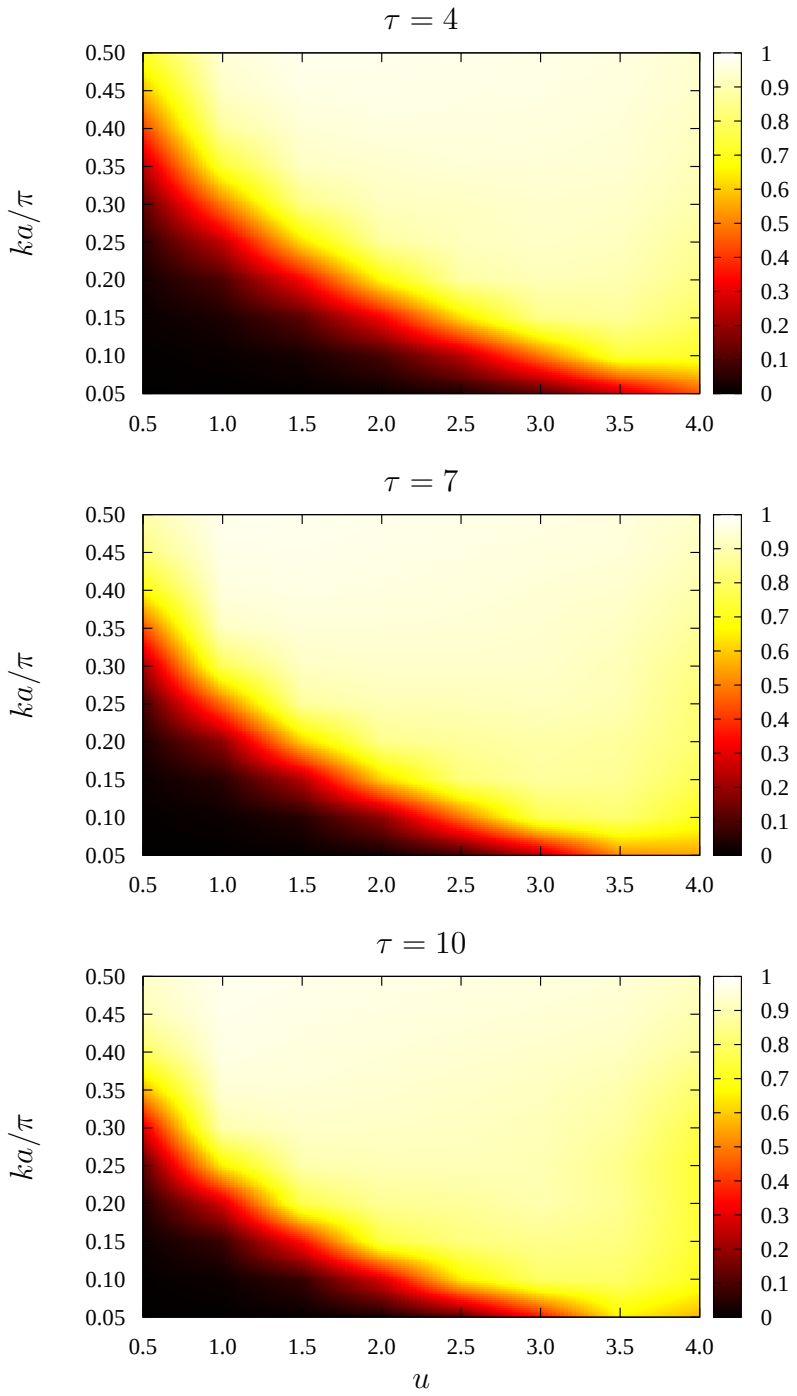

Figure 3.21: Stability crossover, visualised by an interpolation between values of $\Delta\mathcal{C}_{100}$ at times $\tau = 4, 7, 10$.

Bibliography

[1] M. Greiner, O. Mandel, T. Esslinger, T. W. Hänsch, and I. Bloch. *Nature* **415**, 39 (2002).

[2] M. P. A. Fisher, P. B. Weichman, G. Grinstein, and D. S. Fisher. *Phys. Rev. B* **40**, 546 (1989).

[3] D. Jaksch, C. Bruder, J. I. Cirac, C. W. Gardiner, and P. Zoller. *Phys. Rev. Lett.* **81**, 3108 (1998).

[4] L. Fallani, L. De Sarlo, J. E. Lye, M. Modugno, R. Saers, C. Fort, and M. Inguscio. *Phys. Rev. Lett.* **93**, 140406 (2004).

[5] E. Altman, A. Polkovnikov, E. Demler, B. I. Halperin, and M. D. Lukin. *Phys. Rev. Lett.* **95**, 020402 (2005).

[6] A. Polkovnikov, E. Altman, E. Demler, B. Halperin, and M. D. Lukin. *Phys. Rev. A* **71**, 063613 (2005).

[7] J. Mun, P. Medley, G. K. Campbell, L. G. Marcassa, D. E. Pritchard, and W. Ketterle. *Phys. Rev. Lett.* **99**, 150604 (2007).

[8] A. J. Daley. "The Physics of Cold Atoms", Lecture notes, Summer term 2008, University of Innsbruck.

[9] T. D. Kühner, S. R. White, and H. Monien. *Phys. Rev. B* **61**, 12474 (2000).

[10] W. Krauth, M. Caffarel, and J. Bouchaud. *Phys. Rev. B* **45**, 3137 (1992).

[11] A. Smerzi, A. Trombettoni, P. G. Kevrekidis, and A. R. Bishop. *Phys. Rev. Lett.* **89**, 170402 (2002).

[12] B. Wu and Q. Niu. *Phys. Rev. A* **64**, 061603 (2001).

Chapter 4

Simulation of Long-Range Interactions

In chapter 2 we introduced the TEBD algorithm, originally proposed by G. Vidal [1], which makes it possible to perform simulations of the time evolution and to compute ground states of a 1D quantum system with lattice Hamiltonians containing next-neighbour terms. However, to simulate physical systems with long-range interactions it is also desirable to have algorithms at hand making possible the implementation of Hamiltonians with terms ranging over several sites. Some ideas for achieving this task have already been presented, which either use techniques complementing the existing TEBD algorithm [2] or introduce completely new ideas, for example the use of matrix product evolution operators [3–6].

In this chapter we complement the TEBD algorithm using the idea of swapping lattice site indices. First we present how this idea can be implemented for finite systems and introduce a long-range TEBD algorithm, which we will denote lTEBD (Section 4.1). As in section 2.2 we will then extend this algorithm to infinite systems by exploiting translational invariance in homogeneous systems. In keeping with our preceding notation we shall abbreviate this algorithm ilTEBD (Section 4.2).

4.1 Long Range TEBD (lTEBD)

As we have presented it so far, TEBD is only capable of simulating real or imaginary time evolution according to Hamiltonians containing solely next-neighbour terms. This is because we have only provided a scheme for updating a MPS due to the application of next-neighbour gates. For longer range interactions, a Suzuki-Trotter expansion will require applications of evolution

operators that include contributions beyond nearest-neighbour terms.

The removal of this limitation is important in order to simulate physical systems with interactions decaying slowly over a certain range. An example is given in chapter 5, where a system of Rydberg-atoms excited in an an optical lattice potential, exhibiting dipolar long-range interactions is simulated.

To include long-range interactions into our calculations, we use an approach that is based on the existing TEBD framework, i.e. we utilise the MPS representation introduced in section 2.1.1. Additionally, we present a scheme to apply long-range gates to a MPS. The main conceptual idea is the process of swapping lattice indices, first suggested by Y.-Y. Shi et al. in [2].

We will first introduce the idea of swapping indices and show how this can be used for the implementation of long-range gates. We will then introduce a way of grouping these gates into sweeps in a Suzuki-Trotter expansion and present the lTEBD algorithm. This algorithm is capable of simulating systems with long-range interactions and only requires a small computational overhead compared to the standard TEBD version.

4.1.1 Swapping Indices

Before we present the implementation for MPS representations, we introduce the conceptual idea of swapping indices.

3 Site Long Range Gate

Consider a system with 3 sites, where we want to apply a long-range gate between sites 1 and 3 to the state

$$|\Psi\rangle \equiv \sum_{i_1,i_2,i_3} c_{i_1,i_2,i_3} |i_1 i_2 i_3\rangle, \tag{4.1}$$

with basis vectors $|i_1 i_2 i_3\rangle \equiv |i_1\rangle_1 \otimes |i_2\rangle_2 \otimes |i_3\rangle_3$. The long-range gate $\hat{U}_{1,3}$ reads

$$\hat{U}_{1,3} \equiv \sum_{i_1,i_2,i_3} \sum_{i'_1,i'_3} U^{i'_1,i'_3}_{i_1,i_3} |i'_1 i_2 i'_3\rangle\langle i'_1 i_2 i'_3|. \tag{4.2}$$

The operator (4.2) can be rewritten as

$$\begin{aligned}\hat{U}_{1,3} &= \sum_{i_1,i_2,i_3}\sum_{i_1',i_3'} U_{i_1,i_3}^{i_1',i_3'}|i_1' i_2 i_3'\rangle \sum_{k_1,k_2,k_3}\langle i_1' i_3' i_2|k_1 k_2 k_3\rangle\langle k_1 k_3 k_2| \\ &\equiv \sum_{i_1,i_2,i_3}\sum_{i_1',i_3'} U_{i_1,i_3}^{i_1',i_3'}|i_1' i_2 i_3'\rangle\langle i_1' i_3' i_2|\hat{S}_{2,3}^\dagger \\ &= \sum_{i_1,i_2,i_3}\sum_{i_1',i_3'} U_{i_1,i_3}^{i_1',i_3'}\hat{S}_{2,3}|i_1' i_3' i_2\rangle\langle i_1' i_3' i_2|\hat{S}_{2,3}^\dagger \\ &\equiv \hat{S}_{2,3}\hat{U}_{1,2}\hat{S}_{2,3}, \end{aligned} \tag{4.3}$$

where in the second line, the swap operator

$$\hat{S}_{2,3} \equiv \sum_{k_1,k_2,k_3} |k_1 k_3 k_2\rangle\langle k_1 k_2 k_3| = \hat{S}_{2,3}^\dagger, \tag{4.4}$$

and in the last line, the two-site gate $\hat{U}_{1,2}$, which acts on sites 1 and 2 with the same functional form of $\hat{U}_{1,3}$

$$\hat{U}_{1,2} \equiv \sum_{j_1,j_2,j_3}\sum_{j_1',j_2'} U_{j_1,j_2}^{j_1',j_2'}|j_1' j_2' j_3\rangle\langle j_1' j_2' j_3| \tag{4.5}$$

has been defined. The swap-gate (4.4) simply interchanges the indices between sites 2 and 3. Thus, applying U_{13} to the state $|\Psi\rangle$ is equivalent to the application of the same gate on sites 1 and 2 after swapping 2 and 3 followed again by an index interchange of 2 and 3 to restore the original order.

Long Range Gate in a N-Site System

The case of larger systems is analogous. By introducing a general swap-gate for an N-site system (basis $|i_1 i_2 \dots i_n\rangle \equiv |i_1\rangle_1 \otimes |i_2\rangle_N \otimes \cdots \otimes |i_N\rangle_N$), interchanging indices i and $i+1$

$$\hat{S}_i \equiv \sum_{k_1,\dots,k_i,k_{i+1},\dots,k_N} |k_1 \dots k_{i+1} k_i \dots k_N\rangle\langle k_1 \dots k_i k_{i+1} \dots k_N|, \tag{4.6}$$

it immediately follows that any long-range gate $\hat{U}_{i_1,i_2}$, which acts over $l = i_1 - i_2$ sites can be decomposed into

$$\begin{aligned}\hat{U}_{i_1,i_2} &\equiv \sum_{j_1,j_2,\ldots j_N} \sum_{j'_{i_1},j'_{i_2}} U^{j'_{i_1},j'_{i_2}}_{j_{i_1},j_{i_2}} |j_1 \ldots j'_{i_1} \ldots j'_{i_2} \ldots j_3\rangle\langle j_1 \ldots j'_{i_1} \ldots j'_{i_2} \ldots j_3| \\ &= \sum_{j_1,j_2,\ldots j_N} \sum_{j'_{i_1},j'_{i_2}} U^{j'_{i_1},j'_{i_2}}_{j_{i_1},j_{i_2}} \hat{S}_{i_2-1} |j_1 \ldots j'_{i_1} \ldots j'_{i_2} j_{i_2-1} \ldots j_3\rangle \ldots \\ &\qquad\qquad \ldots \langle j_1 \ldots j'_{i_1} \ldots j'_{i_2} j_{i_2-1} \ldots j_3| \hat{S}_{i_2-1} \\ &= \hat{S}_{i_2-1} \hat{U}_{i_1,i_2-1} \hat{S}_{i_2-1}, \end{aligned} \tag{4.7}$$

and equivalently

$$\hat{U}_{i_1,i_2} = \hat{S}_{i_1} \hat{U}_{i_1+1,i_2} \hat{S}_{i_1}. \tag{4.8}$$

Hence, it follows that the full long-range gate $\hat{U}_{i_1,i_2}$ can be expanded into $2(l-1)$ swap-gates and the gate $\hat{U}_{i_1,i_1+1}$, which acts on two neighbouring sites with the same functional form of $\hat{U}_{i_1 i_2}$

$$\hat{U}_{i_1 i_2} = \hat{S}_{i_2-1} \hat{S}_{i_2-2} \ldots \hat{S}_{i_1+1} \hat{U}_{i_1,i_1+1} \hat{S}_{i_1+1} \ldots \hat{S}_{i_2-2} \hat{S}_{i_2-1}. \tag{4.9}$$

Multiple Long Range Gates

If multiple two-site gates have to be applied after each other, like in the Suzuki-Trotter decomposition of the TEBD algorithm, the number of swap-gates can be substantially decreased, saving computational cost. For example, three evolution operators $\hat{U}_{1,2}$, $\hat{V}_{1,3}$ and $\hat{W}_{1,4}$, which act on sites $1 \leftrightarrow 2$, $1 \leftrightarrow 3$ and $1 \leftrightarrow 4$ respectively, can be applied using only 4 instead of 6 swap gates. This can be simply understood, by noting that

$$\begin{aligned}\hat{W}_{1,4} \hat{V}_{1,3} \hat{U}_{1,2} &= (\hat{S}_1 \hat{S}_2 \hat{W}_{3,4} \hat{S}_2 \hat{S}_1)(\hat{S}_1 \hat{V}_{2,3} \hat{S}_1) \hat{U}_{12} \\ &= \hat{S}_1 \hat{S}_2 \hat{W}_{3,4} \hat{S}_2 \hat{V}_{2,3} \hat{S}_1 \hat{U}_{1,2}, \end{aligned} \tag{4.10}$$

where the recursively inserted equation (4.8) and the fact that $\hat{S}_i \hat{S}_i = \mathbb{1}$, which follows immediately from the definition (4.6), has been used.

For a general series of gates, containing operations from next-neighbour to l-site terms $\hat{U}^{(1)}_{i,i+1} \hat{U}^{(2)}_{i,i+2} \ldots \hat{U}^{(l)}_{i,i+l}$, we are further exploiting the condition $\hat{S}_i \hat{S}_i = \mathbb{1}$, by implementing

$$\begin{aligned}\hat{U}^{(1)}_{i,i+1} \hat{U}^{(2)}_{i,i+2} \ldots \hat{U}^{(l)}_{i,i+l} &= \hat{S}_i \ldots \hat{S}_{l-3} \hat{S}_{i+l-2} \hat{U}^{(l)}_{i+l-1,i+l} \hat{S}_{i+l-2} \ldots \\ &\qquad \ldots \hat{U}^{(3)}_{i+2,i+3} \hat{S}_{i+1} \hat{U}^{(2)}_{i+1,i+2} \hat{S}_i \hat{U}^{(1)}_{i,i+1}. \end{aligned} \tag{4.11}$$

This invokes a total of l next-neighbour and $2(l-1)$ swap-gates. In contrast, if only the expansion (4.9) would be used for each two-site operator $\hat{U}$, l next-neighbour and (l^2-l) swap-gates would be required. Thus using (4.11) instead of decomposition (4.9) leads to a computational saving, which is quadratic in l.

4.1.2 Swapping MPS Indices

In the MPS representation (2.15) a swap-gate, which interchanges two neighbouring indices is easy to implement. Consider the two-site expansion (2.32) of the MPS at site l and $m \equiv l+1$

$$|\Psi\rangle = \sum_{i,j} \sum_{\alpha,\beta,\gamma} \lambda_{\alpha}^{[l-1]} \Gamma_{\alpha\beta}^{[l]i} \lambda_{\beta}^{[l]} \Gamma_{\beta\gamma}^{[m]j} \lambda_{\gamma}^{[m]} |i\rangle_l |j\rangle_m |\Phi_{\alpha}^{[l]L}\rangle |\Phi_{\gamma}^{[m]R}\rangle. \tag{4.12}$$

The state vector $|\Psi\rangle$ can be contracted to

$$|\Psi\rangle = \sum_{i,j} \sum_{\alpha,\gamma} \Theta_{\alpha\gamma}^{ij} |i\rangle_l |j\rangle_m |\Phi_{\alpha}^{[l]L}\rangle |\Phi_{\gamma}^{[m]R}\rangle, \tag{4.13}$$

with the matrix

$$\Theta_{\alpha\gamma}^{ij} \equiv \sum_{\beta} \lambda_{\alpha}^{[l-1]} \Gamma_{\alpha\beta}^{[l]i} \lambda_{\beta}^{[l]} \Gamma_{\beta\gamma}^{[m]j} \lambda_{\gamma}^{[m]}. \tag{4.14}$$

For a state vector of the form (4.13), the index interchange can be accomplished, by simply interchanging the i- with the j-elements in the Θ-matrix

$$\tilde{\Theta}_{\alpha\gamma}^{ji} \equiv \Theta_{\alpha\gamma}^{ij}, \tag{4.15}$$

leading to the new state

$$|\tilde{\Psi}\rangle = \sum_{i,j} \sum_{\alpha,\gamma} \tilde{\Theta}_{\alpha\gamma}^{ij} |i\rangle_l |j\rangle_m |\Phi_{\alpha}^{[l]L}\rangle |\Phi_{\gamma}^{[m]R}\rangle. \tag{4.16}$$

Finally, to restore the original truncated MPS form, a Schmidt decomposition of (4.16) followed by an β-index truncation has to be performed, resulting in updated Γ and λ arrays

$$\Theta_{\alpha\gamma}^{lm} \overset{\text{SD}}{=} \sum_{\beta}^{\chi_l} L_{\alpha\beta}^{l} \tilde{\lambda}_{\beta} R_{\beta\gamma}^{m} \overset{\text{Trunc.}}{\approx} \sum_{\beta}^{\chi} \lambda_{\alpha}^{[l-1]} \tilde{\Gamma}_{\alpha\beta}^{[l]i} \tilde{\lambda}_{\beta}^{[l]} \tilde{\Gamma}_{\beta\gamma}^{[m]j} \lambda_{\gamma}^{[m]}. \tag{4.17}$$

This whole process is visualised via

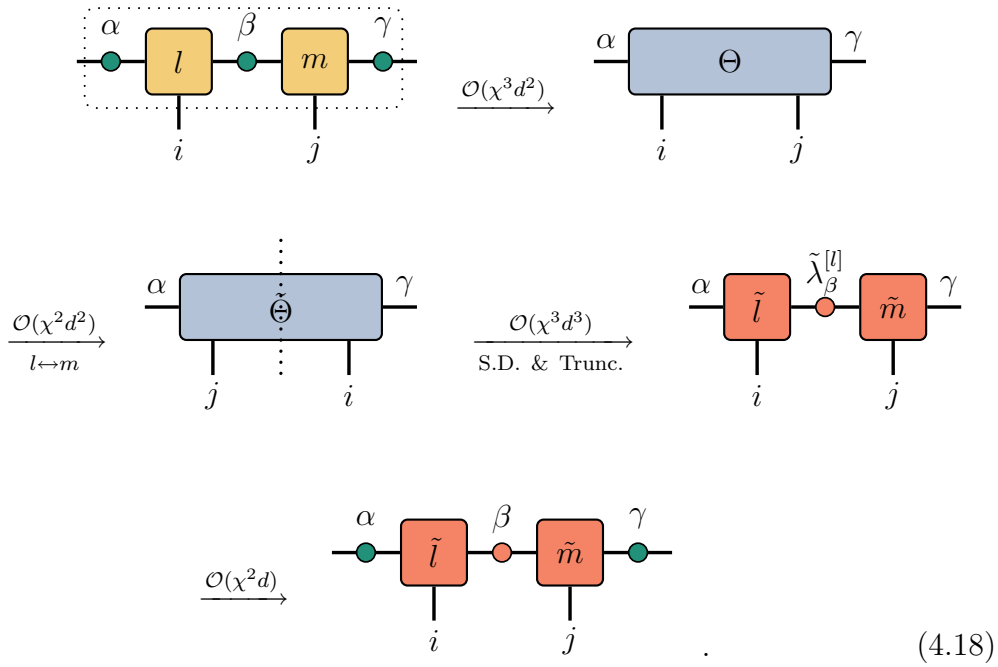

(4.18)

Like for a single two-site evolution step, $\mathcal{O}(\chi^3 d^3)$ basic operations are required for a single swap-gate.

4.1.3 The Algorithm

For the simulation of a full evolution time step, we want to exploit equation (4.11). Consider a N-site system with Hamiltonian $\hat{H}_{\mathrm{LR}}$, containing terms including interactions over a maximum of $l < N$ sites and box-boundary conditions. This implies that $\hat{H}_{\mathrm{LR}}$ can be written as sum over two-site Hamiltonians $\hat{H}_{\mathrm{LR}} \equiv \sum_j^{N-1} \sum_{k;k+j<N}^{l} \hat{H}_{j,j+k}$. Then, the time evolution operator $\hat{U}_{LR} \equiv e^{-i\hat{H}_{\mathrm{LR}}\Delta t}$ for the full system can again be expanded into several repeated sweeps $\hat{P}_{\Delta t'}$ of $[(N-l)l + (l-1)l/2]$ two-site time evolution gates $\hat{U}_{j_1,j_2} \equiv e^{-i\hat{H}_{j_1,j_2}\Delta t}$ with time-steps $\Delta t'$. We are again using a 4th order Suzuki-Trotter decomposition (Equation (2.43)) and therefore 18 sweeps are required.

$$\begin{aligned}\hat{U}_{LR} = {} & \hat{P}_1^T \hat{P}_1 \hat{P}_1^T \hat{P}_{-2} \hat{P}_1^T \hat{P}_1^T \hat{P}_1^T \hat{P}_1^T \hat{P}_1 \hat{P}_1^T \hat{P}_1 \hat{P}_1 \hat{P}_1 \hat{P}_1 \hat{P}_{-2}^T \hat{P}_1 \hat{P}_1^T \hat{P}_1 \\ & + \mathcal{O}(\Delta t^5). \end{aligned} \tag{4.19}$$

Long-Range Sweep

To efficiently implement all gates of a single sweep, we are using the decomposition ($m \equiv N - l$)

$$\hat{P}^{T}_{\Delta t'} = \begin{array}{ccccccc} \hat{U}_{1,2} & \hat{U}_{1,3} & \hat{U}_{1,4} & \dots & \hat{U}_{1,1+l} \\ \hat{U}_{2,3} & \hat{U}_{2,4} & \hat{U}_{2,5} & \dots & \hat{U}_{2,2+l} \\ \vdots & \vdots & \vdots & & \vdots \\ \hat{U}_{m,m+1} & \hat{U}_{m,m+2} & \hat{U}_{m,m+3} & \dots & \hat{U}_{m,N} \\ & \hat{U}_{m+1,m+2} & \hat{U}_{m+1,m+3} & \dots & \hat{U}_{m+1,N} \\ & & \vdots & & \vdots \\ & & & \hat{U}_{N-2,N-1} & \hat{U}_{N-2,N} \\ & & & & \hat{U}_{N-1,N}. \end{array} \tag{4.20}$$

For the sweep $\hat{P}_{\Delta t'}$, the $\hat{U}$ operators are applied line-wise from the top left to the bottom right. In (4.20) we have left out the swap operations, but each line can be implemented according to equation (4.11).

Also in the MPS framework, each line in (4.20), containing $a-1$ elements can be realised, using only the application of next-neighbour gates and swap-operations according to equation (4.11):

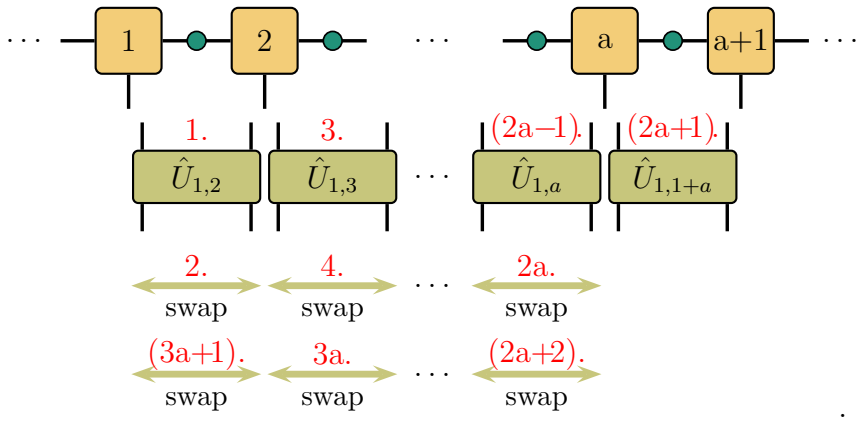

(4.21)

First, the next-neighbour evolution operator acts between site 1 and 2 is applied, followed by an interchange of those indices. In the third step, the long-range evolution operator $\hat{U}_{1,3}$ is applied to sites 2 and 3, which are effectively 1 and 3 due to the previous interchange. The index-swap followed by the application of a long-range gate is repeated for increasing site index,

until the gate $\hat{U}_{1,1+a}$ is applied. The index of site 1 can now be seen as being located at site a. In the final steps (2a+2) to (3a+1), it is swapped back to its original position.

For this specific line $3a + 1$ swap-gate and next-neighbour evolution-operator applications are required, each requiring $\mathcal{O}(\chi^3 d^3)$ basic operations. Thus, for a full sweep $\hat{P}_{\Delta t'}$ through all two-site evolution operators, according to (4.20), the number of required gates is found by summing the contributions of all lines to

$$G \equiv [m(3l + 1) + 3((l - 1)l/2) + l]. \tag{4.22}$$

The case of the transposed sweep $\hat{P}^T_{\Delta t}$ is performed analogous with the only difference, that for every line in (4.20), the order of the operations in scheme (4.21) is reversed.

Efficiency

In the case that the system size is large compared to the considered interaction length, ($N \gg l$), $G \approx N(3l + 1)$. Thus, compared to a single sweep in the standard TEBD algorithm, which requires $N - 1$ gate-applications (Equation (2.42)), adding long-range interactions over a maximum of l sites results in an overhead of only $\mathcal{O}(l)$ gates. If the interaction length is of $\mathcal{O}(N)$ in a large system, $l \approx N \gg 1$, $G \approx (N - 1)N/2 + 2N$. Thus, for the case of long-range interactions, the simulation time overhead is of $\mathcal{O}(N)$.

This also holds for the full evolution step, since the number of sweeps required for the Suzuki-Trotter decomposition remains the same in both, the TEBD and the lTEBD algorithm. Furthermore in both cases, all gates are limited by the Schmidt-decomposition step ($\mathcal{O}(\chi^3 d^3)$).

In conclusion, simulating an evolution step of a large N-site quantum systems with the lTEBD algorithm, including long-range interactions over l sites results in an computational overhead of $\mathcal{O}(l)$ basic operations compared to the next-neighbour TEBD algorithm ($\mathcal{O}(lN\chi^3 d^3)$ compared to $\mathcal{O}(N\chi^3 d^3)$).

Orthogonality Problems & Numerical Improvements

The solution to problems concerning the corruption of an initially canonical MPS during imaginary time evolution, and numerical tricks, discussed in section 2.1.4 for the TEBD algorithm can be largely transferred to lTEBD.

Note that if every line of the long-range sweep $\hat{P}_{\Delta t'}$ in equation (4.20) is implemented by the scheme (4.21), all consecutive two-site gates in $\hat{P}_{\Delta t'}$ are affecting a position in the MPS that is located one site to the left, one site to the right or at the preceding gate position. Thus, according to the

reasoning, following (2.50), at any stage any two-site gate is affecting only sites, represented in an orthogonal Schmidt basis. This also holds for all gates in $\hat{P}_{\Delta t'}\hat{P}^T_{\Delta t'}$ and $\hat{P}^T_{\Delta t'}\hat{P}_{\Delta t'}$. However, by performing the full Suzuki-Trotter expansion (4.19), situations occur where $\hat{P}_{\Delta t'}$ is followed by $\hat{P}_{\Delta t'}$ or $\hat{P}^T_{\Delta t'}$ by $\hat{P}^T_{\Delta t'}$. Since at the end of the sweep $\hat{P}_{\Delta t'}$, the situation of the MPS can be visualised via

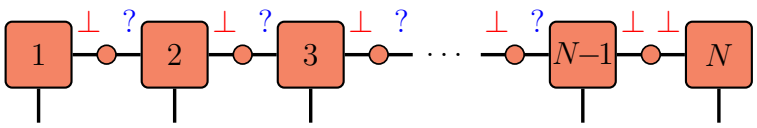

. (4.23)

or after the application of $\hat{P}^T_{\Delta t'}$ via

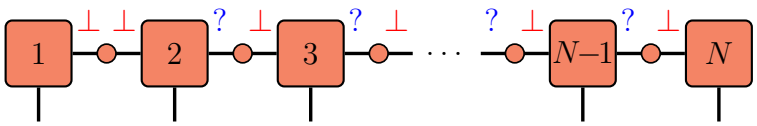

. (4.24)

respectively, we can cure this situation as we did in section 2.1.3 by inserting identity sweeps,

$$\hat{P}^T_{\mathrm{id}} \equiv \mathbb{1}_{2,3}\mathbb{1}_{3,4}\mathbb{1}_{4,5}\ldots\mathbb{1}_{N-2,N-1}, \tag{4.25}$$

changing $\hat{P}_{\Delta t'}\hat{P}_{\Delta t'}$ to $\hat{P}_{\Delta t'}\hat{P}^T_{\mathrm{id}}\hat{P}_{\Delta t'}$ and $\hat{P}^T_{\Delta t'}\hat{P}^T_{\Delta t'}$ to $\hat{P}^T_{\Delta t'}\hat{P}_{\mathrm{id}}\hat{P}^T_{\Delta t'}$. Then, the full long-range Suzuki Trotter expansion (4.19) has to be modified by adding 6 identity sweeps containing $(N-3)$ identity gates each,

$$\begin{aligned}\hat{U}^{\mathrm{imag}}_{\mathrm{LR}} = {} & \hat{P}^T_1\hat{P}_1\hat{P}^T_1\hat{P}_{-2}\hat{P}^T_1\hat{P}_{\mathrm{id}}\hat{P}^T_1\hat{P}_{\mathrm{id}}\hat{P}^T_1\hat{P}_{\mathrm{id}}\hat{P}^T_1\hat{P}_1\ldots \\ & \ldots\hat{P}^T_1\hat{P}_1\hat{P}^T_{\mathrm{id}}\hat{P}_1\hat{P}^T_{\mathrm{id}}\hat{P}_1\hat{P}^T_{\mathrm{id}}\hat{P}_1\hat{P}^T_{-2}\hat{P}_1\hat{P}^T_1\hat{P}_1 + \mathcal{O}(\Delta t^5).\end{aligned} \tag{4.26}$$

Note that analogous to the TEBD algorithm, also here a preceding identity sweep to restore a canonical MPS is necessary before expectation values are computed.

Application to the Dynamics of Rydberg Excitations in 1D Lattices

The lTEBD algorithm presented in this section will be extensively used in chapter 5 where we are going to simulate a system of Rydberg atoms excited in an optical lattice potential.

4.2 Long Range iTEBD (ilTEBD)

Finally, in the last section of Chapter 4, we are going to extend the infinite TEBD algorithm, presented in Section 2.1 to work with long-range interactions and will abbreviate its name as ilTEBD algorithm.

4.2.1 State Representation

For the iTEBD algorithm, the next-neighbour gates break the translation symmetry down to shifts over two sites. Therefore, an iMPS representation consisting of at least two Γ- and two λ-arrays was required to simulate the evolution of a next-neighbour Hamiltonian (Section 2.2.1). Now, we are going to execute long-range gates $\hat{U}_{s_1,s_2}$, which act between sites s_1 and s_2 with distance $\Delta s \equiv s_2 - s_1$. Since we are not able to implement gates of arbitrary large distance, we have to set an upper bound l. The number of Γ- and λ-arrays at least required in the iMPS representation is then given by $2l$. This is the case, because a $(l+1)$-site long-range gate breaks the symmetry down to shifts of $2l$. All these gates have to act in the same way to the left and to the right site, i.e. $\hat{U}_{(i,i+l)}$ must act on the same sites like $\hat{U}_{i-l,i}$. This can only by fulfilled if $(i+l)-(i-l) = 2l$ such sites are present. Consider for example the case $l = 2$,

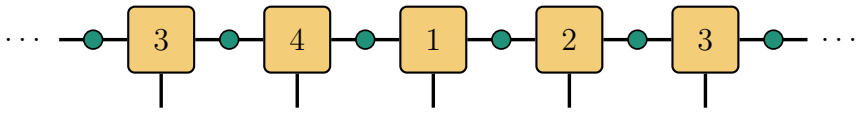

. (4.27)

$\hat{U}_{1,3}$ acts on the same sites, like $\hat{U}_{3,1}$. If only 3 sites would be utilised, the 3-site-gate starting at site 1 that acts to the right would access sites 1 and 3, whereas the gate that acts to the left would hit 2 and 3!

Note that again, an arbitrary number of Γ- and λ-arrays can be supplemented to produce an iMPS with more than $2l$ sites. This could only lead to ambiguities if gates act over more than l sites would be taken into account.

4.2.2 The Algorithm

We proceed like in the previous section. The system Hamiltonian can be decomposed into two-site terms $\hat{H}_{\mathrm{LR,inf}} = \sum_j^\infty \sum_k^l \hat{H}_{j,j+k}$. Both single two-site operations, swap gates and evolution gates $\hat{U}_{j_1,j_2} \equiv e^{-i\hat{H}_{j_2,j_2}\Delta t'}$ are implemented using steps (2.35) and (2.37). They are sorted within sweeps $\hat{P}_{\Delta t'}$ in

a 4th order Suzuki-Trotter expansion. We use

$$\hat{U}_{\mathrm{LR,inf}}(\Delta t) = \hat{P}_1^T \hat{P}_1 \hat{P}_1^T \hat{P}_{-2} \hat{P}_1^T \hat{P}_1^T \hat{P}_1^T \hat{P}_1^T \hat{P}_1 \hat{P}_1^T \hat{P}_1 \hat{P}_1 \hat{P}_1 \hat{P}_1 \hat{P}_{-2}^T \hat{P}_1 \hat{P}_1^T \hat{P}_1 + \mathcal{O}(\Delta t^5), \tag{4.28}$$

to simulate the full time evolution operator $\hat{U}_{\mathrm{LR,inf}}(\Delta t) \equiv e^{-i\hat{H}_{\mathrm{LR,inf}}\Delta t}$ in an infinite system with long-range interactions.

ilTEBD Sweeps

Thus, we only have to find a practical implementation for $\hat{P}_{\Delta t'}$, containing all required next-neighbour gates. Therefore, we decompose the $2l$-site iMPS into parts A and B,

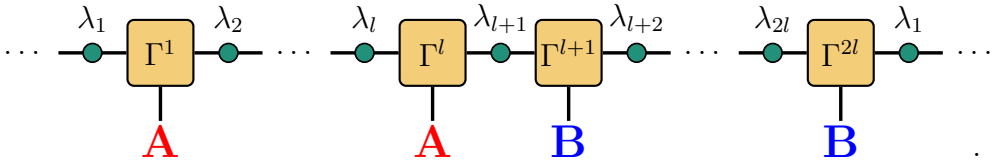

(4.29)

We then split up a single sweep into two parts, denoted $\widehat{AB}$ and $\widehat{BA}$ with

$$\widehat{AB}^T \equiv \begin{matrix} \hat{U}_{1,2} & \hat{U}_{1,3} & \hat{U}_{1,4} & \dots & \hat{U}_{1,1+l} \\ \hat{U}_{2,3} & \hat{U}_{2,4} & \hat{U}_{2,5} & \dots & \hat{U}_{2,2+l} \\ \vdots & \vdots & \vdots & & \vdots \\ \hat{U}_{l,l+1} & \hat{U}_{l,l+2} & \hat{U}_{l,l+3} & \dots & \hat{U}_{l,2l} \end{matrix} \tag{4.30}$$

and

$$\widehat{BA}^T \equiv \begin{matrix} \hat{U}_{l+1,l+2} & \hat{U}_{l+1,l+3} & \hat{U}_{l+1,l+4} & \dots & \hat{U}_{l+1,1} \\ \hat{U}_{l+2,l+3} & \hat{U}_{l+2,l+4} & \dots & \hat{U}_{l+2,1} & \hat{U}_{l+2,2} \\ \vdots & \vdots & & & \vdots \\ \hat{U}_{2l,1} & \hat{U}_{2l,2} & \hat{U}_{2l,3} & \dots & \hat{U}_{2l,l} \end{matrix} \tag{4.31}$$

and define a sweep as

$$\hat{P}_{\Delta t'}^T = \widehat{AB}^T \, \widehat{BA}^T. \tag{4.32}$$

This is similar to the iTEBD algorithm, i.e. equation (2.70).

For each row in (4.30) and (4.31), we can utilise the implementation scheme, introduced for the finite lTEBD algorithm in (4.21). In practice, therefore we additionally store l Γ- and λ-arrays to the right of the memory block B, to which we transfer the updated block memory A after an application of $\widehat{AB}^{(T)}$ and vice versa after an application of $\widehat{BA}^{(T)}$.

Since every row in (4.30) and (4.31) consists of l elements, $3l+1$ two-site evolution- and swap-gates are required. In total, for a full time-step simulation we have to apply $18 \times 2l \times (3l+1)$ gates, each implemented with $\mathcal{O}(\chi^3 d^3)$ basic operations. Hence, the overall complexity for a single time-step is $\mathcal{O}(l^2\chi^3 d^3)$. Note that compared to the next-neighbour iTEBD case, this is an overhead of $\mathcal{O}(l^2)$ operations when considering interactions over l sites. It can be understood by the fact that on the one hand we require $\mathcal{O}(l)$ operations for the long-range gate implementations and on the other hand we have to use a representation containing $\mathcal{O}(l)$ sites to capture the homogeneous infinite system state.

Orthogonality Problems

The orthogonality problems can be faced in a very similar manner as for the l-site iTEBD algorithm in section 2.2. We are going to use the Suzuki-Trotter implementation from equation (4.28), but will make identity gate amendments to the sweep $\hat{P}^T_{\Delta t'}$. However, in the ilTEBD case we are going to extend the sweep on the level of the row implementations of $\widehat{AB}$ and $\widehat{BA}$, namely in (4.21). Therefore, we again have to separately define extensions for the original and the transposed sweep, which are therefore not related by the transposition operation anymore. Utilising our Diagrammatic notation as guide, we obtain the following situation after the first non-unitary gate application within the first row implementation scheme (4.21) in $\hat{P}_{\Delta t'}$ (initially fully canonical iMPS),

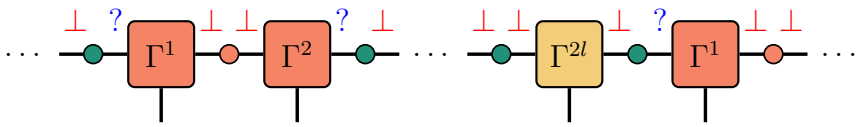

. (4.33)

For the transposed case in $\hat{P}^T_{\Delta t'}$,

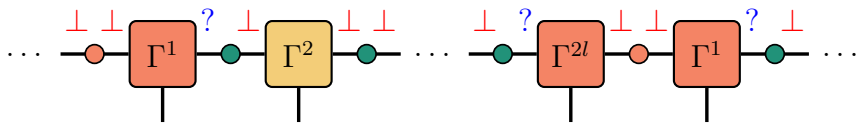

. (4.34)

The only Schmidt basis corrupted in this step and leading to problems in the remaining implementation of $\hat{P}_{\Delta t'}$ will be the set to the right of the bond between $2l$ and 1. In the transposed case, the basis to the left of the bond between sites 1 and 2 will cause problems. In general, considering the bond to the left (right, in the transposed case) of the site position where the actual row implementation (4.21) starts, the basis states to the right (left, in the transposed case) of that bond is causing non-orthogonality issues in the remaining sweep. Therefore, we can circumvent these problems by immediately restoring the orthogonality by inserting an identity gate, which acts on the two sites connected by this specific bond. Hence, we are going to proceed like for the redefinitions of the sweeps for the l-site iTEBD algorithm in equations (2.82) and (2.83), but will add identity operators after the first gate of a row implementation instead of the single gate applications $\hat{U}_{k,k+1}$ in (2.82) and (2.83). Specifically we redefine

$$P_{\Delta t'}^{\text{imag}} \equiv \begin{matrix} \mathbb{1}_{1,2} & & & & & \\ \hat{U}_{2l,l} & \dots & \hat{U}_{2l,3} & \hat{U}_{2l,2} & \mathbb{1}_{2l-1,2l} & \hat{U}_{2l,1} \\ \vdots & & \vdots & \vdots & \vdots & \vdots \\ \hat{U}_{2,2+l} & \dots & \hat{U}_{2,5} & \hat{U}_{2,4} & \mathbb{1}_{1,2} & \hat{U}_{2,3} \\ \hat{U}_{1,1+l} & \dots & \hat{U}_{1,4} & \hat{U}_{1,3} & \mathbb{1}_{2l,1} & \hat{U}_{1,2} \end{matrix} \tag{4.35}$$

and

$$P_{\Delta t'}^{\text{imag,transp}} \equiv \begin{matrix} \mathbb{1}_{2l,1} & & & & & \\ \hat{U}_{1,2} & \dots & \hat{U}_{1,l-1} & \hat{U}_{1,l} & \mathbb{1}_{2,3} & \hat{U}_{1,1+l} \\ \vdots & & \vdots & \vdots & \vdots & \vdots \\ \hat{U}_{2l-1,2l} & \dots & \hat{U}_{2l-1,l-3} & \hat{U}_{2l-1,l-2} & \mathbb{1}_{2l,1} & \hat{U}_{2l-1,l-1} \\ \hat{U}_{2l,1} & \dots & \hat{U}_{2l,l-2} & \hat{U}_{2l,l-1} & \mathbb{1}_{1,2} & \hat{U}_{2l,l} \end{matrix} , \tag{4.36}$$

which guarantees orthogonal Schmidt bases during the whole time-evolution process, if inserted into (4.28). Note that in practice, partial updates of

the auxiliary memory blocks mentioned above have to take place at earlier stages and not only after the application of $\widehat{AB}^{(T)}$ and $\widehat{BA}^{(T)}$. By utilising this scheme, in total $18 \times (2l+1) \times \mathcal{O}(\chi^3 d^3)$ basic operations are added and the total complexity of $\mathcal{O}(l^2\chi^3 d^3)$ is not affected.

4.2.3 A Test System: Haldane-Shastry Model

To test our ilTEBD algorithm we are going to perform ground state calculations by imaginary time evolution of the Haldane-Shastry spin model, which is a Heisenberg chain model with interactions decaying like $1/r^2$ and has been solved exactly in [7, 8]. The model Hamiltonian for an infinite system takes the form

$$\hat{H} = \frac{1}{2} \sum_n \sum_m \frac{J_0}{m^2} \, \hat{\vec{\sigma}}_n \cdot \hat{\vec{\sigma}}_{n+m}, \tag{4.37}$$

with the Pauli spin opertors $\hat{\vec{\sigma}}^T \equiv (\hat{\sigma}_x, \hat{\sigma}_y, \hat{\sigma}_z)$, and can thus be easily implemented into the ilTEBD algorithm. The spin-spin correlation of the ground state has been calculated analytically ($J_0 \equiv 1$),

$$\langle \hat{\sigma}_0^z \hat{\sigma}_k^z \rangle = (-1)^k \frac{\mathrm{Si}(\pi k)}{\pi k} \tag{4.38}$$

with

$$\mathrm{Si}(x) \equiv \int_0^x dt \, \frac{\sin(\pi t)}{\pi t}. \tag{4.39}$$

In figure 4.1, we plot $|\langle \hat{\sigma}_0^z \hat{\sigma}_k^z \rangle|$ from equation (4.38) compared to numerical results, obtained from imaginary time evolution within our ilTEBD algorithm for increasingly large values of the Hilbert space truncation parameter $\chi = 30, 50, 70$ and an interaction length of $l = 12$.

We find good convergence for $\chi = 70$ in the values of the correlations over approximately 50 sites (differences of less than 3% to $\chi = 50$ results). However, our results, even if they are converged in χ, turn out to be not very satisfactory. We find a very slow convergence for increasing values of the interaction length l. Therefore, in figure 4.2 we compare the exact density-density correlation to calculations with $l = 6, 8, 10, 12$ at $\chi = 70$.

We find that the relatively large difference that is visible already after approximately 10 sites, can be reduced only slowly with increasingly large interaction length values l. We conclude that our ilTEBD algorithm is in practice only applicable if we restrict ourselves to models with interactions decaying articulately faster than $1/r^2$. This is simply a practical issue due

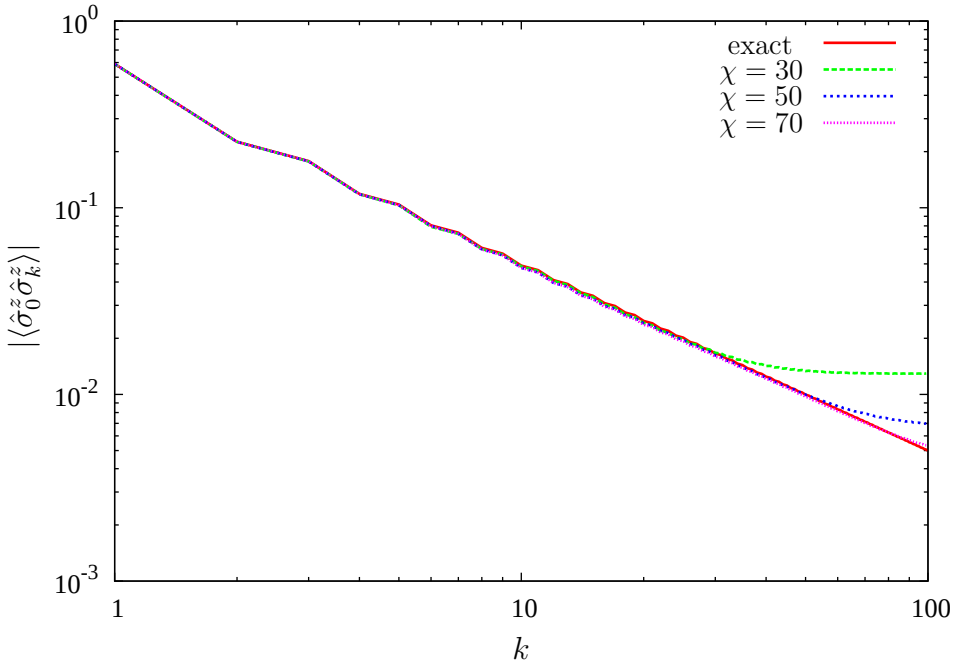

Figure 4.1: Comparison of the exact solution of the ground state spin-spin correlation for the infinite 1D Haldane-Shastry model (4.37) with numerical ilTEBD results. Shown are results for Hilbert space truncation parameters $\chi = 30, 50, 70$. Interactions over $l = 12$ sites are considered.

to the l^2 scaling of the required computational time. As an example, on the hardware we are using[1], 100 imaginary time-steps with a truncation parameter of $\chi = 70$ required approximately 3.0 h in case of an interaction length of $l = 6$ and approximately 11.5 h in the case of $l = 12$. In general, several 1000 steps are required for a fully converged ground state obtained from an imaginary time evolution!

4.2.4 Outlook on Matrix Product Operators

The simulation of infinite 1D systems with interactions over larger distances than neighbouring sites is not fully satisfactorily achieved within the ilTEBD algorithm. For slowly decaying long-range interactions, a many site infinite MPS representation has to be employed, which renders the algorithm extremely time consuming.

Recently, progress has been achieved in simulating infinite systems with long-range interactions, in particular by introducing matrix product opera-

[1]Intel Xeon 5345 (2.33 GHz) CPU, 8 GB RAM, GNU C-Compiler 4.1.2

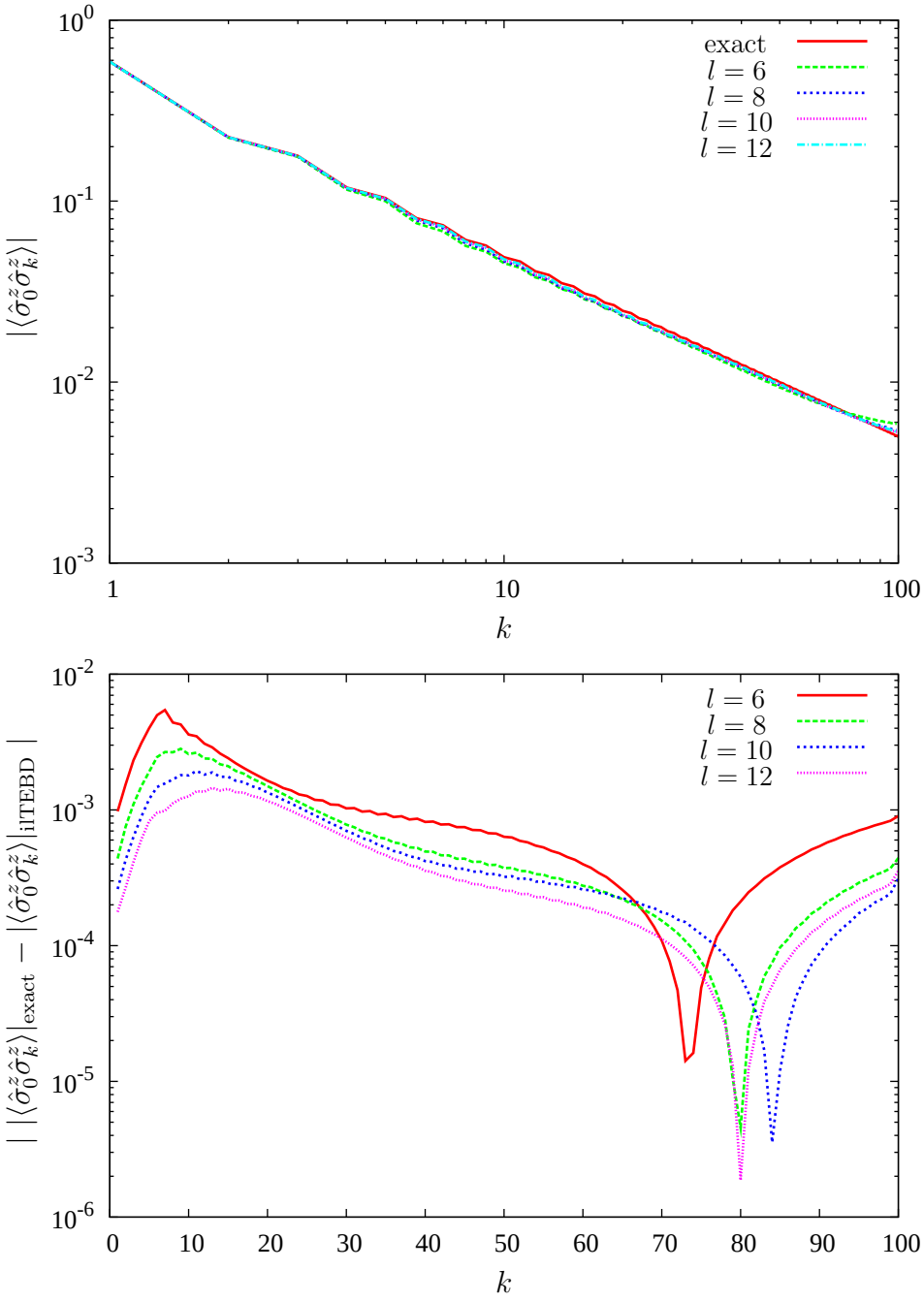

Figure 4.2: Comparison of the exact solution of the ground state spin-spin correlation for the infinite 1D Haldane-Shastry model (4.37) with numerical ilTEBD results. The lower picture shows the absolute differences to the exact results. Shown are calculations for interaction length truncations of $l = 6, 8, 10, 12$.

tors (MPO). The conceptual idea is to also find a matrix product representation of the full evolution operator itself, thereby avoiding that translational invariance is broken. In the case of a finite N-site evolution operator $\hat{U}$, this might be visualised as

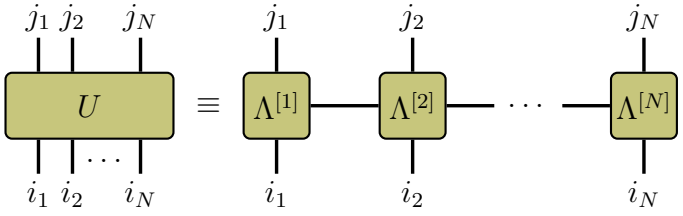

. (4.40)

A MPO can be applied to a MPS much more efficiently than two-site gates in the TEBD algorithm and furthermore no multi-site iMPS representations are required. First schemes how to construct a MPO are presented in [3–6] and results seem to be very promising. Ground state calculations on the Haldane-Shastry model (Equation (4.37) in Section 4.2) have for example been performed in [4] with striking success. There, in contrast to the results in figures 4.1 and 4.2, faithful reproduction of the spin-spin correlation could be achieved over more than 1000 sites. It will be interesting to see which future accomplishments are possible using this algorithm.

Bibliography

[1] Guifré Vidal. *Phys. Rev. Lett.* **91**, 147902 (2003).

[2] Y.-Y. Shi, L.-M. Duan, and G. Vidal. *Phys. Rev. A* **74**, 022320 (2006).

[3] I. P. McCulloch. *J. Stat. Mech.* **2007**, P10014 (2007).

[4] G. M. Crosswhite, A. C. Doherty, and G. Vidal. *Phys. Rev. B* **78**, 035116 (2008).

[5] I. P. McCulloch. *arXiv: 0804.2509* (2008).

[6] V. Murg, J. I. Cirac, B. Pirvu, and F. Verstraete. *arXiv: 0804.3976* (2008).

[7] B. S. Shastry. *Phys. Rev. Lett.* **60**, 639 (1988).

[8] F. D. M. Haldane. *Phys. Rev. Lett.* **60**, 635 (1988).

Chapter 5

Dynamics of Rydberg Excitations in 1D Lattices

Rydberg atoms are characterised by electronic excitations to states of high principal quantum number $n \gtrsim 10$ and have exaggerated properties [1]. The large distance of the valence electron from the ionic core leads to a valid description by the hydrogen atom model and is responsible for extraordinary interaction properties. Despite their high excitation number, single Rydberg atoms can have long lifetimes up to the order of milliseconds and because of their strong interactions, Rydberg excitations in cold atomic gases have become interesting for applications in quantum computation and quantum simulation over the last ten years.

The classical radius of a Rydberg atom is proportional to $n^2 a_0$ with the Bohr radius a_0, and due to their large size they are strongly polarisable. An ensemble of Rydberg atoms is therefore exposed to strong van der Waals interactions. Furthermore, excitations can possess large electric dipole-moments making them also strongly interact over long ranges by this means. Both van der Waals and dipolar interactions lead to the interesting effect of excitation blockade. If a laser is tuned to a Rydberg transition, the shifts in the energy levels out of resonance, which are induced by the interactions, prohibit further excitations in the vicinity of other Rydberg atoms.

In recent times, various proposals triggered a lot of interest in both theoretical and experimental work. This included propositions to utilise this dipole blockade effect for fast quantum gates between two neutral atoms by D. Jaksch et al. [2] or for information stored in collective states of a mesoscopic ensemble by M.D. Lukin et al. [3]. This excitation suppression has recently been demonstrated in several experiments (e.g. [4,5]) and important steps towards implementations of quantum gates using this blockade mechanism have been lately achieved (e.g. for two individual neutral atoms [6]).

Besides that, also numerical studies were performed using simulation techniques of many body Rydberg systems, which make use of a reduced Hilbert space due to a perfect blockade effect [7, 8]. In these studies, mean numbers of excitations and correlation functions emerging during time evolution have been evaluated. It was shown that quantum correlations play a crucial role and mean-field approaches are inappropriate.

We are going to numerically study a system of atoms loaded into a 1D optical lattice potential with a laser tuned to a Rydberg transition. Full dipolar long-range interactions are taken into account and we are going to use the finite lTEBD algorithm (Section 4.1). In this way, quantum correlations will be fully included within our simulations.

We will first describe the theoretical background of Rydberg excitations and outline the blockade mechanism (Section 5.1). We introduce an effective Hamiltonian of a system with atoms loaded into an optical lattice potential and a laser tuned to a Rydberg transition. We then analyse the time evolution of the system and the resulting state when we instantaneously switch on the laser (Section 5.2). We continue with ground state calculations and find several phases indicated by distinct density-density correlations. Afterwards, we analyse a way to drive the system adiabatically from an initial "vacuum" state with no excitations present in the lattice as close as possible to an "anti-ferromagnetic like" ground state. This can be achieved by sufficiently slow changes of the laser intensity and the detuning along a properly chosen adiabatic path.

5.1 Background Overview

In this section we introduce the model Hamiltonian, describing a system of Rydberg atoms in a 1D lattice. This model includes the creation of Rydberg excitations from atoms in each lattice well, in addition to long-range dipole-dipole interactions.

5.1.1 The Hamiltonian

We start from a system with a large number N of homogeneously distributed non-interacting atoms loaded into a 1D periodic optical lattice potential of the form $V_L \equiv V_0 \sin^2(k_l x)$ with wavenumber $k_l \equiv 2\pi/\lambda$ and a lattice constant of $a \equiv \pi/k_l$. We consider a lattice with M sites and an external laser tuned to an internal transition of the atoms to a Rydberg state, detuned by an energy of δ. Neglecting interactions between the Rydberg atoms for the moment, this leads to a model Hamiltonian of the form ($\hbar \equiv 1$)

$$\hat{H}_0 \equiv \Omega_L \sum_j^M \left(\hat{a}_j^\dagger \hat{r}_j + \hat{a}_j \hat{r}_j^\dagger\right) + \delta \sum_j^M \hat{r}_j^\dagger \hat{r}_j, \tag{5.1}$$

where $\hat{a}_j^\dagger$ ($\hat{a}_j$) denote the bosonic creation (annihilation) operators of the atoms and $\hat{r}_j^\dagger$ ($\hat{r}_j$) the creation (annihilation) operators for Rydberg excitations at site j. Ω_L is the Rabi frequency. Assuming that the number of atoms per lattice site $N/M \gg 1$ and for all j, $\langle \hat{a}_j^\dagger \hat{a}_j \rangle \approx N/M$, we can neglect the commutation relations of the atoms, which are only of the order of one and replace for all j, $\hat{a}_j \approx \hat{a}_j^\dagger \approx \sqrt{N/M}$. The approximated Hamiltonian (5.1) can then be written as

$$\begin{aligned}\hat{H}_0 &= \Omega_L \sqrt{\frac{N}{M}} \sum_j^M \left(\hat{r}_j + \hat{r}_j^\dagger\right) + \delta \sum_j^M \hat{r}_j^\dagger \hat{r}_j \\ &\equiv \Omega \sum_j^M \left(\hat{r}_j + \hat{r}_j^\dagger\right) + \delta \sum_j^M \hat{n}_j,\end{aligned} \tag{5.2}$$

where in the second line the effective Rabi frequency $\Omega \equiv \Omega_L \sqrt{N/M}$ and the Rydberg particle number operator $\hat{n}_j \equiv \hat{r}_j^\dagger \hat{r}_j$ have been defined.

Dipole Blockade Mechanism

We are now going to include interactions between the Rydberg atoms. To obtain an organised dipole-dipole interaction we assume a constant electric field set up along the z axis, perpendicular to our lattice dimension and aligning existing dipoles parallel to $\vec{e}_z$. Following [1], we can calculate the electric dipole moment of the Rydberg state (SI units)

$$\mu \equiv e\langle z \rangle = \frac{3}{2} e a_0 (n_1 - n_2) n, \tag{5.3}$$

where e denotes the elementary charge, a_0 the Bohr radius, n the effective principal quantum number and n_1,$n_2 \geq 0$ are the parabolic quantum numbers. Those are implicitly related to the magnetic quantum number via

$$n = n_1 + n_2 + |m| + 1. \tag{5.4}$$

We are going to consider only non-circular states, implicating a permanent dipole moment. Specifically, we assume the case of $|m| = 0$ and furthermore

the state with the maximum possible dipole moment, i.e. with $n_1 - n_2 = n-1$. Then,

$$\mu = \frac{3}{2} e a_0 n (n-1). \tag{5.5}$$

Thus, the dipole-dipole interaction energy between sites i and j with $|i-j| \equiv k > 0$ can be expressed as

$$\beta_k \equiv \frac{1}{4\pi\epsilon_0} \frac{\mu^2}{(ak)^3} \tag{5.6}$$

with permittivity ϵ_0. This interaction energy leads to a shift in the energy levels of the nearby atoms and therefore suppresses an excitation to the Rydberg state within some blockade distance $(ak)_b$. This distance can be estimated by comparing β_k with the linewidth of the excitation laser. For a linewidth Γ, ranging approximately between 0.1 – 10 MHz and by assuming a Rydberg excitation to $n = 20$ one can calculate that $(ak)_b \approx 27$ – 6 μm. In general, $(ak)_b \propto n^{4/3}$ and $(ak)_b \propto \Gamma^{-1/3}$. In experiments Γ is typically dominated by powerbroadening and therefore $\Gamma = \Omega_L$ [9]. For typical optical lattice wavelengths, $a \approx 500$ nm and the blockade distance translates to several tens of sites, i.e. we are considering a regime of strong blockade.

Naturally, Rydberg atoms are also exposed to van der Waals interactions. The leading term is $V_k^{\mathrm{vdW}} = -C_6/(ak)^6$ (for specific values of C_6 see [10]). In general $C_6 \propto n^{11}$, however for example in the case $n = 20$ for Rubidium, $C_6 \approx -7.5 \times 10^{14}$ in Hartree atomic units. Therefore, the van der Waals interaction energy between neighbouring sites is $|V_1^{\mathrm{vdW}}| \approx 40$ MHz. In contrast, the corresponding dipole-dipole interaction is $\beta_1 \approx 16$ GHz, which can be calculated utilising (5.6) with (5.5). Thus, we are going to neglect van der Waals interactions in our observations, but it is important to remember that they play a crucial role for extremely large n or for states without or small permanent electric dipole moments.

Writing the interactions (5.6) as part of our Hamiltonian leads to an interaction term

$$\hat{H}_{\mathrm{int}} = \sum_{j}^{M-1} \sum_{1 \le k \le M-j} \beta_k \hat{n}_j \hat{n}_{j+k} \tag{5.7}$$

in a finite system consisting of M sites. Thereby, we additionally leave out local dipole-dipole on-site interactions of the form

$$\beta_{\mathrm{on-site}} \equiv \frac{1}{4\pi\epsilon_0} \frac{\mu^2}{(\epsilon)^3} \tag{5.8}$$

with a site dimension of $\epsilon \ll a$. Instead, since $\beta_{\text{on-site}} \gg \beta_k$, we restrict ourselves to a local Hilbert space dimension of two and simply do not allow double or higher occupation. Note that due to this limitation of the local dimension to $d = 2$, the model is also valid for a fixed number of particles on each site, e.g. for a Mott insulator (Section 3.1).

Finally this leads us to the full model Hamiltonian residing in an M-site Hilbert space with local dimensions of $d = 2$, ($\hbar \equiv 1$)

$$\hat{H} = \Omega \sum_j^M \left(\hat{r}_j + \hat{r}_j^\dagger\right) + \sum_j^{M-1} \sum_{1 \le k \le M-j} \frac{\beta_0}{k^3} \hat{n}_j \hat{n}_{j+k} + \delta \sum_j^M \hat{n}_j, \tag{5.9}$$

where

$$\beta_0 \equiv \frac{1}{4\pi\epsilon_0} \frac{\mu^2}{(a)^3}. \tag{5.10}$$

Note that the third detuning term can also be interpreted as negative chemical potential $\mu \equiv -\delta$.

Equation (5.9) is an implementation of a spin 1/2 Hamiltonian with the identifications $|0\rangle_j = |\downarrow\rangle_j$, $|1\rangle_j = |\uparrow\rangle_j$, $\hat{\sigma}_j^x = \hat{r}_j + \hat{r}_j^\dagger$ and $\hat{\sigma}_j^z = 2(\hat{n}_j - 1/2)$. The Hamiltonian (5.9) can then be written as

$$\begin{aligned}\hat{H}_{\text{Spin}} = \Omega \sum_j^M \hat{\sigma}_j^x + \sum_j^{M-1} \sum_{1 \le k \le M-j} \left(\frac{\beta_0}{4k^3} \hat{\sigma}_j^z \hat{\sigma}_{j+k}^z + \frac{\beta_0}{2k^3} (\hat{\sigma}_j^z + \hat{\sigma}_{j+k}^z) \right) \\ + \frac{\delta}{2} \sum_j^M \hat{\sigma}_j^z,\end{aligned} \tag{5.11}$$

where constant terms have been dropped.

In practice, in our numerical simulations later in this chapter we will not take into account interactions over arbitrary many sites. Instead, we will in the second term of (5.9) and (5.11) restrict the k index to values $1 \le k \le l$ with a maximum interaction length l, thereby neglecting terms of $\mathcal{O}(\beta_0/l^3)$.

5.2 lTEBD Calculations

In this section we present our results from exact and numerical lTEBD (Section 4.1) simulations performed with the Hamiltonian (5.9).

We will first analyse the time evolution of the system if the excitation laser is switched on instantaneously with previously no Rydberg excitation present in the lattice, i.e. the system is in a "vacuum" state $|0\rangle$. This state is

the natural state to start in for an experimental realisation. We then perform ground state calculations for various values of the detuning δ and the dipolar interaction strength β_0 at fixed small effective Rabi frequency Ω. In general, it is a priori not clear how to experimentally prepare a ground state of the system, due to the absence of a dissipative process. We will therefore answer the question how close the system can be adiabatically driven to an antiferromagnetic like (on average one Rydberg excitation on every second site) ground state if we start in the state $|0\rangle$ and only vary Ω and δ at fixed β_0.

5.2.1 Excitation Dynamics

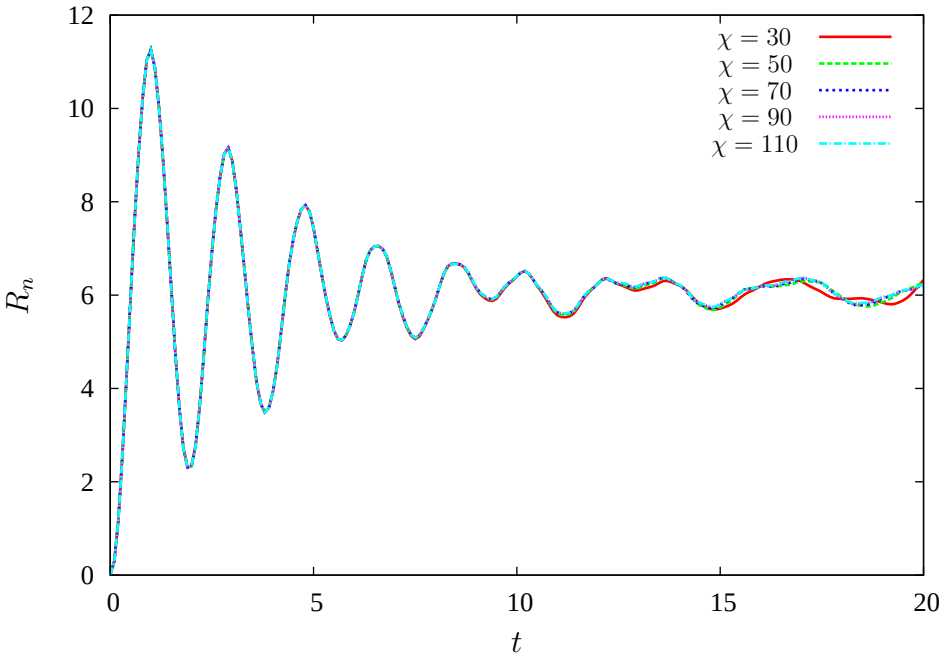

Figure 5.1: Rydberg excitation number as function of time, when simulating the Hamiltonian (5.9) with $\Omega = 1$, $\beta_0 = 10$ and $\delta = 0$ in a 30-site system. Initially the system is in a vacuum state $|0\rangle$. We show several increasing values of the Hilbert space truncation parameter χ. Interactions over a maximum of $l = 10$ sites are taken into account. $\Delta t = 0.1\ \Omega^{-1}$.

Initially, we employ the lTEBD algorithm to simulate the real time evolution of the total Rydberg excitation number $R_n \equiv \sum_i^N \langle \hat{n}_i \rangle$, after switching on the excitation laser at time $t = 0$ in a system of 30 sites initially in the state $|0\rangle$. The effective Rabi frequency is normalised to $\Omega = 1$, the interaction energy is chosen to be large with $\beta_0/\Omega = 10$ and the laser is exactly

tuned to a Rydberg transition, $\delta = 0$. To obtain valid results we have to check up to what time our results reproduce the real physical behaviour. Therefore, we have to find convergence for increasingly large values of our Hilbert space truncation parameter χ, which limits the entanglement allowed in the basis states during evolution. In figure 5.1 we plot time evolution up to $t = 20\ \Omega^{-1}$ for increasing values of $\chi = 30, 50, 70, 90, 110$ and find that the results with $\chi = 110$ reproduce the correct behaviour up to a time of approximately $t = 20\ \Omega^{-1}$.

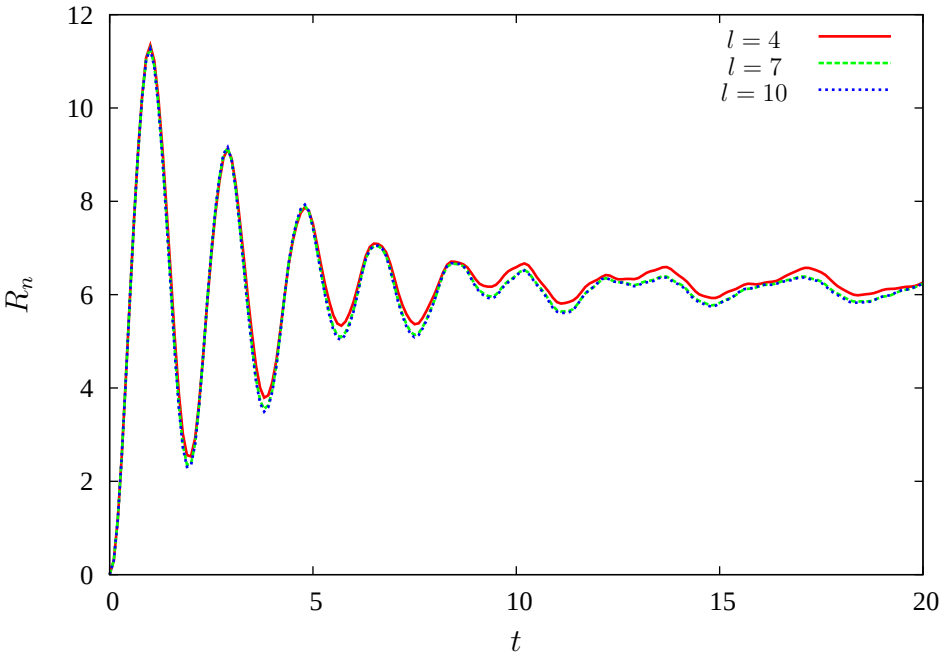

Figure 5.2: Rydberg excitation number as function of time, when simulating the Hamiltonian (5.9) with $\Omega = 1$, $\beta_0 = 10$ and $\delta = 0$ in a 30-site system. Initially the system is in a vacuum state $|0\rangle$. We show several increasing values of the considered interaction length l. $\chi = 110$, $\Delta t = 0.1\ \Omega^{-1}$.

We make the approximation of truncating dipolar interactions over more than l sites in the Hamiltonian (5.9). To see to what extent this changes our results, in figure 5.2 we show the same evolution as in figure 5.1 but with fixed $\chi = 110$ and increasing values of $l = 4, 7, 10$. We find small differences between the curves for $l = 4$ and $l = 7$, but the latter one nearly completely coincides with the results for $l = 10$. We conclude that the main physical behaviour is captured by the results with $l = 10$.

In figures 5.2 and 5.1 we observe a relaxation to a time averaged excitation number $\bar{R}_n$ of approximately 6. If we would only consider next-neighbour

interactions in a system with large β_0, we would expect excitations on average on every second site. Furthermore, due to a factor of 1/2 because of the two possible combinations of these second-site excitations, we would expect $\bar{R}_n \approx N/4$. Including long-range terms will in general lead to a decrease of this number due to blockades over more than neighbouring sites. Thus, $\bar{R}_n \approx 6$ in figures 5.2 and 5.1 is reasonable.

To verify the assumption of the excitation blockade, we can also analyse correlations in the site occupation within our system. Specifically we are going to evaluate the density-density correlation (DDC) at site i of the form

$$\mathcal{G}_k^{[i]} \equiv \frac{\langle \hat{n}_i \hat{n}_{i+k} \rangle}{\langle \hat{n}_i \rangle \langle \hat{n}_{i+k} \rangle}, \tag{5.12}$$

which is normalised to one if no correlations between the occupation numbers of sites i and $i+k$ are present.

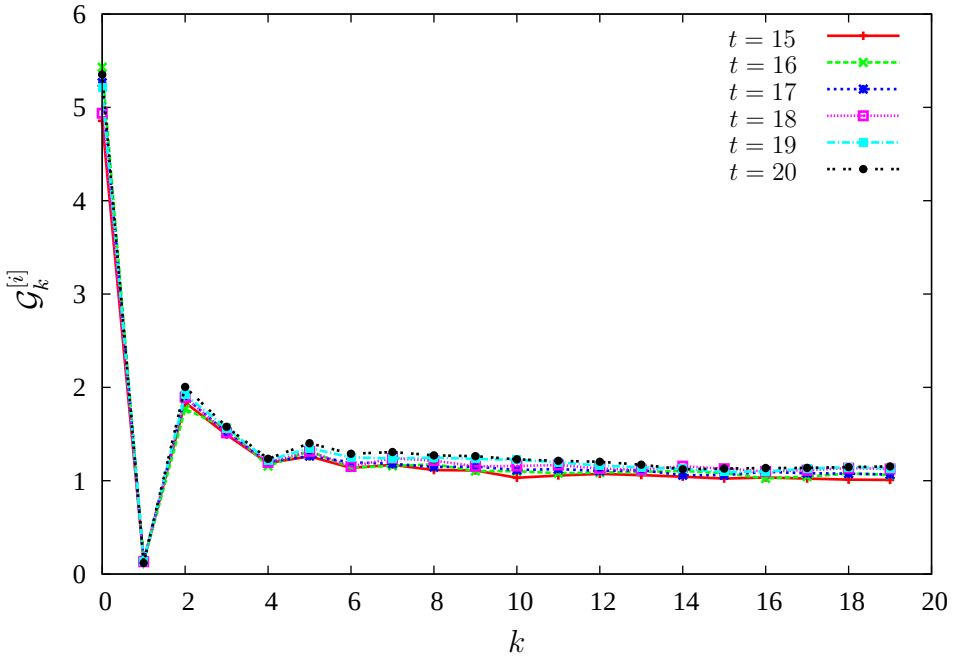

Figure 5.3: The density-density correlation evaluated from site 6 to 25 ($i = 6$), for times between $t = 15\ \Omega^{-1}$ and $t = 20\ \Omega^{-1}$ in the evolution process of figures 5.2, 5.1.

In figure 5.3 we plot the DDC for several time snapshots between the times 15 and 20, where the system has already relaxed to an average total excitation number. We find that also $\mathcal{G}_k^{[i]}$ is very similar at all this points in time, especially the behaviour over the first 5 sites is common to all curves.

We observe an almost perfect blockade for excitations on neighbouring sites, whereas the small peak at $k = 2$ indicates an increased probability for states with excitations on every second site. For large site differences, no correlations are visible.

It is also interesting, to not only observe the DDC, but also purely quantum mechanical correlations, i.e. entanglement, emerging during time-evolution. Due to our TEBD simulation technique, in each time step we can easily evaluate the von Neumann entropy S, since we already have a matrix product state representation expanded into Schmidt eigenbases $\{|\Phi_{\alpha_b}^{[b]L}\rangle\}$ and $\{|\Phi_{\alpha_b}^{[b]R}\rangle\}$ to the left and the right of a specific bipartite splitting (bond) b of the system (see section 2.1, equation (2.17)). The von Neumann entropy, a

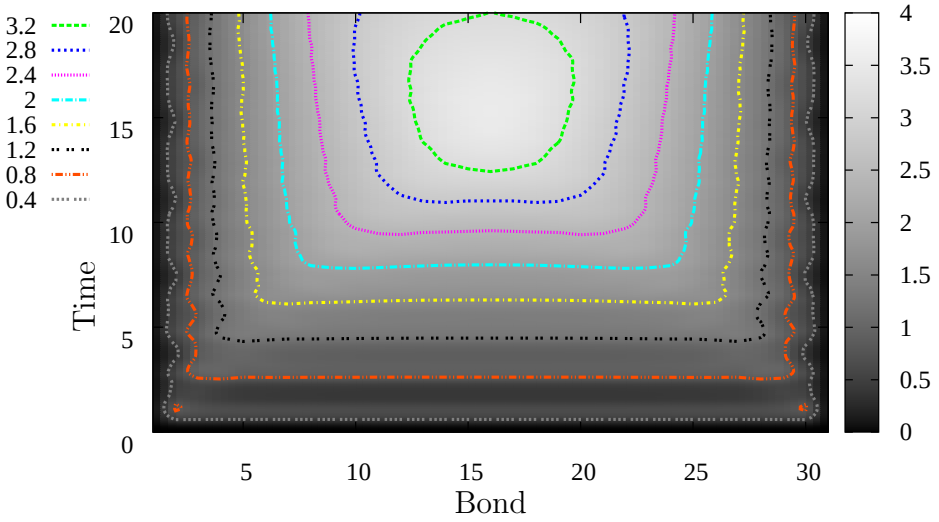

Figure 5.4: The von Neumann entropy as a function of time for all bipartite splittings (Bonds) in a system of 30 sites. The evolution is simulated under the Hamiltonian (5.9) with $\Omega = 1$, $\beta_0 = 10$ and $\delta = 0$. The initial state is $|0\rangle$. $\chi = 110$, $\Delta t = 0.1\ \Omega^{-1}$. The linies indicate contours of constant entropy.

measure for bipartite entanglement can therefore be immediately evaluated from equation (2.8) with the Schmidt coefficients $\lambda_{\alpha_b}^{[b]}$,

$$S = -\sum_{\alpha_b}^{\chi} \lambda_{\alpha_b}^{[b]2} \log_2(\lambda_{\alpha_b}^{[b]2}). \tag{5.13}$$

In figure 5.4 we plot the time evolution of the von Neumann entropy as a function of time and for each bond in the 30-site system. We find that in the centre of the system, entanglement continuously increases until a time of approximately $t = 15\ \Omega^{-1}$ and then saturates at a value of approximately $S = 3.5$. We thus conclude that entanglement plays a crucial role in an understanding of the state emerging from a sudden switch on of the laser and mean-field Gutzwiller treatments, which assume product state dynamics, are in general questionable for this system. Note that the maximum possible von Neumann entropy could occur in the centre of the 30-site system and would be $S_{\max} = 15$. With our truncation parameter we can in principle capture basis states with a maximum bipartite entanglement of $S_{\chi=110} = \log_2(110) \approx 6.78$.

5.2.2 Ground State Calculations

We calculate ground states for a 30-site Rydberg system introduced in section 5.1 with Hamiltonian (5.9), using evolution in imaginary time within our lTEBD algorithm.

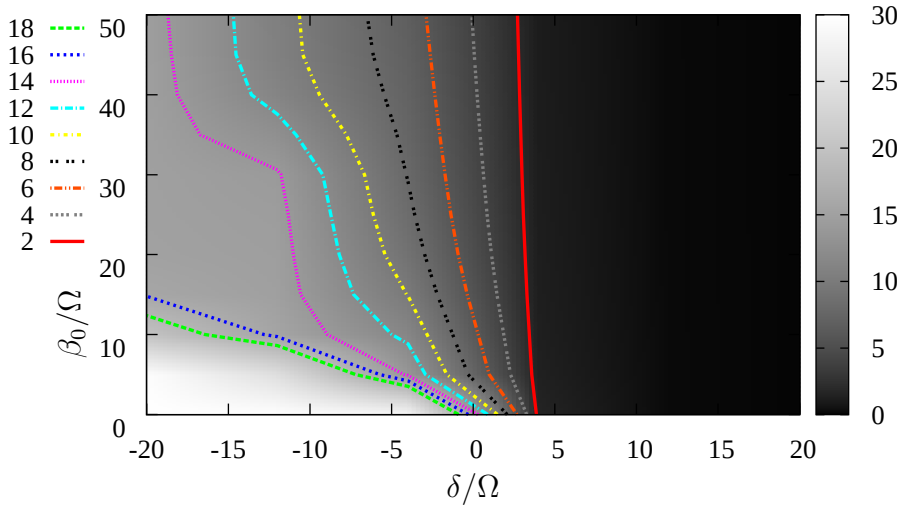

Figure 5.5: Rydberg excitation number of the ground states obtained from an imaginary lTEBD time evolution ($\chi = 30$) in a 30-site system with long-range interactions included over $l = 10$ sites. The system Hamiltonian is (5.9) with $\Omega = 0.1$. Shown are several values of detuning δ/Ω and interaction strength β_0/Ω. The lines indicate the contours of constant excitation number.

In figure 5.5, we start our investigation by plotting the total ground state Rydberg excitation number $R_n \equiv \sum_i^N \langle \hat{n}_i \rangle$ as a function of the detuning δ and the dipolar interaction strength β_0, both normalised by an effective Rabi frequency of $\Omega = 0.1$. We plot the results on a grid with $-20 \leq \delta/\Omega \leq 20$ and $0 \leq \beta_0/\Omega \leq 50$ with spacing $\Delta\delta/\Omega = 4$ and $\Delta\beta_0/\Omega = 5$.

Numerically we find convergence by considering an interaction length of 10 sites and it turns out that a small Hilbert space truncation parameter of $\chi = 30$ already suffices. The small χ value can be understood by the fact that Ω is small and therefore the Hamiltonian (5.9) is almost diagonal, i.e. very similar to a classical Ising model with additional long-range interactions. Thus, ground states will in general contain only little entanglement.

In figure 5.5, as one might expect, we find regions with no excitation present in the lattice for large positive detunings, i.e. negative chemical potentials at arbitrary interaction strengths β_0. In contrast, in regions with weak interactions and large negative detunings we find states with full occupation of all 30 lattice sites. A positive chemical potential leads to a reduction of the total energy when Rydberg excitations are added to the system and thus competes with the penalty of an increased interaction energy. For negative chemical potential, Rydberg atoms lead to an increased overall energy in addition to their interaction energy and are thus suppressed. Interesting behaviour arises when observing, for example, a line of constant detuning $\delta/\Omega = -12$ and increasing interactions from $\beta_0/\Omega = 0$ to $\beta_0/\Omega = 50$. In the case of $\beta_0/\Omega = 0$ and $\beta_0/\Omega = 5$, we find that almost all 30 sites are occupied. Following that, in the region of $10 \leq \beta_0/\Omega \leq 30$ we find that the excitation number almost remains fixed at a value of 15, whereas after some intermediate values it tends to a value around 10 for $\beta_0/\Omega = 45$ and $\beta_0/\Omega = 50$. Therefore, we conclude that Rydberg atoms in the states for $10 \leq \beta_0/\Omega \leq 30$ are on average excited on every second site, i.e. the ground state is "anti-ferromagnetic" like, and for $\beta_0/\Omega = 45$ and $\beta_0/\Omega = 50$ on every third site.

To verify this assumption we are plotting the density-density correlation $\mathcal{G}_k^{[i]} \equiv \langle \hat{n}_i \hat{n}_{i+k} \rangle / \langle \hat{n}_i \rangle \langle \hat{n}_{i+k} \rangle$ for the ground states along the $\delta/\Omega = -12$ line in figure 5.6. The evaluation is performed between sites number 11 and 30 to also observe the effect of the boundary. Indeed, we find that in the case of $\beta_0/\Omega = 0, 5$, the DDC remains flat at a value of 1. Suddenly, for $10 \leq \beta_0/\Omega \leq 30$ a marked correlation with peaks on every second site appears and after some random behaviour for $\beta_0/\Omega = 35, 40$, a correlation with peaks on every third site becomes visible for $\beta_0/\Omega = 45, 50$.

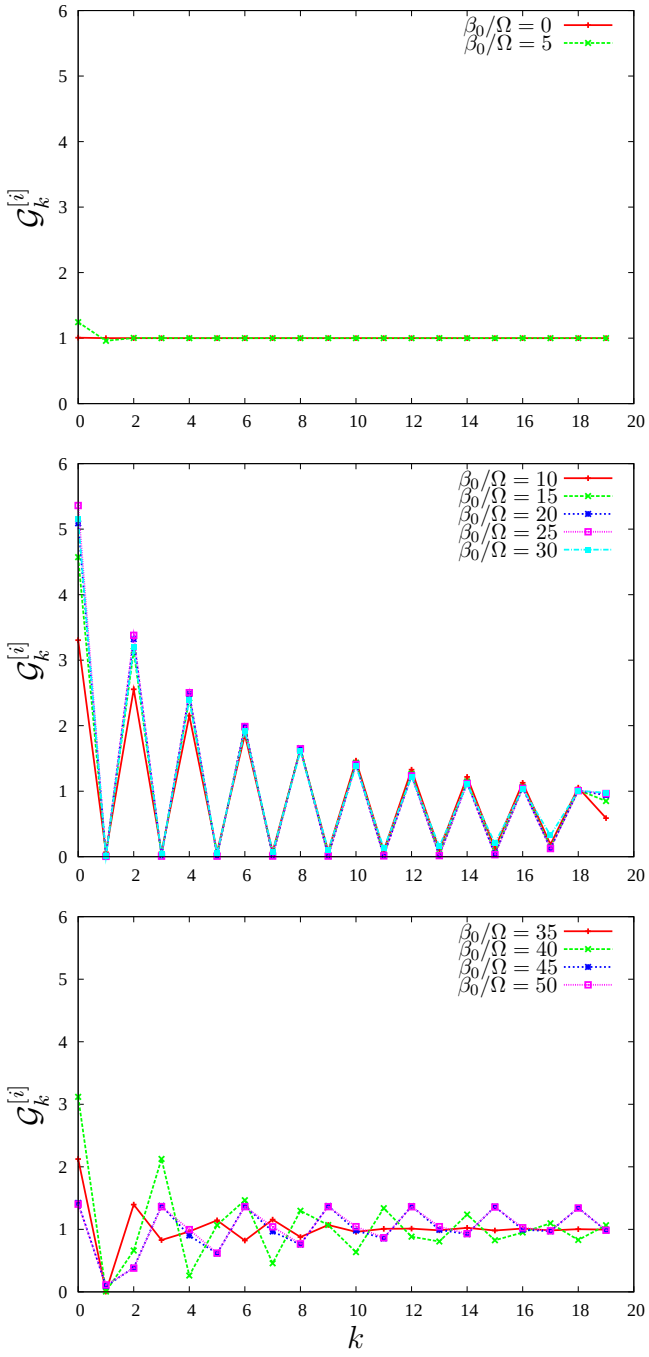

Figure 5.6: Ground state density-density correlations evaluated between sites 11 and 30 ($i = 11$) in a 30-site system with long-range interactions over $l = 10$ sites. The results are obtained from an imaginary lTEBD time evolution ($\chi = 30$). The system Hamiltonian is (5.9) with effective Rabi frequency $\Omega = 0.1$ and detuning $\delta/\Omega = -12$. Shown are results for several values of β_0/Ω.

5.2.3 Adiabatic Driving

It is an interesting question whether it is possible to reach an anti-ferromagnetic like phase with a DDC as in figure 5.6 for the region $10 \leq \beta_0/\Omega \leq 30$, by starting in a vacuum state $|0\rangle$ and adiabatically changing the laser parameters detuning δ and effective Rabi frequency Ω. We do not expect that this procedure works in the limit of an infinite system, since we encounter a disappearing energy gap ΔE between the ground and the first excited state in this case. However, since we are dealing with a finite system, we are going to analyse to which extent we can reach a state with a DDC close to the one shown in figure 5.6 when changing the parameters sufficiently slow.

Exact Simulations for an 8-Site System

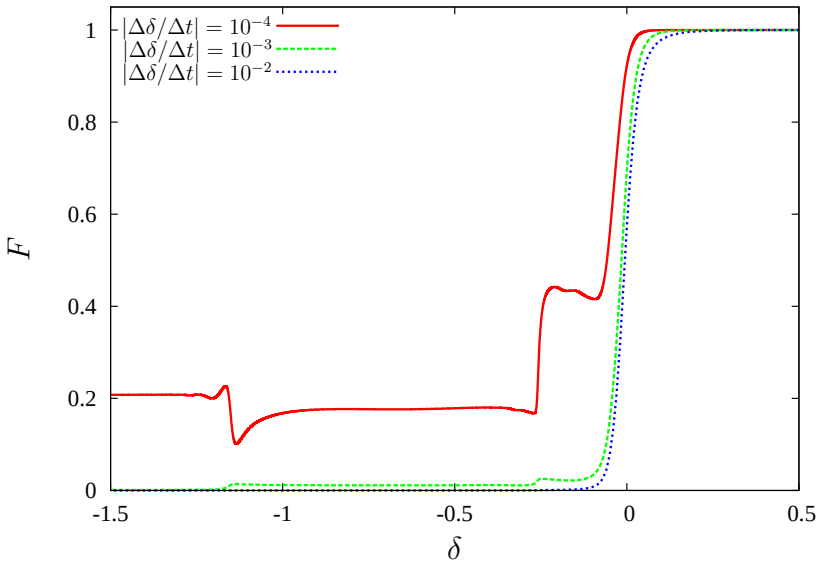

Figure 5.7: The overlap (fidelity) of the system state with the ground state at given points, when driving δ from 0.5 to -1.5 at constant $\Omega = 0.01$. The results are from an exact time simulation of an 8-site system with Hamiltonian (5.9) ($\beta_0 = 1$). Shown are results for different velocities $|\Delta\delta/\Delta t|$ with $\Delta t = 0.1\ \beta_0^{-1}$. Initially, the system is in the ground state with $\delta = 0.5$. Even at slow δ variations, the fidelity dramatically decreases at the point where δ becomes negative.

For a first overview, we are going to observe an exactly solvable system of 8 sites with the Hamiltonian (5.9) in which we normalise the interactions strength to $\beta_0 \equiv 1$. Initially we start in the state $|0\rangle$, which is the exact

ground state of the system in the limit $\delta \to \infty$, i.e. for an infinite negative chemical potential.

As a first try, we start by switching on the laser, resulting in a fixed small effective Rabi frequency of $\Omega = 0.01$ and an initial $\delta_i \gg 0$ detuning. We simulate the time evolution of the state, while slowly decreasing δ to a value of $\delta_f = -1.5$, which is a regime where we previously found a nice anti-ferromagnetic like ground state.

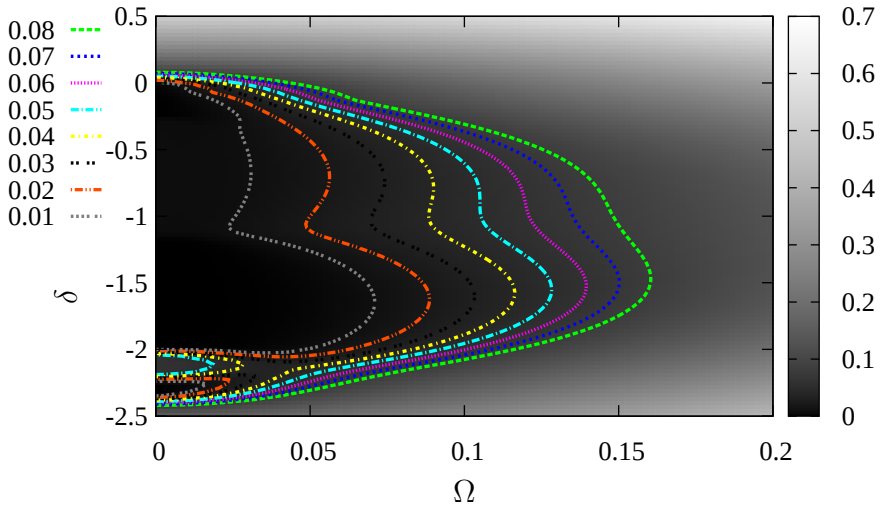

Figure 5.8: The energy gap ΔE between the ground and the first excited state of an 8-site system with Hamiltonian (5.9) ($\beta_0 = 1$) on a Ω-δ grid. ΔE vanishes rapidly when changing δ from 0.5 to 0 at a small Ω. The lines are indicating the contours of constant ΔE.

In figure 5.7 we find that this procedure fails. To not have to simulate the change in δ over a large range, in this figure we start at a ground state of the system with $\delta = 0.5$ and then decrease the detuning at different velocities $|\Delta\delta/\Delta t| = 10^{-2}, 10^{-3}, 10^{-4}$, where for all our calculations we are using a time-step of $\Delta t = 0.1\ \beta_0^{-1}$. After each time step we calculate the inner product of the actual state with the ground state of this point, that is

$$F \equiv |\langle\Psi|\Psi_G\rangle|, \tag{5.14}$$

with $|\Psi\rangle$ being the actual system state and $|\Psi_G\rangle$ being the actual ground state. We find that this fidelity dramatically decreases when reaching a regime of small negative δ.

The reason why the fidelity drops down to very small values even in case of very slow variation velocities can be understood by looking at the energy gaps of the system. In figure 5.8 we plot ΔE, i.e. the energy difference between the ground and first excited state on a Ω-δ grid. We use a grid spacing of $\Delta\delta = 0.03$ and $\Delta\Omega = 0.002$.

In regions of detuning $\delta \gg \Omega$ we find that $\Delta E \approx \delta$, which can be understood by the fact that in this case $|0\rangle$ is the ground state of the system and the first excited state consists of one Rydberg excitation costing an energy of approximately δ.

In figure 5.8, we observe that when changing δ from 0.5 to 0 at a small constant Ω, $\Delta E \to 0$ rapidly, which is the reason why the adiabatic procedure from figure 5.7 does not work. However, figure 5.8 suggests a different way

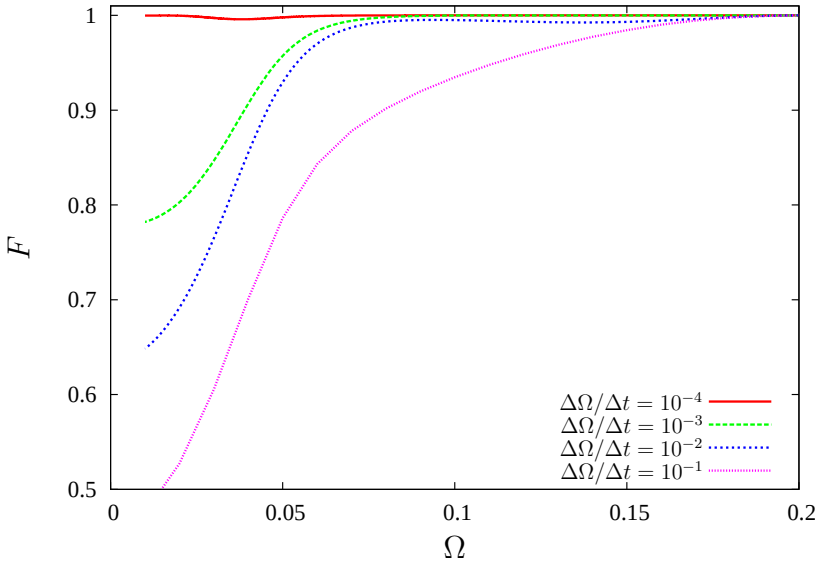

Figure 5.9: The overlap (fidelity) of the system state with the ground state, when driving Ω from 0.20 to 0.01 at constant $\delta = -1.5$. The results are from an exact time simulation of an 8-site system with Hamiltonian (5.9) ($\beta_0 = 1$). Shown are results for different values of $\Delta\Omega/\Delta t$ with $\Delta t = 0.1\ \beta_0^{-1}$. Initially, the system is in the ground state. We can reach a final ground state with over 99.9% fidelity.

to adiabatically drive to the ground state with $\delta = -1.5$ and $\Omega = 0.01$ at normalised $\beta_0 = 1$. To steer around the "obstacles", namely a vanishing energy gap, one can firstly increase Ω to a value of 0.2 at constant large detuning δ and secondly decrease δ to -1.5 at a constant $\Omega = 0.2$. Both of these to steps can be achieved by changing the parameters δ and Ω reasonably fast due to the large gap ΔE present at all times. Afterwards, Ω can be

decreased to a small value on a line of constant δ, where ΔE decreases much more slowly than in the previous example in figure 5.7.

For simplicity we again assume that the ground state with $\Omega = 0.2$, $\delta = -1.5$ at normalised $\beta_0 = 1$ can be reached up to a very high accuracy and concentrate on the critical region. Assuming that we can start in the ground state, in figure 5.9 we plot the fidelity in the case that Ω is decreased from 0.2 to 0.01 at constant $\delta = -1.5$ and for different velocities $\Delta\Omega/\Delta t = 10^{-1}, 10^{-2}, 10^{-3}, 10^{-4}$. We find that even in the very fast varying case of $\Delta\Omega/\Delta t = 10^{-1}$ we can reach a ground state with higher fidelity than in the $|\Delta\delta/\Delta t| = 10^{-4}$ example in figure (5.7). In the case of $\Delta\Omega/\Delta t = 10^{-4}$ we can reach a final ground state with a fidelity of over 99.9%!

lTEBD Simulations for a 30-Site System

Analogous to the 8-site calculations, we are now going to find a way to reach a high-fidelity anti-ferromagnetic like ground state for a system of 30 sites by utilising the lTEBD algorithm.

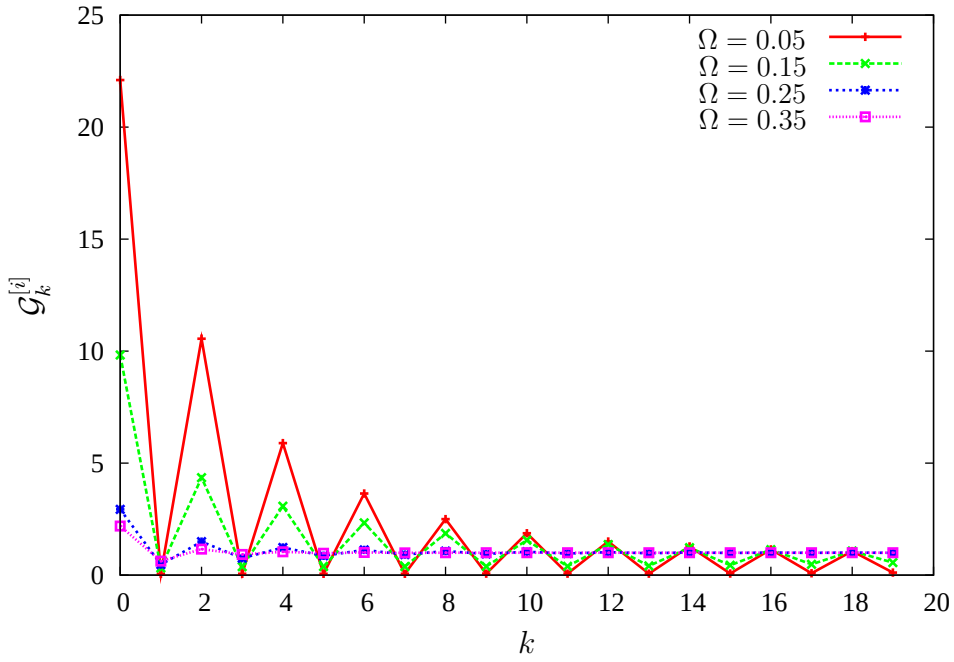

Figure 5.10: Density-density correlations for ground states of a 30-site system. The system Hamiltonian is (5.9) ($\beta_0 = 1$) with $\delta = -1.1$. The DDCs are evaluated between sites 6 and 25 ($i = 6$) for several values of Ω. The ground states are obtained by imaginary time evolution within the lTEBD algorithm. $\chi = 50$.

We again normalise the Hamiltonian (5.9) by $\beta_0 \equiv 1$. We then find a nice anti-ferromagnetic like ground state for small values of $0 \lesssim \Omega \lesssim 0.15$ at a detuning of $\delta = -1.1$. This can be seen in figure 5.10, where the DDC for ground states with $\delta = -1.1$ is plotted for several values of Ω. The results are obtained by imaginary time evolution within our lTEBD algorithm.

We are going to proceed like for the 8-site system but will now perform the time evolution for a full path, starting in the vacuum state and resulting in a state close to the ground state with $\Omega = 0.05$ and $\delta = -1.1$. Therefore, we perform real time simulations for 3 paths. For each path we are using a time step of $\Delta t = 0.1$. Initially we start in the vacuum state $|0\rangle$ with values $\Omega = 0.05$ and $\delta = 3$, for which the fidelity to the calculated ground state is approximately 99.99%.

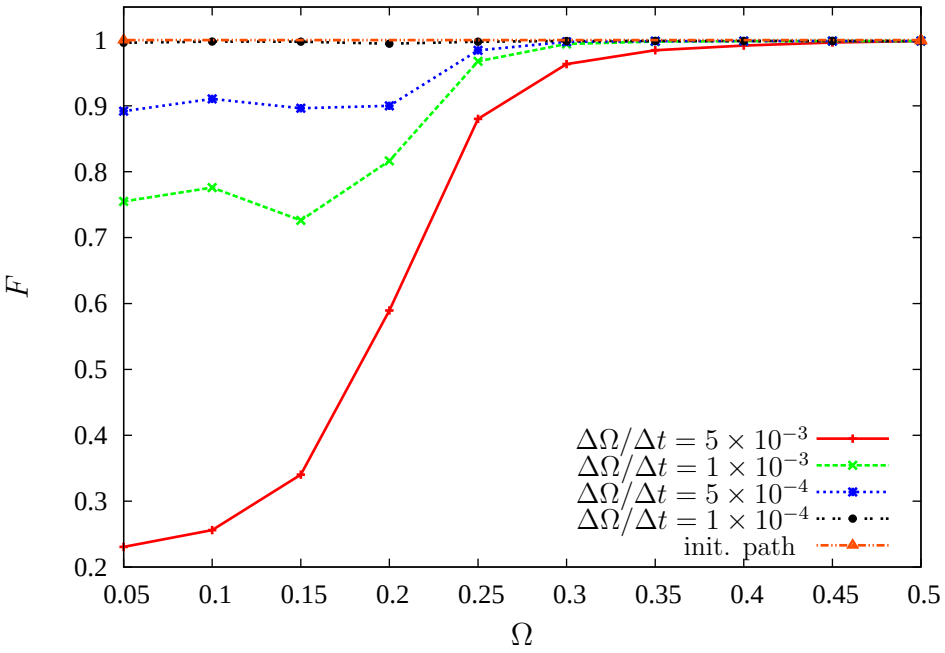

Figure 5.11: The overlap (fidelity) with the ground state, when driving Ω from 0.50 to 0.05 at constant $\delta = -1.1$ for different values of $\Delta\Omega/\Delta t$ with $\Delta t = 0.1\ \beta_0^{-1}$. Initially paths 1. and 2. (see text) are simulated. The results are from a 30-site system utilising the TEBD algorithm with the Hamiltonian (5.9) ($\beta_0 = 1$). $\chi = 50$.

1. We increase Ω from 0.05 to 0.5 at $\delta = 3$ with $\Delta\Omega/\Delta t = 0.05$. The final fidelity is over 99.9%.

2. We decrease δ from 3 to -1.1 at $\Omega = 0.5$ with $\Delta\delta/\Delta t = 0.05$. The final fidelity is approximately 99.8%.

3. We decrease Ω from 0.5 to 0.05 with several values of $\Delta\Omega/\Delta$. Results for the fidelity are shown in figure 5.11.

We observe that we can reach the ground state at $\Omega = 0.05$ with an overlap of about 99.6% when changing Ω with a rate of $\Delta\Omega/\Delta t = 1 \times 10^{-4}$.

In figure 5.12, we show to what extent the final state represents the DDC of the ground state with $\Omega = 0.05$ depending on the value of $\Delta\Omega/\Delta t$. In

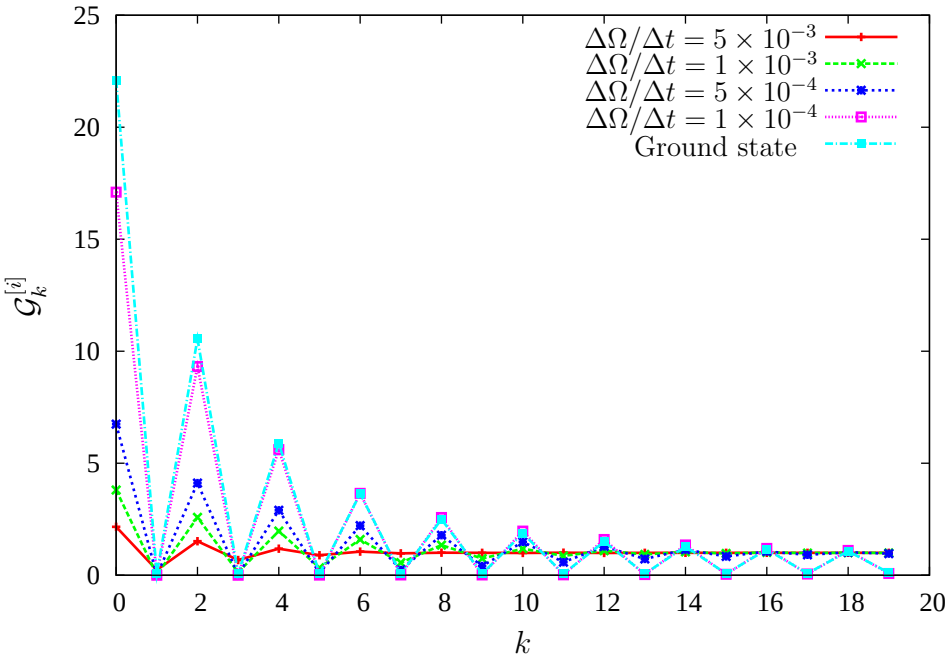

Figure 5.12: The Density-density correlation evaluated between sites 6 and 25 ($i = 6$), after driving Ω from 0.50 to 0.05 at constant $\delta = -1.1$, for different values of $\Delta\Omega/\Delta t$ with $\Delta t = 0.1\ \beta_0^{-1}$. The results are from a 30-site system utilising the TEBD algorithm with Hamiltonian (5.9) ($\beta_0 = 1$). $\chi = 50$.

this figure, we find marked differences in the shape of the correlations of the final state, obtained for the three "fast" driving velocities of $\Delta\Omega/\Delta t = 5 \times 10^{-3}, 1 \times 10^{-3}$ and 5×10^{-4} with a final overlap of less than 90%. In contrast to the DDC resulting from the ground state, in these cases we do not find a DDC, which is vanishing completely on every second site over a long range. However, we find that the correlation is converging to the one of the ground state with decreasing $\Delta\Omega/\Delta t$. In the case of the slowest driving velocity $\Delta\Omega/\Delta t = 1 \times 10^{-4}$ considered in our calculations, we obtain an excellent significant anti-ferromagnetic like correlation over all 19 sites. This correlation is very close to the one of the original ground state and small differences are only visible in the heights of the first three peaks.

We finally want to compare the time required for reaching this final ground state with experimentally accessible timescales. In the scheme presented above, at the slowest final changing rate of $\Delta\Omega/\Delta t = 1 \times 10^{-4}$ a total time of 4591 in units of $1/\beta_0$ is required. Note that this time could be further dramatically decreased by looking for shorter paths or by not using a constant driving velocity, but rather reducing it with time while approaching the final state. In reality the next-neighbour dipole-dipole interaction energy β_0 can be calculated from equations (5.10) and (5.5). For example, with $n = 20$ we find a value of approximately 16 GHz. Therefore, our total simulation time corresponds to approximately 0.26 μs in a realistic experiment. This value for example is well below the typical lifetime of $n = 20$ Rydberg levels for Rubidium, which can be found to be approximately 5 μs [11]. In general, this timescale limits experiments with Rydberg atoms and thus we conclude that the presented procedure above can in principle be implemented in realistic experimental setups.

Bibliography

[1] T. F. Gallagher. *Rydberg Atoms*. Cambridge University Press, (1994).

[2] D. Jaksch, J. I. Cirac, P. Zoller, S. L. Rolston, R. Côté, and M. D. Lukin. *Phys. Rev. Lett.* **85**, 2208 (2000).

[3] M. D. Lukin, M. Fleischhauer, R. Cote, L. M. Duan, D. Jaksch, J. I. Cirac, and P. Zoller. *Phys. Rev. Lett.* **87**, 037901 (2001).

[4] D. Tong, S. M. Farooqi, J. Stanojevic, S. Krishnan, Y. P. Zhang, R. Côté, E. E. Eyler, and P. L. Gould. *Phys. Rev. Lett.* **93**, 063001 (2004).

[5] K. Singer, M. Reetz-Lamour, T. Amthor, L. G. Marcassa, and M. Weidemüller. *Phys. Rev. Lett.* **93**, 163001 (2004).

[6] A. Gaëtan, Y. Miroshnychenko, T. Wilk, A. Chotia, M. Viteau, D. Comparat, P. Pillet, A. Browaeys, and P. Grangier. *arXiv:0810.2960* (2008).

[7] F. Robicheaux and J. V. Hernandez. *Phys. Rev. A* **72**, 063403 (2005).

[8] B. Sun and F. Robicheaux. *New Journal of Physics* **10**, 045032 (2008).

[9] R. Heidemann, U. Raitzsch, V. Bendkowsky, B. Butscher, R. Löw, L. Santos, and T. Pfau. *Phys. Rev. Lett.* **99**, 163601 (2007).

[10] K. Singer, J. Stanojevic, M. Weidemuller, and R. Cote. *J. Phys. B: At., Mol. and Opt. Phys.* **38**, 295 (2005).

[11] C. E. Theodosiou. *Phys. Rev. A* **30**, 2881 (1984).

Chapter 6

Conclusion & Outlook

We studied two systems with atoms in optical lattices numerically: (i) The dynamics of a superfluid current in the 1D Bose-Hubbard model, and (ii) Ground state correlations and time evolutions in a 1D lattice system of Rydberg atoms, including the effects of long-range interactions. To numerically simulate (ii), we extended the existing TEBD simulation technique [1] to work with interactions over larger distances than neighbouring sites in a 1D lattice Hamiltonian.

1. **Superfluid Boson Currents in 1D Lattices**

   In chapter 3 we investigated the crossover diagram for 1D superfluid currents within the Bose-Hubbard model. We found regions in which currents remain constant over long timescales and regions where it decays to zero rapidly. The superfluid behaviour depends on the ratio of the on-site interaction U to the tunnelling parameter J in the Bose-Hubbard Hamiltonian and the magnitude of the initial current.

   In contrast to previous analytical work in [2, 3], we were able to analyse the current stability in 1D for arbitrary interaction strengths. We achieved our results by employing the numerical iTEBD technique [4], a near-exact simulation algorithm for infinite 1D lattice Hamiltonians in the low-energy regime. With this numerical work, we could interpolate between the analytical solvable limits of strong and weak interactions. Unlike previous numerical mean-field studies in [2, 3], we were able to fully take into account quantum fluctuations.

   The method we analysed the system is directly comparable to experimental implementations, for example in [5]. We accelerate the particles, initially located in a superfluid ground state, to a desired quasi momentum and observe the real time evolution of the condensate fraction within a finite region of our infinite system. Both steps can be

performed in an optical lattice experiment by firstly accelerating the whole lattice potential (detuning the lattice laser beams) and afterwards observing interference patterns in a time-of-flight measurement.

This experiment has already been performed for 1D systems in the weakly-interacting Gross-Pitaevskii regime in [5]. In the future, it should also be possible for a regime in which the Bose-Hubbard model is valid. Data from such experiments could be directly compared to our quantitative numerical results.

2. **Rydberg Excitations in 1D Lattices**

We analysed a system of Rydberg atom excitations in an optical lattice potential (Chapter 5) and thereby gave an example of how a spin-1/2 model Hamiltonian can be engineered in an optical lattice. In this model, atoms are loaded into the lattice and an excitation laser is tuned to a Rydberg transition. Excited atoms give rise to strong interactions over long-ranges due to their large dipole-moment, which for example leads to excitation blockade effects in their vicinity. This model could be useful for implementations of quantum gates [6, 7] or the realisation of a quantum simulator.

We studied the dynamics of this system in real time simulations and calculated ground-states by utilising a variation of the TEBD simulation technique [1]. We extended this algorithm, which is capable of exactly simulating 1D slightly entangled lattice systems with nearest-neighbour interactions, to work with longer-range interactions in chapter 4 (lTEBD). We analysed the emergence of density-density correlations and entanglement as a function of time. We start from an initial state with no Rydberg excitation present, i.e. all spins are in the $|\downarrow\rangle$ state, which is exactly tailored to an experimental situation. We presented a method to dynamically prepare an anti-ferromagnetic phase of the system on experimentally realisable timescales.

Rydberg excitation suppression effects have been already observed experimentally and first quantum gate realisation experiments are very promising. The system that we simulated in chapter 5 could be also implemented in the future. Our lTEBD algorithm can guide such experiments in the sense that it can directly propose schemes to prepare interesting quantum states.

However, 1. and 2. are just two examples of what can be achieved with current time-dependent DMRG/TEBD algorithms. With these techniques, one is not limited to extract certain ground state properties, but can also

simulate real time-evolutions. This makes it possible to directly propose and test possible experiments in optical lattices. As outlined in chapter 2, by employing next-neighbour TEBD calculations already many dynamical effects in 1D lattice systems have been successfully studied. With the implementation of long-range interactions, even more than the already vast amount of 1D next-neighbour lattice models are accessible by this way. With the development of new algorithms, which are using matrix product operators, these systems could be also simulated very efficiently in infinite systems in which no boundary effects are present.

For future implementations of quantum information processing schemes or quantum simulator realisations, interactions over long ranges can be very important, like in a system of Rydberg atoms [6, 7]. Similar interesting systems, which also give rise to lattice Hamiltonians with dipolar interactions, consist of polar molecules in free space [8] or in an optical lattice potential [9].

Bibliography

[1] Guifré Vidal. *Phys. Rev. Lett.* **91**, 147902 (2003).

[2] E. Altman, A. Polkovnikov, E. Demler, B. I. Halperin, and M. D. Lukin. *Phys. Rev. Lett.* **95**, 020402 (2005).

[3] A. Polkovnikov, E. Altman, E. Demler, B. Halperin, and M. D. Lukin. *Phys. Rev. A* **71**, 063613 (2005).

[4] G. Vidal. *Phys. Rev. Lett.* **98**, 070201 (2007).

[5] J. Mun, P. Medley, G. K. Campbell, L. G. Marcassa, D. E. Pritchard, and W. Ketterle. *Phys. Rev. Lett.* **99**, 150604 (2007).

[6] D. Jaksch, J. I. Cirac, P. Zoller, S. L. Rolston, R. Côté, and M. D. Lukin. *Phys. Rev. Lett.* **85**, 2208 (2000).

[7] M. D. Lukin, M. Fleischhauer, R. Cote, L. M. Duan, D. Jaksch, J. I. Cirac, and P. Zoller. *Phys. Rev. Lett.* **87**, 037901 (2001).

[8] G. Pupillo, A. Griessner, A. Micheli, M. Ortner, D.-W. Wang, and P. Zoller. *Phys. Rev. Lett.* **100**, 050402 (2008).

[9] A. Micheli, G. K. Brennen, and P. Zoller. *Nature* **2**, 341 (2006).